

Spin Dynamics of Equilibrium Electrons in Gallium Arsenide

Von der Fakultät für Mathematik und Physik der
Gottfried Wilhelm Leibniz Universität Hannover

zur Erlangung des Grades

Doktor der Naturwissenschaften

Dr. rer. nat.

genehmigte Dissertation

von

Dipl.-Phys. Georg Martin Müller

geboren am 24. Mai 1982 in Emden

2010

Referent: Prof. Dr. Michael Oestreich
Korreferent: Prof. Dr. Rolf J. Haug
Tag der Promotion: 8. Dezember 2010

Kurzzusammenfassung

In der vorliegenden Dissertation wird die Spinrauschspektroskopie zur Untersuchung der Spindynamik in GaAs-basierten Halbleiterstrukturen nahe des thermischen Gleichgewichtes angewendet. Die Halbleiterspinrauschspektroskopie misst die stochastische Spinpolarisation eines Elektronenensembles mit Hilfe von nicht-resonanter Faradayrotation. Dementsprechend muss dem Probensystem im Gegensatz zu anderen experimentellen Techniken, in denen die Dephasierung oder Depolarisation einer künstlich erzeugten Spinpolarisation gemessen wird, keine Energie zugeführt werden.

Da die Spinfluktuationen in Echtzeit gemessen werden, war die Spinrauschspektroskopie bisher auf Frequenzen unterhalb von 1 GHz begrenzt. Die experimentelle Weiterentwicklung zur ultraschnellen Spinrauschspektroskopie, in der die Fluktuationen mit gepulstem Licht abgefragt werden, ermöglicht die Detektion von Spinrauschen bei Frequenzen von bis zu 16 GHz. Diese Frequenzen überschreiten die Bandbreite des verwendeten Photodetektors um einen Faktor von ungefähr 200. Um die Einschränkung der Spinrauschspektroskopie durch die endliche Bandbreite weitergehend zu untersuchen, wird elektrische Frequenzmischung zur Frequenzherabsetzung des elektrischen Spinrauschsignals angewendet. Ferner werden Spinrauschmessungen simuliert. Diese Simulationen belegen, dass auch ultraschnelle Digitalisierer mit niedriger Auflösung für die Spektralanalyse in der Spinrauschspektroskopie ohne einen deutlichen Verlust an Sensitivität verwendet werden können.

Zu den untersuchten Probensystemen gehören symmetrisch gewachsene, modulationsdotierte (110) GaAs/AlGaAs-Mehrfachquantenfilme. Dieses Experiment stellt die erste Spinrauschmessung an einem Halbleitersystem reduzierter Dimensionalität dar. Der Dyakonov-Perel-Mechanismus, der üblicherweise die Spindephasierung delokalisierte Elektronen in GaAs dominiert, ist für Spins entlang der Wachstumsrichtung in (110)-ausgerichteten Strukturen ineffektiv. Allerdings sind die dementsprechend erwarteten langen Spindephasierungszeiten in (110)-ausgerichteten GaAs/AlGaAs-Quantenfilmen bei niedrigeren Temperaturen herkömmlichen experimentellen Methoden, die auf optischer Spin-

orientierung beruhen, nicht zugänglich, da die optische Erzeugung von Löchern die beobachteten Spindephasierungszeiten aufgrund des Bir-Aronov-Pikus-Mechanismus verfälscht. Im Gegensatz dazu ermöglicht die Spinrauschspektroskopie Messungen in Abwesenheit von optisch erzeugten Löchern; die in dieser Arbeit gemessenen Dephasierungszeiten stellen die längsten veröffentlichten Spinlebenszeiten delokalasierter Elektronen in einem GaAs-Quantenfilm dar. Darüberhinaus werden die anisotrope Spindynamik, die auf der Tatsache beruht, dass der Dyakonov-Perel-Mechanismus für Spins in der Quantenfilmebene noch effektiv ist, sowie die Flugzeitverbreiterung der Spinrauschspektren, die aus der endlichen Aufenthaltszeit der Elektronen im Abfragevolumen resultiert, untersucht.

Die ultraschnelle Spinrauschspektroskopie ermöglicht es, die Spindynamik in n -dotiertem Volumen-GaAs in hohen Magnetfeldern zu untersuchen. Die untersuchten Proben weisen eine Donatorkonzentration etwas unterhalb und oberhalb des Metall-Isolator-Überganges auf. Die Abhängigkeit des effektiven Elektron-Landé-Faktors von Temperatur, Dotierung und Magnetfeld wird ebenso untersucht wie die Spindephasierung im transversalen Magnetfeld.

Zuletzt wird die Halbleiterspinrauschspektroskopie mit einem externen Magnetfeld durchgeführt, das in einem willkürlichen Winkel zu der Ausbreitungsrichtung des Lichtes steht, während üblicherweise ein Magnetfeld transversal zum Wellenvektor des Lichtes angelegt wird. Diese neuartige Geometrie der Spinrauschspektroskopie ermöglicht es, in einer einzelnen Messung sowohl die Spindephasierung als auch die Spinrelaxation zu untersuchen.

Schlagwörter: GaAs, Spindynamik, Spinrauschen.

Abstract

In this dissertation, spin noise spectroscopy is applied to study spin dynamics in GaAs based semiconductor structures close to thermal equilibrium. Semiconductor spin noise spectroscopy measures the stochastic spin polarization of the electron ensemble via off-resonant Faraday rotation. Correspondingly, no energy has to be deposited in the sample system contrary to other experimental techniques, in which the dephasing or the depolarization of an artificially injected spin polarization is measured.

Since the spin fluctuations are measured in real-time, spin noise spectroscopy had been hitherto limited to frequencies below 1 GHz. This thesis introduces the experimental advancement of ultrafast spin noise spectroscopy, in which the fluctuations are probed by pulsed light, and detection of spin noise at frequencies up to 16 GHz is demonstrated. These frequencies exceed the bandwidth of the photoreceiver by a factor of around 200. To further explore the limitations of the finite bandwidth of the detection system, electrical frequency mixing is applied for down-conversion of the electrical spin noise signal. Furthermore, spin noise measurements are simulated revealing that also ultrafast digitizers with low resolution can be utilized for spectral analysis in spin noise spectroscopy without any significant loss of sensitivity.

The spin dynamics in a symmetrically grown, modulation-doped, (110)-oriented GaAs/AlGaAs multiple quantum well structure are investigated in this work. This experiment represents the first spin noise measurements on a semiconductor system of reduced effective dimensionality. The Dyakonov-Perel mechanism that usually dominates spin dephasing of free electrons in GaAs is ineffective in (110)-oriented structures for spins along the growth direction. Nevertheless, the correspondingly anticipated long spin dephasing times in (110) GaAs/AlGaAs quantum wells at low temperatures are not accessible with conventional experiments that rely on optical spin orientation since the photocreation of holes obviates the observed spin dephasing times due to the Bir-Aronov-Pikus mechanism. Spin noise spectroscopy however enables measurements in the absence of optically created holes and the measured spin dephasing times in this work represent the longest re-

ported spin dephasing times for delocalized electrons in GaAs quantum wells. Additionally, the anisotropic spin dynamics, which result from the Dyakonov-Perel mechanism that is still effective for the spins in the quantum well plane, as well as the time-of-flight broadening of the spin noise spectra, which originates from the finite transit time of the electrons through the probe volume, are experimentally investigated.

The experimental technique of ultrafast spin noise spectroscopy enables investigation of spin dynamics in *n*-type bulk GaAs at high magnetic fields. The examined samples have a doping concentration slightly below and above the metal-to-insulator transition. The temperature, doping and magnetic field dependence of the effective electron Landé factor is studied as well as the spin dephasing in a transverse magnetic field.

Finally, semiconductor spin noise spectroscopy is carried out with a magnetic field oriented with an arbitrary angle to the direction of light propagation while usually the magnetic field is applied transverse to the light wavevector. This novel geometry for spin noise spectroscopy allows the investigation of spin dephasing and spin relaxation in a single measurement.

Keywords: GaAs, spin dynamics, spin noise.

Contents

1. Introduction	15
2. Equilibrium Spin Fluctuations in GaAs	21
2.1. Principles of spin noise spectroscopy	21
2.2. Spin dynamics of equilibrium electrons in GaAs	22
2.2.1. Band structure and dipole selection rules	23
2.2.2. From hydrogenic impurities to the metallic phase: Shallow donors in GaAs	26
2.2.3. Electrons in a magnetic field	28
2.2.4. Mechanisms of spin dephasing	31
2.3. Spin noise of donor-bound electrons	42
2.4. Spin noise of conduction band electrons	45
2.5. Spectral shape of spin noise	46
3. Experimental Methods	49
3.1. Fundamental setup	50
3.2. Background noise and experimental implications	55
3.2.1. Background noise and relative signal strength	55
3.2.2. Subtraction of background noise	58

3.3.	Extension of the experimental bandwidth	61
3.3.1.	Electrical down-conversion of the noise signal	62
3.3.2.	Limitations of FFT spectrum analysis	64
3.3.3.	Ultrafast spin noise spectroscopy	70
3.4.	Investigated samples	73
3.4.1.	Bulk samples	73
3.4.2.	(110)-oriented GaAs/AlGaAs multiple quantum well	74
4.	Experimental Results	77
4.1.	Spin noise spectroscopy in (110)-oriented quantum wells	77
4.1.1.	Probe wavelength dependence	79
4.1.2.	Anisotropic spin dynamics	81
4.1.3.	Time-of-flight broadening	84
4.1.4.	Intrinsic spin dephasing	87
4.2.	Spin noise spectroscopy in <i>n</i> -type bulk GaAs in transverse magnetic fields	90
4.2.1.	Spin dephasing in transverse magnetic fields	91
4.2.2.	Field, doping and temperature dependence of the effective Landé factor	96
4.3.	Spin noise spectroscopy in oblique magnetic fields	101
5.	Summary and Outlook	105
A.	Spin Noise Spectroscopy in Materials with Magnetic Order	111
A.1.	Model	112
A.2.	Experiment	114
	Bibliography	118
	List of Publications	137

List of symbols

In the following, a list of physical symbols that are used in this work is given. A few symbols are not unambiguously defined; their particular meaning becomes evident in the context. Symbols that are only used once are not included in this list.

Symbol		Section
\mathbf{m}	Spin polarization	2.1
$N^{\uparrow(\downarrow)}$	Number of [spin-up(down)] electrons in probe volume	2.1
σ^{\mp}	Right (left) circularly polarized probe light	2.1
$\alpha^{(\mp)}$	Optical absorption constant (for right and left circularly polarized light)	2.1
E	Electronic energy	2.2.1
\mathbf{k}, k	Electronic quasi wavevector	2.2.1
Γ	Origin of 1st Brillouin zone in GaAs	2.2.1
$m_e^{(*)}$	(Effective) electron mass	2.2.1
\hbar, h	(Reduced) Planck constant	2.2.1
\mathbf{s}	Spin operator	2.2.1
H	Hamilton operator	2.2.1

$\boldsymbol{\Omega}_D(\mathbf{k})$	Dresselhaus spin-orbit field	2.2.1
γ_D	Dresselhaus coefficient	2.2.1
E_G	Band gap	2.2.1
j	Angular momentum quantum number	2.2.1
Δ_{SO}	Spin-orbit splitting	2.2.1
e	Elementary charge	2.2.2
ϵ_r	Dielectric constant of GaAs	2.2.2
\mathbf{r}, r	Spatial coordinate	2.2.2
$\Psi_D(\mathbf{r})$	Electron donor wavefunction	2.2.2
$\Psi_{1,s}^*(\mathbf{r})$	Effective hydrogen atom groundstate wavefunction	2.2.2
$u_{CB,\mathbf{k}}(\mathbf{r})$	Periodic Bloch wavefunction for the conduction band	2.2.2
$E_{Ry}^{(*)}$	(Effective) Rydberg energy	2.2.2
$a_B^{(*)}$	(Effective) Bohr radius	2.2.2
r_D	Average donor distance	2.2.2
n_D	Doping concentration	2.2.2
E_F	Fermi energy	2.2.2
T	Temperature	2.2.2
k_B	Boltzmann constant	2.2.2
$f(E)$	Fermi-Dirac distribution	2.2.2
$D(E)$	Density of states	2.2.2
$g^{(*)}$	(Effective) electron Landé factor	2.2.3
μ_B	Bohr magneton	2.2.3
\mathbf{B}, B	Magnetic field	2.2.3
t	Time	2.2.3
$f_L = \omega_L/2\pi$	Larmor frequency	2.2.3
ω_C	Cyclotron frequency	2.2.3
k_F	Fermi wavevector	2.2.3
ν	Ratio of cyclotron energy to localization energy	2.2.3
\mathbf{m}_0	Equilibrium spin polarization	2.2.4
T_1	Spin relaxation time	2.2.4
$T_2^{(*)}$	(In)homogeneous spin dephasing time	2.2.4
$\Delta\Phi, \Delta\phi$	Dephasing angle	2.2.4
τ_c	Correlation time	2.2.4

$\delta\omega, \Omega$	Change of precessional frequency	2.2.4
τ_{P}^*	Momentum scattering time (including electron-electron scattering)	2.2.4
$\Omega_{\text{D}}(\mathbf{k})$	Dresselhaus spin-orbit field	2.2.4
$\Omega_{\text{R}}(\mathbf{k})$	Rashba spin-orbit field	2.2.4
α_{R}, ξ	Rashba coefficient	2.2.4
\mathcal{E}	Electrical field	2.2.4
ϵ_0	Vacuum permittivity	2.2.4
R_{d}	Distance from center of quantum well to doping sheet	2.2.4
τ_{d}	Transit time of an electron through a disorder domain	2.2.4
v_{F}	Fermi velocity	2.2.4
Ω_{HF}	Hyperfine field	2.2.4
N_{L}	Number of lattice nuclei overlapping with donor wavefunction	2.2.4
J	Exchange integral	2.2.4
γ	Spin rotation by anisotropic exchange interaction	2.2.4
$E_{\text{D}^0\text{X}}$	Binding energy of exciton-neutral donor complex	2.3
$\omega_{\text{D}^0\text{X}}$	Frequency of exciton-neutral donor transition	2.3
V	Probe volume	2.3
σ_{m_z}	Mean deviation of spin polarization	2.3
ω_{laser}	Laser frequency	2.3
f	Oscillator strength	2.3
$n^{(\mp)}$	Real part of refractive index (for right and left circularly polarized light)	2.3
n'	Imaginary part of refractive index	2.3
c_0	Velocity of light in vacuum	2.3
λ	Probe light wavelength in vacuum	2.3
Γ	Width of optical transition	2.3
\tilde{n}	Change of refractive index close to optical transition	2.3
θ_{F}	Faraday rotation angle	2.3

σ_{θ_F}	Mean deviation of faraday rotation	2.3
l	Sample thickness	2.3
$A = \pi w_0^2$	Laser probe area	2.3
w_0	Laser beamwaist at focus	2.3
ζ	Maximum degree of optical spin orientation in the conduction band	2.3
F	Spin noise suppression by Pauli blockade	2.4
$f = \omega/2\pi$	frequency	2.5
$S(f)$	Spin noise spectrum	2.5
w_{FWHM}	Full width at half maximum of spin noise curve	2.5
z_R	Rayleigh range	3.1
ρ	Detector responsivity	3.1
z_R	Rayleigh range	3.1
I	Data transmission	3.1
f_S	Sample rate	3.1
B	Detection bandwidth	3.1
P_{laser}	Probe laser power	3.2.1
S_{SN}	Shot noise power level	3.2.1
η	Relative signal strength	3.2.1
ω_{LO}	Local oscillator frequency	3.3.1
q	Quantization error	3.3.2
x	Analog input	3.3.2
y	Digital output	3.3.2
σ_{SN}^2	Integrated shot noise power	3.3.2
$\sigma_{q(\text{, gran/over})}$	Mean deviation of quantization error (due to granularity/overload of the digitizer)	3.3.2
α	Spin noise amplitude in simulations	3.3.2
SNR	Signa-to-noise ratio	3.3.2
N	Number of averages for spectrum analysis	3.3.2
f_{rep}	Pulsed laser repetition rate	3.3.3
μ	Electron mobility	3.3.3
$T_{2,z}$	Spin dephasing time along the growth direction of a (110) quantum well	4.1
$T_{2,\perp}$	Spin dephasing time perpendicular to the growth direction of a (110) quantum well	4.1

κ	Ratio of spin dephasing times along the growth direction and in the quantum well plane	4.1
τ_{ee}	Electron-electron scattering time	4.1.3
$w(z)$	Laser beamwaist	4.1.3
$P(\mathbf{r}, \mathbf{r}_0)$	Sojourn probability in the case of two-dimensional diffusion	4.1.3
D	Diffusion constant	4.1.3
$I(\mathbf{r})$	Laser beam intensity profile	4.1.3
Q	Spin quality factor (ratio of spin precessional frequency to dephasing rate)	4.2.1
$\mathbf{k}_{\text{laser}}$	Probe light wavevector	4.3
\mathbf{M}	Magnetization	A.1
M_S	Saturation magnetization	A.1
μ_0	Permeability constant	A.1
Ψ_F	Specific Faraday rotation angle	A.1

CHAPTER 1

Introduction

The physical properties of the electron spin in semiconductors have been an active field of research since the pioneering publications of Lampel [1] and Parsons [2] in the end of the 1960s. The theoretical proposal of the spin field effect transistor by Datta and Das in 1990 [3] has boosted the number of research papers in this field, giving rise to the notion of semiconductor spintronics [4, 5, 6, 7]. Some years later, localized electronic spins in semiconductors were suggested as possible qubits for quantum computation [8, 9, 10]. The research field of semiconductor spintronics aims at the design of electronic devices that can be operated at higher speed while showing less energy dissipation compared to today's silicon based CMOS technology which completely neglects the electronic spin degree of freedom. In contrast to such quantitative improvements, possible solid state spin-based quantum information devices target the physical implementation of qualitatively new types of algorithms and encryption protocols.

Both lines of research as well as pure scientific curiosity demand a detailed understanding of the dephasing of electron spins in semiconduc-

tors. As a matter of fact, investigations of the electron spin dephasing or relaxation times have been an integral part of semiconductor spintronics since the very beginning [1, 2, 11]. However, most experimental probes of semiconductor spin dynamics rely on generation of a non-equilibrium spin polarization [1, 2, 12, 13, 14, 15, 16]. This creation of a spin polarized electron ensemble away from thermal equilibrium is necessarily accompanied by energy transfer to the system which modifies the effectiveness of the different mechanisms of spin dephasing. Already everyday physical problems do in principle encounter such observer effects: For instance, a thermometer extracts thermal energy from the investigated system and alters the temperature of the sample. In this specific case, a thermometer with a significantly smaller heat capacity than the investigated system will deliver physical meaningful results. In an alternative approach, the experimenter repeats the measurement with identically prepared systems and thermometers of different heat capacity and extrapolates the experimental outcome to vanishing heat capacity. However, it turns out that the analogous approach for measuring dephasing times of semiconductor spin ensembles, though often carried out, happens to fail due to the intricate dependence of the various spin dephasing mechanisms on the excitation density [17]. Hence, for investigating semiconductor spin dynamics, a measurement technique corresponding to a thermometer with zero heat capacity is needed.

The fluctuation-dissipation theorem [18], which states that the response of a system to a perturbation is directly linked to its fluctuations at thermal equilibrium, discloses a way to solve this problem. In the case of the Brownian motion of a pollen particle in water, it was Einstein who realized that the random forces which make a particle jitter on a microscopic scale at thermal equilibrium cause the friction while dragging the particle through the liquid [19]. Analogously, the spin fluctuations of an electronic ensemble deliver information about the dynamics of the spin system under an infinitesimal external perturbation which is experimentally not realizable [20]. Such spin noise, i.e., a time-varying stochastic spin polarization, was first predicted by Bloch [21] for a nuclear spin system and first measured by Sleator *et al.* [22]. Later, other groups experimentally verified the fluctuation-dissipation theorem via magnetometric [23, 24, 25] and electrical [26]

measurements of the magnetic noise of spin glasses. More recently, Rugar and co-workers extended the use of spin fluctuations to very small nuclear and electronic spin ensembles by means of magnetic force microscopy [27, 28, 29, 30, 31]. In 2006, Müller and Jerschow utilized nuclear spin noise for magnetic resonance imaging [32].

Measurement of spin noise by optical means, i.e., spin noise spectroscopy, was first carried out in atom optics by Aleksandrov and Zapskii [33] in 1981. Spin-orbit coupling gives rise to an interaction between the electron spin and the photon helicity via the dipole selection rules and thereby maps the spin noise onto the light polarization of an off-resonant probe laser via the Faraday effect [34]. Application of off-resonant probe light is an established concept in atom optics to avoid optical pumping and to study optically thick samples [35]. Several experiments in alkali metal vapors (see, e.g., References 36 and 37) clearly prove that for sufficient detuning from the resonance spin noise spectroscopy can be viewed as a quantum non-demolition measurement [38, 39, 40] of the atomic spin.

In 2005, spin noise spectroscopy was first demonstrated in a semiconductor system, introducing this sensitive and nearly perturbation-free technique to study semiconductor spin physics [41]. Spin noise spectroscopy has been transferred to semiconductor physics rather late since the faster spin relaxation times in semiconductors compared to atoms require much more sophisticated experimental means [42].

In this work, spin noise spectroscopy is used to investigate spin dynamics in bulk GaAs in a transverse magnetic field as well as in GaAs/AlGaAs based quantum wells. The relevant theoretical background is given in Chapter 2: After further elucidating the measurement principle of semiconductor spin noise spectroscopy (Section 2.1), Section 2.2 reviews the spin dynamics of donor electrons in GaAs. The discussion in this section especially shows that spin dephasing is delicately influenced by optical excitation. In the Sections 2.3 and 2.4, a model is presented to calculate the stochastic spin polarization and the resulting variance of the Faraday rotation, i.e., the spin noise power, for a semiconductor system with donor-bound, localized electrons and for a fully degenerate semiconductor system with electrons in the conduction band. The spectral shape of spin noise spectrum is calculated in Section 2.5.

After laying the theoretical groundwork, the experimental realization

of spin noise spectroscopy is discussed in detail (Chapter 3). First, the particular components of the setup are introduced (Section 3.1). Then the impact of spurious noise contributions to the detection sensitivity is reviewed (Section 3.2). Since spin noise spectroscopy records the spin fluctuations in real-time, a high-bandwidth detection system is required and experimental realizations of spin noise spectroscopy before this work have been limited to frequencies below 1 GHz. Section 3.3 presents three possible routes to increase the experimental bandwidth which is required to study spin dynamics in high transverse magnetic fields that yield a high-frequency modulation of the spin fluctuations. In Section 3.3.1, the application of electrical frequency mixing to down-convert the high-frequency spin noise signal for spectrum analysis is inspected. Subsequently, the influence of the resolution of the digital data acquisition on the detection sensitivity is studied by means of simulated measurements in order to prove that also ultrafast, low-resolution analog-to-digital converters can be used to increase the bandwidth of the spectrum analysis for spin noise spectroscopy (Section 3.3.2). Finally, an experimental advancement of semiconductor spin noise spectroscopy is presented where the spin dynamics are sampled by pulsed probe light allowing detection of spin noise at frequencies that are in principle only limited by the inverse pulse width (Section 3.3.3).

The investigated sample systems are chosen to highlight the benefits of the rather new technique of semiconductor spin noise spectroscopy and to deliver insight into the underlying spin dephasing mechanisms that can hardly be gathered by experiments that rely on optical spin orientation and exclude measurements at thermal equilibrium. First, symmetrically modulation-doped (110)-oriented GaAs/AlGaAs quantum wells are examined (Section 4.1). This experiment represents the first application of spin noise spectroscopy to a semiconductor system of reduced dimensionality. In these structures with a (110)-oriented growth axis, extremely long spin dephasing times are anticipated since the Dyakonov-Perel mechanism that usually dominates spin dephasing of free electrons in GaAs is ineffective for spins aligned along the growth direction. This behavior was experimentally demonstrated at relatively high temperatures [43, 44]. However, at low temperatures the optical electron-hole pair generation diminishes the observed spin dephasing times and the intrinsic dephasing times at low temperatures remained

unknown. In this work, spin noise spectroscopy, which largely avoids electron-hole pair generation by detuning of the probe laser from the optical resonance, is applied to study spin dynamics in a symmetrically modulation-doped (110)-oriented GaAs/AlGaAs multiple quantum well structure. Correspondingly, the probe wavelength dependence is studied first (Section 4.1.1). Then, an in-plane magnetic field is applied to demonstrate that spins perpendicular to the growth direction dephase significantly faster due to the anisotropy of the Dyakonov-Perel mechanism (Section 4.1.2). In Section 4.1.3, the size of the probe volume is systematically varied to study the influence of the finite transit time of an electron through the laser spot. Finally, the physical origin of the observed intrinsic spin dephasing times is discussed (Section 4.1.4).

Next, the new experimental technique of ultrafast spin noise spectroscopy is applied to study spin dynamics of n -type bulk GaAs in transverse magnetic fields. A similar investigation of the spin dephasing in transverse magnetic fields was carried out by means of resonant spin amplification [16]. The explanation of those experimental findings, however, seems in parts to be questionable and, in addition, the influence of optical pumping in those measurements has not been clarified. In this work, spin dephasing in transverse magnetic fields is investigated for one sample slightly below the metal-to-insulator transition and for another well above (Section 4.2.1). To this end, spin dephasing at high precessional frequencies is evaluated by spin quality factors that are defined as the ratio of the precession frequency and the dephasing rate. The technique of ultrafast spin noise spectroscopy also allows high-precision g -factor spectroscopy which is applied to investigate the doping, temperature, and magnetic field dependence of the effective Landé factor in n -type bulk GaAs (Section 4.2.2).

In spin noise spectroscopy, the magnetic field is most often applied transverse to the probe light wavevector to modulate the detected spin fluctuations with the Larmor frequency. In this work, also the influence of a magnetic field with an arbitrary angle to the direction of light propagation is investigated (Section 4.3).

CHAPTER 2

Equilibrium Spin Fluctuations in GaAs

The central experimental tool of this work is semiconductor spin noise spectroscopy which is applied to investigate spin dynamics of equilibrium carriers in GaAs. The underlying principles of this measurement technique are elucidated in Section 2.1. Section 2.2 elaborates the basic facts of spin dynamics of donor electrons in GaAs. With these fundamentals at hand, spin noise of donor electrons is considered in more detail for two complementary systems—a low doped semiconductor crystal with localized, non-interacting electron spins (Section 2.3) and a highly doped system with delocalized electrons in the conduction band (Section 2.4). It is shown in Section 2.5 that spectral analysis of the spin fluctuations allows investigation of the underlying spin dynamics.

2.1. Principles of spin noise spectroscopy

The basic principle of spin noise spectroscopy is to map spin fluctuations in the sample onto the polarization state of the probe light. Cor-

respondingly, spin noise spectroscopy does not rely on an artificially injected spin polarization as other experimental techniques but on a stochastic spin polarization at thermal equilibrium. This stochastic spin polarization of the equilibrium electron ensemble,¹

$$m_z = \frac{N^\uparrow - N^\downarrow}{N^\uparrow + N^\downarrow}, \quad (2.1)$$

has a zero mean, but a finite standard deviation that originates from the finite ensemble size $N = N^\uparrow + N^\downarrow$ and the resulting incomplete cancellation of up- (N^\uparrow) and down (N^\downarrow) spins as first predicted by Bloch for a nuclear spin ensemble [21]. Due to spin dependent bleaching of an optical transition, this fluctuating spin imbalance becomes manifest in a difference of the absorption coefficient α^\mp for right (σ^-) and left (σ^+) circularly polarized light. This dichroism translates via the Kramers-Kronig relations [45, 46] to a difference of the dispersive part of the refractive index for the two light components. Due to this circular birefringence, linearly polarized light, which is composed out of σ^- and σ^+ light, acquires a rotation of its polarization direction, known as Faraday effect [34]. Hence, the linear light polarization fluctuates. As shown in the following, these fluctuations contain valuable information about the unperturbed spin dynamics in the semiconductor sample at thermal equilibrium.

2.2. Spin dynamics of equilibrium electrons in GaAs

This work focuses on spin dynamics in GaAs which has evolved as the quintessential system for spinelectronic research. Nevertheless, spin noise spectroscopy works in a variety of different semiconductor systems: The only fundamental requirement is that the investigated system possesses an optical transition which connects the electron spin with the photon helicity. The bandstructure of GaAs and the corresponding optical selection rules are shortly discussed in Section 2.2.1

¹In the following, the axis of quantization for the electron spin is the z -axis if not stated otherwise.

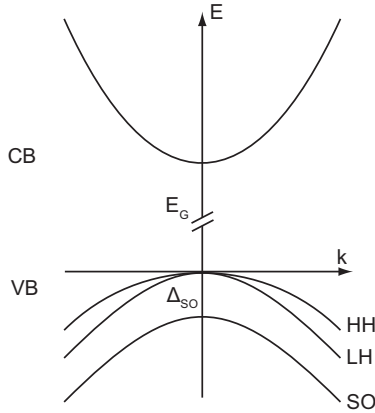


Figure 2.1.: Band structure of GaAs: The conduction band (CB) is separated from the valence bands by the energy gap of E_G from the conduction band; the heavy (HH) and the light hole (LH) valence band are degenerate at the Γ -point while the degeneracy with the split-off (SO) band is lifted by spin-orbit coupling.

to further elucidate this point. This chapter proceeds with presenting the basic physical properties of so-called shallow impurities which allow to insert additional electrons in the GaAs crystal (Section 2.2.2). Section 2.2.3 shortly reviews the interaction of an external magnetic field, which is applied in most of the experiments in this work, with the orbital and spin degrees of freedom of delocalized and localized electrons. The discussion of spin dynamics of equilibrium electrons in GaAs closes with describing the different mechanisms of spin dephasing (Section 2.2.4).

2.2.1. Band structure and dipole selection rules

GaAs is a III-V semiconductor with a direct bandgap. Figure 2.1 depicts the dispersion $E(k)$ of the conduction band and the three highest valence bands in the vicinity of the Γ -point, i.e., for small quasi-momentum k . The dispersion of the conduction band is parabolic close to

2. Equilibrium Spin Fluctuations in GaAs

the Γ -point and isotropic so that it can be written as $E(k) = \hbar^2 k^2 / 2m_e^*$ with m_e^* being the effective mass of the electron [11]. However, at higher momenta the conduction band dispersion in GaAs has also anharmonic contributions and, hence, the effective mass is generally a function of the electron energy. In this work, the effective mass at the conduction band edge of $m_e^*/m_e \approx 0.067$ is an accurate approximation in the tested temperature [47], doping [48], and magnetic field range [49]. The conduction band states have s -type character, i.e., the periodic part of the Bloch wave has a vanishing orbital angular momentum. Still, the spin degree of freedom of the conduction band electrons has to be considered. The conduction band states are twofold degenerate due to time-reversal symmetry [50], i.e.,

$$E_{\uparrow}(k) = E_{\downarrow}(-k). \quad (2.2)$$

However, since GaAs with its zinc blende structure lacks inversion symmetry, the conduction band is spin-split:²

$$E_{\uparrow}(k) = E_{\downarrow}(-k) \neq E_{\downarrow}(k). \quad (2.3)$$

The Hamilton operator for the conduction band electrons up to the third order in \mathbf{k} including spin-orbit coupling reads [51]

$$H = \frac{\hbar \mathbf{k}^2}{2m_e^*} + \mathbf{s} \times \boldsymbol{\Omega}_D(\mathbf{k}), \quad (2.4)$$

where \mathbf{s} is the spin operator and $\boldsymbol{\Omega}_D(\mathbf{k})$ is the so-called Dresselhaus field [52]

$$\boldsymbol{\Omega}_D(\mathbf{k}) = \frac{2\gamma_D}{\hbar} [k_x (k_y^2 - k_z^2), k_y (k_z^2 - k_x^2), k_z (k_x^2 - k_y^2)]. \quad (2.5)$$

Here, the coordinate system is chosen to coincide with the crystallographic axes of the cubic unit cell. In GaAs, spin-orbit coupling in the conduction band is so small ($\gamma_D \approx 27.5 \text{ eV}\text{\AA}^3$ [53]) that it is usually negligible for optical interband transitions close to the Γ -point. However, spin-orbit coupling plays an important role for the dephasing of a

²Lack of inversion symmetry is obviously a necessary, but not a sufficient criterion for spin-split bands.

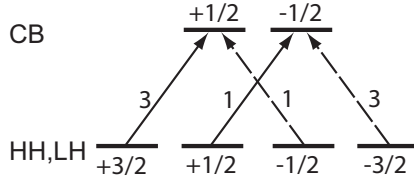


Figure 2.2.: Dipole selection rules for GaAs for right (solid arrow) and left (dashed arrow) circularly polarized light from the heavy (HH) and light hole (LH) band to the conduction band; the corresponding relative transition strength is given next to the arrows.

spin polarization in the conduction band (see Section 2.2.4).

The periodic Bloch functions of the three valence bands, which are separated by the energy gap of $E_G = 1.519$ eV at 0 K [54], have p -type character. Due to spin-orbit coupling, the total angular momentum of these wavefunctions has to be considered. The so-called heavy and light hole band have a total angular momentum of $j = 3/2$, while the third band has a total angular momentum of $j = 1/2$ and spin-orbit coupling lifts its degeneracy with the heavy and light hole band at the Γ -point. Therefore, this third valence band is called split-off band. This splitting amounts to $\Delta_{SO} = 0.341$ eV in GaAs [54] (see Figure 2.1). Accordingly, the split-off band can be neglected regarding optical transitions in a relatively wide spectral region around E_G .

Figure 2.2 shows the allowed optical transitions from the heavy and light hole band to the conduction band close to the Γ -point for circularly polarized light [11]. The relative strength of each transitions can be easily calculated via the Wigner-Eckart theorem (see, e.g., Reference 50) and is given in Figure 2.2. Correspondingly, circularly polarized light with an energy of E_G and a wavevector along the z -direction creates a spin polarization at the conduction band edge of³

$$m_z = \frac{3 - 1}{3 + 1} = 0.5. \quad (2.6)$$

³Under continuous light excitation, the observed degree of spin polarization is also determined by the ratio of recombination and spin dephasing time; the value of $m_z = 0.5$ gives the theoretical upper limit.

Spin noise spectroscopy can be applied to any system that has an optical transition which allows spin orientation in the conduction band by irradiation with circularly polarized probe light. In the absence of spin-orbit coupling, such an optical spin orientation is forbidden by the dipole selection rules. Note that momentum quantization due to the confinement in a GaAs/AlGaAs quantum well lifts the degeneracy between heavy and light hole band at the Γ -point and higher degrees of spin polarization than $m_z = 0.5$ can be achieved by optical orientation [55].

2.2.2. From hydrogenic impurities to the metallic phase: Shallow donors in GaAs

The concentration of intrinsic conduction band electrons in an ideal GaAs crystal with its large band gap is negligible even at room temperature. Certain impurities of the crystal however can easily donate an electron to the conduction band. The concentration of equilibrium electrons close to the conduction band edge can be adjusted by incorporating these shallow impurities (donors) into the crystal. Silicon on a gallium site in the GaAs crystal acts as a donor since the silicon atom has four valence electrons while a gallium atom has three. The coulomb interaction between the extra positive charge of the silicon nucleus and the fourth valence electron is screened by the core and valence electrons of the silicon atom as well as by the valence electrons at other lattice sites. Hence, this extra electron is not as tightly bound to the nucleus as in an isolated silicon atom and can be easily ionized. The corresponding ionization energy is calculated within the effective mass approximation, in which the nucleus of the impurity atom is treated as a hydrogenic potential attenuated by the dielectric constant of GaAs $\epsilon_r = 12.5$ [56]. The complete Hamilton operator is given by the single electron Hamiltonian of the ideal crystal plus this hydrogenic potential and the corresponding electron wavefunction $\Psi_D(\mathbf{r})$ is assumed to be a superposition of the Bloch waves that represent solutions for the ideal crystal. The groundstate wavefunction is in good approximation given by the product of the periodic Bloch function at the conduction band

edge and the 1s-hydrogen-like wavefunction:

$$\Psi_{\text{D}}(\mathbf{r}) \approx u_{\text{CB},0}(\mathbf{r})\psi_{1s}^*(\mathbf{r}). \quad (2.7)$$

Correspondingly, the ionization energy is given by an effective Rydberg energy of

$$E_{\text{Ry}}^* = \frac{m_e^*}{m_e \epsilon_{\text{r}}^2} E_{\text{Ry}}, \quad (2.8)$$

which amounts to about 6 meV in GaAs. The characteristic dimensions of the donor wavefunction are given by the effective Bohr radius

$$a_{\text{B}}^* = \frac{m_e \epsilon_{\text{r}}^2}{m_e^*} a_{\text{B}}, \quad (2.9)$$

which is around 10 nm in GaAs. Accordingly, the donor wavefunction ranges over a large number of lattice sites which justifies *a posteriori* the modeling of the screening by the macroscopic dielectric constant.

The average distance between adjacent donors amounts to $r_{\text{D}} = (4\pi n_{\text{D}}/3)^{-1/3}$ with n_{D} being the three dimensional density of donor atoms. As soon as electronic wavefunctions overlap, the above modeling does not hold anymore and the binding energy broadens, which results in the formation of an impurity band [56]. The degree of overlap is quantified by the dimensionless parameter $n_{\text{D}}^{1/3} a_{\text{B}}^*$ [57]: At $n_{\text{D}}^{1/3} a_{\text{B}}^* < 0.25$, the electronic states in the impurity band are completely localized and vanishing electrical conductivity is expected at zero temperature. In the range of $0.25 < n_{\text{D}}^{1/3} a_{\text{B}}^* < 0.33$, the metal-to-insulator transition [58] is reported to occur which means that a doped semiconductor above this impurity concentration shows metallic behavior with electrical conductivity at zero temperature. At $n_{\text{D}}^{1/3} a_{\text{B}}^* > 0.43$, the Fermi energy E_{F} enters the conduction band and can be calculated via the integral equation

$$n_{\text{D}} = \int_{E_{\text{G}}}^{\infty} f(E) D(E) dE, \quad (2.10)$$

where $D(E)$ is the density of states for the conduction band and $f(E)$

is the Fermi-Dirac distribution function

$$f(E) = 1 / \left(e^{[E-E_F]/k_B T} + 1 \right). \quad (2.11)$$

As discussed in the previous paragraphs, the presence of equilibrium electrons in or close to the conduction band in a three-dimensional GaAs crystal is inevitably connected to the existence of impurities. In two-dimensional structures, however, modulation-doping allows spatial separation of the ionized impurity atoms from the carriers [59]. To this end, the doping layers are incorporated in the barrier material, while the donor electrons are confined to the quantum well. The quantum well structure investigated in this work is modulation-doped.

2.2.3. Electrons in a magnetic field

An external magnetic can significantly influence the energy and the spin dynamics of an electron. In this section, the interaction of a magnetic field with the spin and orbital degrees of freedom is discussed.

Zeeman spin splitting and Larmor spin precession. In an external magnetic field, the degeneracy between spin-up and spin-down states at the conduction band edge is lifted, which is known as Zeeman splitting. The corresponding Hamilton operator reads

$$H_Z = -\frac{g^* \mu_B}{\hbar} \mathbf{B} \cdot \mathbf{s}, \quad (2.12)$$

where g^* denotes the effective Landé g -factor which strongly deviates due to spin-orbit coupling from the vacuum electron Landé factor of $g \approx 2$. This deviation can be illustrated by Roth's formula [60]:

$$\frac{g^*}{g} = 1 - \left(\frac{m_e}{m_e^*} - 1 \right) \frac{\Delta_{\text{SO}}}{3E_G + 2\Delta_{\text{SO}}}, \quad (2.13)$$

which can be derived via 3-level $\mathbf{k} \cdot \mathbf{p}$ perturbation theory in second order.⁴ The underlying 3-level GaAs model, in which the lowest con-

⁴The $\mathbf{k} \cdot \mathbf{p}$ method is, e.g., described in Reference 61.

duction band, the heavy- and the light-hole band, and the split-off band are taken into account, is already depicted in Figure 2.1. As mentioned above, the quantity Δ_{SO} is an immediate measure of the strength of the spin-orbit coupling. Equation (2.13) shows that for $\Delta_{\text{SO}} = 0$, i.e., no spin-orbit coupling, the effective Landé factor attains the value of the free electron g -factor. Roth's formula does only yield a qualitative understanding of the deviation of the effective Landé factor. The experimentally determined value of $g^* \approx -0.48$ at the conduction band edge is in good quantitative agreement with 5-level $\mathbf{k} \cdot \mathbf{p}$ theory [62, 63]. Away from the conduction band edge, at higher electron energies, the band non-parabolicity has to be considered as in the case of the effective mass [47, 48, 49]. This results in a theoretically and experimentally well established [47, 64] energy dependence of g^* :

$$g^*(E) = -0.48 + 6.3 \text{ eV}^{-1} \times E. \quad (2.14)$$

This energy dependence is—contrary to the energy dependence of the effective mass—relevant in the experimentally tested parameter range in this work. Note that the effective Landé factor approaches the free electron value of $g \approx 2$ with increasing electron energy.

The Zeeman energy amounts to $g^* \mu_{\text{B}} B \approx 30 \mu\text{eV}$ at a magnetic field of $B = 1 \text{ T}$. In view of the thermal energy $k_{\text{B}} T \approx 86 \mu\text{eV}$ for $T = 1 \text{ K}$, the Zeeman spin splitting is relatively small and a magnetic field induced electron spin polarization can be neglected in this work. Nevertheless, an electron spin perpendicular to the magnetic field is a superposition of the two spin states whose degeneracy is lifted by the magnetic field. Hence, the coherent time evolution of the spin shows a beating. The equation of motion for the expectation value of the spin reads in the Heisenberg picture

$$\begin{aligned} i\hbar \frac{d}{dt} \langle s_i \rangle &= \langle [s_i, H_Z] \rangle, \\ i\hbar \frac{d}{dt} \langle s_i \rangle &= -\frac{g^* \mu_{\text{B}}}{\hbar} \langle [s_i, s_j] \rangle B_j, \\ \frac{d}{dt} \langle s_i \rangle &= -\frac{g^* \mu_{\text{B}}}{\hbar} \epsilon_{ijk} \langle s_k \rangle B_j, \end{aligned} \quad (2.15)$$

2. Equilibrium Spin Fluctuations in GaAs

where the Einstein convention and the commutator relation $[s_i, s_j] = i\hbar\epsilon_{ijk}s_k$ are used. For $\mathbf{B} = [B, 0, 0]^5$, this differential equation for the y - and z -component is solved by

$$\begin{aligned}\langle s_y \rangle &\propto \sin \omega_L t, \\ \langle s_z \rangle &\propto \cos \omega_L t,\end{aligned}\tag{2.16}$$

where the $\omega_L/2\pi \equiv f_L = g^*\mu_B B/h$ is called Larmor frequency. Due to this precessional motion, the spin component perpendicular to a magnetic field is modulated with this frequency.

Landau quantization and donor-bound electrons in a magnetic field.

The so-called Landau quantization results from the quantization of the orbital motion of a free electron perpendicular to the external field. The electronic energy reads (neglecting the spin)

$$E_L = \frac{\hbar^2 k_x^2}{2m_e^*} + \hbar\omega_c \left(n + \frac{1}{2} \right), \quad n = 0, 1, 2, \dots,\tag{2.17}$$

where $\omega_c = \frac{eB}{m_e^*}$ is denoted as the cyclotron frequency. The orbital motion along the magnetic field direction still contributes to the kinetic energy. The low effective mass in GaAs yields significantly higher cyclotron frequencies compared to the case of a free electron in vacuum: The cyclotron energy $\hbar\omega_c$ amounts to 1.72 meV in bulk GaAs at 1 T. In reciprocal space, the occupied conduction band states at zero field are situated within the Fermi sphere with a radius of $k_F = \sqrt{2m_e^*E_F/\hbar^2}$. At finite magnetic field, the electrons are redistributed onto the surfaces of the so-called Landau tubes which correspond to the Landau levels $\hbar\omega_c(1/2 + n)$, $n = 0, 1, 2, \dots$. The radii of the tubes and the distances between them increase with magnetic field and, when one Landau tube cuts the Fermi surface, the electrons populate lower Landau tubes. Hence, the total energy of the electron oscillates while increasing the magnetic field. These oscillations are smeared by the momentum relaxation of the electrons. However, if the lowest Landau level exceeds the

⁵Throughout this work, the direction of an external magnetic field is along the x -direction if not stated otherwise.

Fermi energy, the total energy of the electronic system will no longer oscillate, but will monotonously increase with the magnetic field with a slope of $\hbar\omega_c/2B$. This behavior sets in at a magnetic field that is approximated by [65]

$$B = \sqrt[3]{\frac{4}{9} \frac{E_F m_e^*}{\hbar e}}. \quad (2.18)$$

The spectrum of eigenstates can significantly differ from the energies in Equation (2.17) if an additional localization potential is present. In the case of a two-dimensional electron with a harmonic localization potential, the eigenstates are given by the so-called Fock-Darwin spectrum [66, 67] which can be calculated analytically. For a single donor-bound electron, the localization potential is given by the coulomb potential and this problem has only been solved approximately [68]. If the cyclotron energy exceeds the effective Rydberg energy by far ($\nu = \hbar\omega_c/2E_{Ry}^* \gg 1$), again, an increase of the electronic energy in a magnetic field with a slope converging to $e/2m_e^*$ is expected. The binding energy for the magnetic field range used in this work ($\nu < 0.5$) is listed, e.g., in Reference 69.

2.2.4. Mechanisms of spin dephasing

The time evolution for a single spin is already derived in Equation (2.15). In this section, not a single spin but the spin polarization \mathbf{m} of an electron ensemble is considered. To this end, also spin dephasing and spin relaxation have to be accounted for. The resulting equation of motion is known as Bloch equation [21]:

$$\begin{aligned} \frac{\partial m_x}{\partial t} &= \frac{\mu_B g^*}{\hbar} (\mathbf{m} \times \mathbf{B})_x - \frac{m_x - m_{x,0}}{T_1}, \\ \frac{\partial m_y}{\partial t} &= \frac{\mu_B g^*}{\hbar} (\mathbf{m} \times \mathbf{B})_y - \frac{m_y}{T_2}, \\ \frac{\partial m_z}{\partial t} &= \frac{\mu_B g^*}{\hbar} (\mathbf{m} \times \mathbf{B})_z - \frac{m_z}{T_2}, \end{aligned} \quad (2.19)$$

where the spin dephasing time T_2 as well as the spin relaxation time T_1 are introduced phenomenologically. The quantity $m_{x,0}$ describes the

equilibrium spin polarization along the external field. Relaxation to the equilibrium value $m_{x,0}$ is accompanied by energy dissipation while the spin polarization transverse to the magnetic field usually dephases with the energy of the spin system being conserved. This work focuses mainly on spin dephasing, however, the physical difference between spin dephasing and relaxation blurs at the relatively low magnetic fields used in most spin noise spectroscopy experiments, resulting in $T_1 \simeq T_2$. Spin dephasing can either be of homogeneous or of inhomogeneous nature. Inhomogeneous spin dephasing is for instance observed when an electronic ensemble is probed in which all electrons experience different magnetic fields or have different effective g -factors. Inhomogeneous—contrary to homogeneous—spin dephasing is reversible which means that the spin orientation can be recovered in spin echo experiments; the corresponding inhomogeneous spin dephasing time is denoted by T_2^* [5]. Strictly speaking, inhomogeneous spin dephasing is not described by Equation (2.19) as the corresponding decay of the spin polarization is non-exponential.

In order to discuss the different mechanisms of spin dephasing, the random walk formalism of Pines and Slichter is adopted [70], which lucidly displays the main features of the particular mechanisms. Pines and Slichter consider a spin in interaction with its environment. This interaction results in an average change of the spin direction by an angle of $\delta\phi$ in the time span τ_c where τ_c is the correlation time of the given interaction. The change of the angle varies its sign with this time constant due to scattering events. The mean square of the rotational phase change of the spin after time t is given by

$$\langle \Delta\phi^2 \rangle \sim (\delta\phi)^2 t / \tau_c. \quad (2.20)$$

Pines and Slichter define T_2 to be the time after which $\langle \Delta\phi^2 \rangle$ reaches unity, a definition that is closely related to the one in Equation (2.19). In the following, three cases have to be considered: In the first case (*i*), the change of the rotational frequency occurs during the scattering event itself. The spin dephasing time becomes [71]

$$1/T_2 \sim (\delta\phi)^2 / \tau_c. \quad (2.21)$$

In the second case (*ii*), the interaction occurs during the whole time span of τ_c resulting in a change of the precession frequency ω by $\delta\omega \sim \delta\phi/\tau_c$. Consequently, the spin dephasing time reads

$$1/T_2 \sim (\delta\omega)^2\tau_c. \quad (2.22)$$

Thereby, the spin dephasing becomes less efficient at shorter correlation times τ_c . This concept of motional narrowing was first put forward by Bloembergen *et al.* to account for the narrow linewidths found in the nuclear magnetic resonance spectra of liquids [72]. If an additional external field is applied so that $\omega_L\tau_c > 1$, $\delta\phi$ never exceeds $\delta\omega/\omega_L$ [11]. In this case, Equation (2.20) yields

$$T_2(B) = T_2(0) (\omega_L\tau_c)^2 \text{ for } \omega_L\tau_c > 1. \quad (2.23)$$

Since $T_2(B) \rightarrow T_2(0)$ for $B \rightarrow 0$, the following expression is extrapolated from Equation (2.23) [11]

$$\frac{1}{T_2(B)} = \frac{1}{T_2(0)} \frac{1}{1 + (\omega_L\tau_c)^2}. \quad (2.24)$$

In the third case (*iii*), the correlation time is large compared to $1/\delta\omega$, i.e., the spin polarization has decayed before the first scattering event occurs and τ_c has to be replaced by T_2 in Equation (2.22), resulting in

$$1/T_2^* \sim \delta\omega. \quad (2.25)$$

In general, spin dephasing mechanisms can be assigned to one of the three above cases. The underlying interaction is in most cases either based on spin-orbit interaction (Elliott-Yafet mechanism, Dyakonov-Perel mechanism, and spin dephasing by random Rashba fields, by anisotropic exchange interaction, as well as by g -factor inhomogeneities) or on the hyperfine interaction. Since localized electronic states have a total quasi momentum of $k = 0$, spin dephasing via spin-orbit interaction is usually ineffective for these electronic states. However in impurity bands, where the electronic spin can diffuse from one donor to the other via exchange interaction or electron hops, spin-orbit interaction is again effective (see paragraph ‘‘Spin dephasing by anisotropic

exchange interaction”). Spin-orbit interaction also results in the energy dependence of the effective g -factor [see Equation (2.14)] which can yield an inhomogeneous distribution of g^* and subsequent spin dephasing in a transverse magnetic field. The spin dephasing of strongly localized carriers at low magnetic fields is dominated by hyperfine interaction and is included in this section for the sake of completeness. The Bir-Aronov-Pikus mechanism is only effective when holes as well as electrons are present in the sample and does not contribute to spin dephasing at thermal equilibrium. The following discussion also shows that excitation of the sample away from thermal equilibrium can significantly alter the observed spin dynamics in doped GaAs. Optical excitation heats the electron ensemble and also yields photogeneration of free electrons and holes. The presence of holes increases the spin dephasing due to the Bir-Aronov-Pikus mechanism while the presence of free electrons yields enhanced exchange averaging of the investigated spin ensemble which strongly influences the spin dephasing of localized carriers.

Elliott-Yafet mechanism. The Elliott-Yafet mechanism is based on the fact that electronic Bloch states are because of spin-orbit coupling not pure spin-up or spin-down states but superpositions of both [73, 74], e.g., $\Psi_{CB,\mathbf{k}\uparrow} = [a_{CB,\mathbf{k}}(\mathbf{r})|\uparrow\rangle + b_{CB,\mathbf{k}}(\mathbf{r})|\downarrow\rangle]e^{i\mathbf{k}\cdot\mathbf{r}}$. This admixture of the other spin species is small ($|b| \ll 1$). Nevertheless, scattering into another \mathbf{k} -state comes along with a finite possibility of a spin-flip. Correspondingly, the Elliott-Yafet mechanism is of the form given by Equation (2.21) [5]:

$$1/T_2^{\text{EY}} \sim \langle b^2 \rangle / \tau_p^*, \quad (2.26)$$

where τ_p^* is the momentum scattering time. Qualitatively, it does not matter which process gives the main channel for momentum relaxation. Either scattering due to impurity atoms [73], phonons [74], or electron-electron interaction [75] lead to spin relaxation via the Elliott-Yafet mechanism.⁶ Obviously, all of these underlying scattering mechanisms obey an energy or temperature dependence and, consequently, optical

⁶The quantity τ_p^* denotes the momentum scattering time including electron-electron scattering, which keeps the total momentum of the electron system constant, contrary to τ_p that can be deduced from mobility measurements.

excitation will alter the efficiency of spin dephasing. Nevertheless, not only the correlation time is energy dependent, but also the size of the spin-down admixture b varies with the electronic energy. For III-V semiconductors, like GaAs, Equation (2.26) becomes [71, 76]

$$1/T_2^{\text{EY}}(E) \propto E^2/\tau_p^*(E). \quad (2.27)$$

Recently, Jiang and Wu theoretically studied the relative strength of the Elliott-Yafet mechanism to other mechanisms concluding that the Elliott-Yafet mechanism is unimportant in most III-V semiconductors at low magnetic fields [77].

Dyakonov-Perel mechanism. As already discussed in Section 2.2.1, spin-orbit coupling in non-centrosymmetric semiconductor structures becomes manifest in spin-split energy bands. The lack of inversion symmetry can either result from bulk inversion asymmetry as in GaAs [Dresselhaus spin splitting, see Equation (2.5)], from structure inversion asymmetry as in asymmetrically doped quantum wells (Rashba spin-splitting) [78, 79], or from interface inversion asymmetry (see, e.g., Reference 80). However, at GaAs/AlGaAs interfaces, the interface asymmetry plays no crucial role [81, Chapter 2]. The spin splitting can be described by an effective, wavevector dependent magnetic field [see Equations (2.12) and (2.4)]. Hence, spins of electrons in different \mathbf{k} -states precess around different effective magnetic field vectors and, subsequently, a spin polarization dephases due to the so-called Dyakonov-Perel mechanism [52]. The correlation time of this interaction is again given by the momentum scattering rate including scattering due to impurities, phonons, and electron-electron interaction. The relevance of electron-electron scattering to the Dyakonov-Perel mechanism was pointed out by Wu and Ning [82, 83] as well as by Glazov and Ivchenko [84, 85].

For $\tau_p^* \ll 1/\omega$, which is most often the case, the Dyakonov-Perel mechanism is of the type given by Equation (2.22):⁷

$$1/T_2^{\text{DP I}} \sim \langle \Omega^2 \rangle \tau_p^*. \quad (2.28)$$

⁷The corresponding spin-orbit field has to be averaged over momentum space (see Reference 11).

2. Equilibrium Spin Fluctuations in GaAs

The Dresselhaus spin-splitting for bulk GaAs is cubic in \mathbf{k} [51] [see Equation (2.5)]. Thus, as for the Elliot-Yafet mechanism, not only the momentum relaxation time but also the strength of the spin-orbit coupling becomes energy dependent and varies by moving away from thermal equilibrium:

$$1/T_2^{\text{DP I}}(E) \propto E^3 \tau_p^*(E). \quad (2.29)$$

Since the Dyakonov-Perel mechanism is effective for free electrons, the cyclotron motion yields a weakening of the spin dephasing if $\omega_c \tau_c > 1$. Ivchenko deduced [11]

$$1/T_2(B) = 1/T_2(0) \left[1 - C (\omega_c \tau_c)^2 \right], \quad (2.30)$$

where the constant C depends on the type of the scattering process. As $\omega_c/\omega_L = 2m_e/m_e^* g^* \approx 70$ in bulk GaAs, the following magnetic field dependence of the Dyakonov-Perel spin dephasing rate is expected: (a) no significant change up to fields that correspond to $\omega_c \tau_c \approx 1$, (b) decrease and subsequent saturation of the dephasing rate until $\omega_c \tau_c \gg 1$, (c) a further decrease according to Equation (2.23) at $\omega_L \tau_c > 1$. Note that this discussion is independent of the direction of the applied magnetic field.

The Dresselhaus spin splitting is modified in quantum wells where the quasi momentum in the growth direction k_z is determined by momentum quantization [86], i.e.,

$$\begin{aligned} \langle k_z \rangle &= 0, \\ \langle k_z^2 \rangle &\approx \left(\frac{\pi}{l} \right)^2, \end{aligned} \quad (2.31)$$

where l is the width of the quantum well. For further calculation, the coordinate system of the crystal has to be transformed onto the coordinate system of the quantum well with the z -axis along the growth direction. An interesting case results for (110)-oriented quantum wells, which are also investigated in this work. The Dresselhaus field is given

by [86]

$$\boldsymbol{\Omega}_D^{(110)} = -\frac{\gamma_D \langle k_z^2 \rangle}{\hbar} [0, 0, k_x], \quad (2.32)$$

where the x -axis is chosen along $[1\bar{1}0]$. Hence, spins aligned along the growth direction in (110)-grown quantum wells do not dephase due to bulk inversion asymmetry.

Also a possible structure inversion asymmetry has to be considered in quantum well structures. The corresponding Rashba field is given by

$$\boldsymbol{\Omega}_R = \frac{2\alpha_R}{\hbar} [k_y, -k_x, 0], \quad (2.33)$$

where $\alpha_R = \xi e \mathcal{E}_z$ is the Rashba coefficient. Here, ξ is a material and structure dependent parameter of the unit length squared and \mathcal{E}_z denotes the electrical field along the quantum well that results, e.g., from asymmetric doping.

In systems with very low momentum scattering rates as in high mobility quantum wells at ultralow temperatures [87, 88], the Dyakonov-Perel process is described by Equation (2.25):

$$1/T_2^{\text{DP}} \Pi^* \sim \langle \Omega \rangle. \quad (2.34)$$

Spin dephasing by random Rashba fields. As expounded in the previous paragraph, the Dyakonov-Perel mechanism is only present in system lacking inversion symmetry. Accordingly, modulation-doped quantum well structures with symmetrically grown doping sheets exhibit no structural inversion asymmetry and, therefore, no Rashba fields should be present. The structural inversion symmetry, however, only exists on a mesoscopic scale. On a microscopic scale, there are inevitable, spatial fluctuations of the impurity density in the doping sheets. Hence, the disorder in the doping layers results in random electrical fields that in turn yield Rashba fields. These random Rashba fields induce spin dephasing of a two-dimensional electron gas in a modulation-doped quantum well. This mechanism was first suggested and studied by Sherman [89]. Assuming thin doping sheets and a totally uncorrelated spatial distribution of impurity atoms in the doping sheet, the disorder domains have an estimated size of πR_d^2 with R_d being the distance between the mid-

2. Equilibrium Spin Fluctuations in GaAs

dle of the quantum well and the remote doping layer [90]. The variance of the electric field along the growth axis z is calculated to be

$$\langle \mathcal{E}_z^2 \rangle = 2\pi \left(\frac{e}{4\pi\epsilon_0\epsilon} \right)^2 \frac{n_D}{R_d^2}, \quad (2.35)$$

where n_D is the two-dimensional electron density in the quantum well which coincides with the impurity density in the remote doping sheets in a multiple well quantum well structure (neglecting the outmost doping sheets) as depicted in Figure 3.11.⁸ According to Equation (2.35), the relevant dopant fluctuations in one doping layer are of the order of $1/\sqrt{\pi R_d^2 n_D}$. In GaAs/AlGaAs structures, the time of passage through one disorder domain τ_d is usually shorter than the momentum scattering time including electron-electron scattering τ_p^* [90]. Hence, the correlation time of the spin-orbit interaction is given by the passage time which is a crucial difference to the usual Dyakonov-Perel spin dephasing. Correspondingly, the passage time in one disorder domain can be calculated in the ballistic regime [90], i.e.,

$$\tau_d = \frac{R_d}{v_F}, \quad (2.36)$$

where v_F is the Fermi velocity of the electron gas. Obviously, random spin orbit coupling in a two-dimensional electron gas results in spin dephasing of the type given by Equation (2.22). The size of the spin-orbit field is—as in the case of spin dephasing in mesoscopic Rashba fields—proportional to electron momentum, the electric field size and the material dependent constant ξ . Overall, the spin dephasing time due to random Rashba fields can be estimated as [90]

$$1/T_2^{\text{RR}} \sim \left(\xi e \sqrt{\langle \mathcal{E}_z^2 \rangle} k_F / \hbar \right)^2 \tau_d. \quad (2.37)$$

Spin dephasing due to g -factor inhomogeneities. At finite temperatures, the Fermi distribution in the conduction band is broadened by $k_B T$. Due to the energy dependent effective g -factor [Equation (2.14)],

⁸Screening of the electric fields from the adjacent quantum well in a multiple quantum well structure can be neglected in most practical cases [90].

electrons at different energies show different effective Landé factors. The momentum state of the electrons however changes with the momentum scattering time τ_p^* . Hence, a spin polarization transverse to an external magnetic field dephases according to Equation (2.22) [91]:

$$1/T_2^{\text{IGI}} \sim (\sigma_{g^*} \mu_B B / \hbar)^2 \tau_p^*, \quad (2.38)$$

where the standard deviation $\sigma_{g^*} = \sqrt{\langle g^{*2} \rangle - \langle g^* \rangle^2}$ results from averaging over reciprocal space. Due to fast momentum scattering, this effect is usually negligible at moderate fields ($B < 10$ T) [92]. The variance of the effective g -factor can however also result from spatial inhomogeneities for localized carriers as in quantum dot ensembles. In this case, the spin polarization dephases according to Equation (2.25):

$$1/T_2^{\text{IGII}^*} \sim \sigma_{g^*} \mu_B B / \hbar. \quad (2.39)$$

Here, σ_{g^*} results contrary to Equation (2.38) from spatial averaging.

Bir-Aronov-Pikus mechanism. Optical spin orientation is necessarily accompanied by the creation of electron-hole pairs in a semiconductor. Thus, away from thermal equilibrium, electrons and holes can be present in the sample, which leads to additional spin dephasing. Bir *et al.* showed that the electron spin in presence of holes dephases due to exchange interaction between electrons and holes [93]. The strength of this Bir-Aronov-Pikus mechanism depends on the hole density, the electron-hole overlap, and the fact whether holes are bound or delocalized. The Bir-Aronov-Pikus mechanism shows distinct regimes with different dependencies on the hole density [11]. Qualitatively, in all of these regimes, the efficiency of electron spin dephasing is increasing with hole density. Also, the temperature dependence does not follow a simple expression and varies for the different regimes: Nevertheless, for fixed hole density, the electron-hole overlap increases with decreasing temperatures and, accordingly, the Bir-Aronov-Pikus mechanism gets more efficient. While it is clear experimental evidence that the Bir-Aronov-Pikus mechanism significantly contributes to spin dephasing in the absence of other spin dephasing processes [44], its relative strength compared to other mechanisms has become subject of scientific discus-

sion (see References 94 and 95).

Spin dephasing by hyperfine coupling. In GaAs all lattice nuclei have a finite spin. The electronic spin interacts with the spins of the lattice nuclei due to the Fermi contact interaction. This hyperfine coupling represents an interface between electronic and nuclear spins, as proposed by Overhauser in 1953 for the case of metals [96]. In a semiconductor, an electronic spin polarization creates a nuclear spin polarization on the laboratory timescale which in turn strongly influences the electronic spin dynamics [1, 97, 98]. Spin dephasing due to hyperfine interaction in semiconductors was first theoretically investigated by Dyakonov and Perel [97] and later extensively discussed by Merkulov *et al.* [99]. Depending on the number of lattice nuclei carrying a nuclear spin and the extension of the donor wavefunction, a localized electronic spin interacts with a certain number of nuclear spins N_L ; in GaAs $N_L \approx 2 \times 10^5$. Recalling the prediction of nuclear spin noise by Bloch [21], an average stochastic polarization of $\sqrt{N_L}$ nuclear spins is present at thermal equilibrium. This hyperfine interaction leads to an electronic spin precession with an average frequency $\langle \Omega_{\text{HF}} \rangle$ in the nuclear magnetic field, the so called Overhauser field. An expression to calculate this field is given in Reference 99 (see also References 100 and 101) and amounts to around 7 mT in GaAs. The nuclear spins themselves precess in the magnetic field of the electron, the so-called Knight field, which is a factor of $\sqrt{N_L}$ smaller than the Overhauser field. Hence, the precessional frequency of the nuclear spin is significantly smaller than for the electrons and, in the first step, the nuclear spin polarization can be viewed as frozen. The correlation time τ_c of the hyperfine interaction is determined by the strength of electronic localization, i.e, by the time an electronic spin resides at a certain donor site. Spin diffusion via exchange interaction occurs orders of magnitude faster than electronic hopping in the low doping regime [102] so that $\tau_c \approx \hbar/J$ [102, 103] is given by the exchange integral between remote donor states J . In the intermediate doping regime below the metal-to-insulator transition, where $\langle \Omega_{\text{HF}} \rangle \tau_c \ll 1$, a spin polarization dephases according to Equation (2.22) with a rate of [102]

$$1/T_2^{\text{HF I}} \sim \langle \Omega_{\text{HF}}^2 \rangle \tau_c. \quad (2.40)$$

Therefore, spin dephasing based upon hyperfine interaction becomes less efficient with increasing doping concentrations and is completely negligible in the metallic state. Nevertheless, also the creation of additional free carriers by optical spin orientation yields efficient exchange averaging of the hyperfine fields [98, 104]. In the regime of very low doping and low temperatures, where electrons are considered as non-interacting and strongly localized, no motional narrowing occurs, i.e., $\langle \Omega_{\text{HF}} \rangle \tau_c \gg 1$ and, due to the stochastic nuclear spin polarization, a spin ensemble is subject to inhomogeneous spin dephasing according to Equation (2.25):

$$1/T_2^{\text{HF II}^*} \sim \langle \Omega_{\text{HF}} \rangle. \quad (2.41)$$

However, Equations (2.40) and (2.41) only describe the decay of the spin components perpendicular to the Overhauser field at the particular donor sites. In the absence of an external magnetic field, the angle between electronic and nuclear magnetic field is conserved during the electronic spin precession period. Hence, one third of the spin polarization of a spin ensemble does not dephase on the timescale of the electronic but of the nuclear precession period as predicted by Merkulov *et al.* [99] and experimentally demonstrated by Braun *et al.* [101]. Due to the spatial variation of the electronic wavefunction, the Knight field is spatially inhomogeneous and different nuclei at a given donor site have different precessional frequencies. Subsequently, the angle between electronic and nuclear spin is not conserved on the timescale of the nuclear spin precession. Thus, the spin component randomly aligned with the nuclear field undergoes spin dephasing with a roughly estimated rate of

$$1/T_2^{\text{HF III}^*} \sim \langle \Omega_{\text{HF}} \rangle / \sqrt{N_{\text{L}}}. \quad (2.42)$$

Spin dephasing by anisotropic exchange interaction. The exchange interaction is mentioned as an origin of motional narrowing of the hyperfine induced spin dephasing in the last paragraph. However, in semiconductors without spatial inversion symmetry, the exchange interaction itself is in connection with spin-orbit coupling a source of spin dephasing for localized electronic spins. Due to spin-orbit coupling and a crystalline structure lacking spatial inversion symmetry, the exchange interaction between two spins is not described by a Heisenberg-type

Hamiltonian of the form $\mathbf{s}_1 \cdot \mathbf{s}_2$ but by means of a second rank tensor. The antisymmetric part of this tensor gives rise to an anisotropic exchange interaction or the so called Dzyaloshinskii-Moriya interaction [105, 106]. Kavokin was the first to suggest in 2001 that spin tunneling from one donor site to another will in average encounter a finite rotation of γ due to this anisotropic exchange interaction [107]. Hence, the Dzyaloshinskii-Moriya interaction gives rise to spin dephasing of the type of Equation (2.21):

$$1/T_2^{\text{DM}} \sim \gamma^2/\tau_c, \quad (2.43)$$

where the time between two spin diffusion events $\tau_c \approx \hbar/J$ [102, 103] is, as in the previous paragraph, given by the isotropic part of the exchange interaction J . Obviously, enhanced exchange averaging by photocreation of free carriers yields strongly reduced spin dephasing times [17]. Electron hopping contributes to spin dephasing analogously [102, 108]. Spin dephasing due to the anisotropic exchange interaction is expected to dominate spin dephasing at the metal-to-insulator transition and spin noise spectroscopy yields spin dephasing times around 300 ns that are in good agreement with theoretically expected values [17]. The magnetic field dependence of these spin dephasing mechanisms is expected to be rather complex due to a variety of different effects [102] (see also Section 4.2).

2.3. Spin noise of donor-bound electrons

In a low doped semiconductor system, where the donor electrons are localized at the impurity atoms and non-interacting with each other, spin noise spectroscopy probes the donor-bound exciton transition ($\hbar\omega_{\text{D}^0\text{X}} = E_{\text{G}} - E_{\text{D}^0\text{X}}$). Here, E_{G} is the fundamental absorption edge and $E_{\text{D}^0\text{X}}$ is the binding energy of the exciton-neutral donor complex D^0X [109]. Since the donor electrons do not interact with each other, the number of spin-up(down) electrons $N^{\uparrow(\downarrow)}$ follows a binomial distribution with mean $\langle N^{\uparrow(\downarrow)} \rangle = 0.5N$ and standard deviation $\sigma_{N^{\uparrow(\downarrow)}} = 0.5\sqrt{N}$. Here, $N = N^{\uparrow} + N^{\downarrow} = n_{\text{D}}V$ is the total number of donor electrons within the probe volume V . Thus, the standard deviation of the stochastic spin

polarization m_z of the donor-bound electrons is given by

$$\begin{aligned}\sigma_{m_z} &= \frac{2\sigma_{N\uparrow(\downarrow)}}{N}, \\ &= \frac{1}{\sqrt{N}}.\end{aligned}\quad (2.44)$$

Neglecting the spin, the Drude-Lorentz oscillator model describes this optical transition as a sum of N harmonic oscillators with oscillator strength f . Within this model (see, e.g., Reference 110), the absorption constant α and the dissipative part of the refractive index n' can be written as [111]

$$\begin{aligned}\alpha &= n' \frac{2\omega_{\text{laser}}}{c_0}, \\ &= \frac{e^2 f n_{\text{D}}}{8m_e^* \epsilon_0 \omega_{\text{D}^0\text{X}} \sqrt{\epsilon_{\text{r}}}} \frac{\Gamma}{(\omega_{\text{laser}} - \omega_{\text{D}^0\text{X}})^2 + \Gamma^2/4} \frac{2\omega_{\text{laser}}}{c_0},\end{aligned}\quad (2.45)$$

where dispersive and dissipative contributions from far-detuned transitions are subsumed by the background dielectric constant ϵ_{r} and Γ is the width of the optical transition. The corresponding dispersive part of refractive index is given by [111]

$$\begin{aligned}n &= n_{\text{B}} + \tilde{n}, \\ &= \sqrt{\epsilon_{\text{r}}} - \frac{e^2 f n_{\text{D}}}{4m_e^* \epsilon_0 \omega_{\text{D}^0\text{X}} \sqrt{\epsilon_{\text{r}}}} \frac{\omega_{\text{laser}} - \omega_{\text{D}^0\text{X}}}{(\omega_{\text{laser}} - \omega_{\text{D}^0\text{X}})^2 + \Gamma^2/4}.\end{aligned}\quad (2.46)$$

Thus, the deviation of the real part of the refractive index from $n_{\text{B}} = \sqrt{\epsilon_{\text{r}}}$ decreases linearly with inverse detuning and the absorbed energy decreases with the inverse detuning squared. In other words, for off-resonant probing the change of the refractive index is finite even at negligible absorption (see Figure 2.3).

A stochastic spin imbalance m_z yields a circular dichroism due to the optical selection rules, i.e., different constants of absorption α^+ and α^-

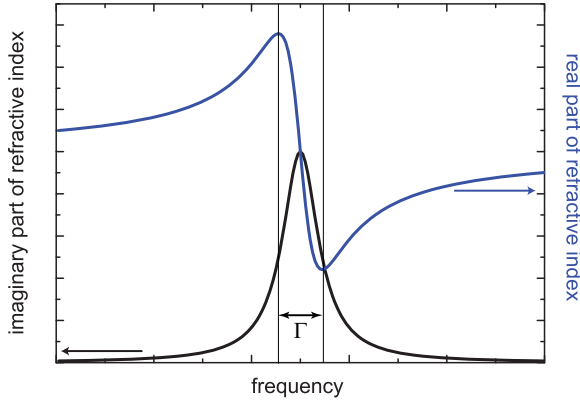


Figure 2.3.: Dissipative and dispersive part of the refractive index of an optical transition according to the Drude-Lorentz oscillator model.

for σ^+ and σ^- light,

$$\begin{aligned}\Delta\alpha &= \alpha^+ - \alpha^- \\ &= \zeta m_z \alpha,\end{aligned}\tag{2.47}$$

as well as a circular birefringence, i.e., different indices of refraction n^+ and n^- for σ^+ and σ^- light,

$$\begin{aligned}\Delta n &= n^+ - n^- \\ &= \zeta m_z \tilde{n},\end{aligned}\tag{2.48}$$

where the factor $\zeta = 0.5$ for bulk GaAs is determined by the optical selection rules [see Equation (2.6)]. If the probe beam waist w_0 within the sample can be viewed as constant on the length scale of the sample thickness l , the circular birefringence amounts to a Faraday rotation angle of

$$\theta_{\text{F}} = \pi \Delta n l / \lambda,\tag{2.49}$$

where λ is probe light wavelength in vacuum. According to Equa-

tion (2.44), the observed integrated spin noise power reads:

$$P = \sigma_{\theta_F}^2 = \frac{\pi^2 \zeta^2 \tilde{n}^2 l}{\lambda_0^2 n_D A}. \quad (2.50)$$

Here, $A = \pi w_0^2$ is the laser spot area and θ_F is assumed to be small. Of course, Equation (2.50) is only valid if the probe volume V is large compared to the inverse of the doping concentration n_D , which is nearly always the case.

Note that Faraday rotation is usually independent of the laser spot area A , but in the case of spin noise spectroscopy the stochastic spin polarization and thereby the Faraday rotation angle becomes larger for smaller probe laser spots, resulting in the $1/A$ relation in the above equation.

2.4. Spin noise of conduction band electrons

Next, a GaAs system with a doping level well above the metal-to-insulator transition is considered. In such a sample system, the Fermi energy lies within the conduction band. The two main differences to very low doped samples are that *(i)* electrons are degenerate and Fermi-Dirac statistics have to be applied and that *(ii)* the interband transition is described by a sum of Drude-Lorentz oscillators with different resonant energies. The stochastic spin polarization in this systems varies with the energy position in the conduction band. According to the Pauli principle, the variance of the spin imbalance is determined by the number of occupied and unoccupied electronic states around the Fermi level:

$$\sigma_{m_z}^2(E) \propto f(E) [1 - f(E)]. \quad (2.51)$$

For a rigorous calculation, the given absorption spectrum $\alpha(E)$ has to be modeled by a sum of Drude-Lorentz oscillators with different resonance energies and an energy dependent spin polarization. From a more practical viewpoint—due to the term $f(E) [1 - f(E)]$ —a spin noise contribution at low temperatures is only expected from electrons within a width of $k_B T$ around the Fermi energy E_F . Also, the optical absorption sets in at energies around $E_F + E_G$. Hence, the signal strength can be

approximated at low temperatures by calculating the optical transitions by a single Drude-Lorentz oscillator centered around E_F and assuming noise contributions from electrons with a carrier density reduced by a factor F [42, 112]:⁹

$$F \times n_D = \int_{E_G}^{\infty} f(E) [1 - f(E)] D(E) dE. \quad (2.52)$$

At this stage, it is important to note that the amount of observed spin noise power gives information about the underlying electron statistics, i.e., the integrated spin noise power of localized non-interacting electrons is temperature independent while the spin noise power of fully delocalized electrons vanishes at zero temperature due to Pauli spin blockade ($F = 0$). In other words, the amount of spin noise power extrapolated to zero temperature is a measure of the degree of electron localization [100].

2.5. Spectral shape of spin noise

In the previous paragraphs, it is elaborated that fluctuations of the z -component of the electron spin polarization in the sample are mapped onto the linear light polarization. Of course, these fluctuations are not completely random but exhibit correlations in time determined by the underlying spin dynamics. According to Equation (2.19),¹⁰ the relevant auto-correlation function is given by [113]

$$\langle s_z(0) s_z(t) \rangle \propto \cos \omega_L t e^{-t/T_2} \text{ for } t > 0. \quad (2.53)$$

The Wiener-Chintchin theorem [114, 115] states that the Fourier transform of this expression is equal to the power spectrum of the spin fluctuations that are recorded in the time domain, i.e., the spectral power

⁹Contrary to the previous case of fully localized electrons, the amount of probed electrons $N = F n_D V$ is also subject to stochastic fluctuations. Hence, N_\uparrow and N_\downarrow are not fully correlated as in the previous case and Equation (2.44) is strictly not valid anymore.

¹⁰Here, the spatial correlations which result from the finite residence time of delocalized electrons in the probe volume are not considered. They can however have an important influence on the observed line width as discussed in Section 4.1.3.

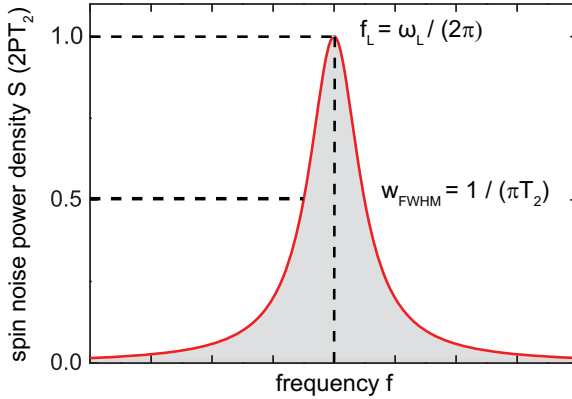


Figure 2.4.: Expected power spectrum of the spin fluctuations. The exponential spin dephasing yields a Lorentzian line shape. The spin noise spectrum is centered at the Larmor frequency; the width is given by the inverse dephasing time and the area under the curve gives the spin noise power P as calculated in Sections 2.3 and 2.4. Here, the noise power density is given in units of $S(f_L)$ according to Equation (2.54).

density of the total spin noise power P . The Fourier transform of such an exponentially damped spin oscillation¹¹ yields a Lorentzian shaped spectral spin noise spectrum [113]

$$S(f) = \frac{2P}{\pi} \frac{w_{\text{FWHM}}}{4 \left(f - \frac{\omega_L}{2\pi}\right)^2 + w_{\text{FWHM}}^2} \left[\frac{\text{rad}^2}{\text{Hz}} \right]. \quad (2.54)$$

Here, $w_{\text{FWHM}} = (\pi T_2)^{-1}$ denotes the full width at half maximum (FWHM) and P is the integrated spin noise power as calculated in Equation (2.50) (see Figure 2.4). Correspondingly, spin noise spectroscopy yields experimental access to the effective Landé g -factor and the spin dephasing time. In addition, the spin noise power is also a measure for the statistics of the electrons [see Equation (2.52)].

¹¹Note that inhomogeneous spin dephasing does not yield an exponential spin decay and should result in a Gaussian spin noise spectrum.

CHAPTER 3

Experimental Methods

The fundamentals of semiconductor spin noise spectroscopy are discussed in full detail in the previous chapter. This chapter focuses on the experimental realization of this measurement concept. The basic setup is introduced in Section 3.1. Section 3.2 discusses the relative strength of the spin noise signal to the laser shot noise background and the resulting experimental implications. The limitations of spin noise spectroscopy by the finite experimental bandwidth and possible routes for an extension to higher frequencies are examined in Section 3.2. For this purpose, electrical frequency mixing is applied for down-conversion of the spin noise signal (Section 3.3.1), the sensitivity of spin noise spectroscopy employing ultrafast, low-bit digitizers is inspected (Section 3.3.2), and the new experimental technique of ultrafast spin noise spectroscopy is introduced (Section 3.3.3). The specifics of the samples that are examined in this work are given in Section 3.4.

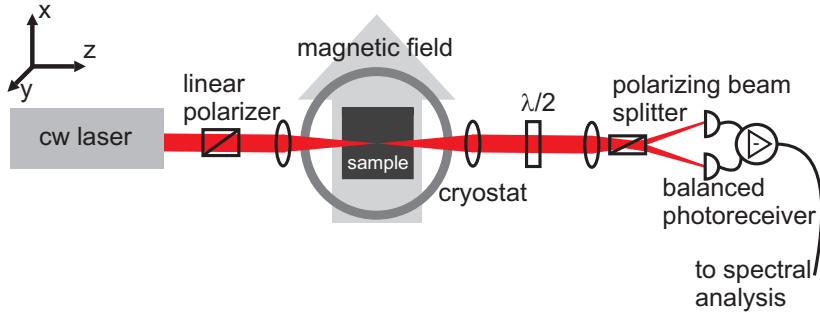


Figure 3.1.: Basic experimental setup for semiconductor spin noise spectroscopy.

3.1. Fundamental setup

In spin noise spectroscopy, the stochastic spin polarization in the investigated sample is measured. For this purpose, the spin fluctuations are mapped onto the direction of the linear light polarization of an off-resonant probe laser via the Faraday effect. The basic setup is depicted in Figure 3.1. In this setup, the laser system emits linearly polarized continuous-wave laser light. The sample is mounted in a cryostat, in which the sample temperature can be varied. Additionally, a magnetic field usually transverse to the wavevector of the probe light—the so called Voigt geometry—can be applied to modulate the spin dynamics via the Larmor frequency. The linearly polarized laser light, which has a wavelength within the transparency region of the sample, is transmitted through the sample and experiences a Faraday rotation. This Faraday rotation is measured by means of a balanced detection scheme, which consists of a balanced photoreceiver and a polarizing beam splitter that decomposes the probe light into the two orthogonal linear light components. The difference signal between the two photodiodes of the balanced receiver is for small rotation angles proportional to the Faraday rotation. The voltage output of the photoreceiver is spectrally analyzed. In the following, the main components of the setup are discussed in more detail.

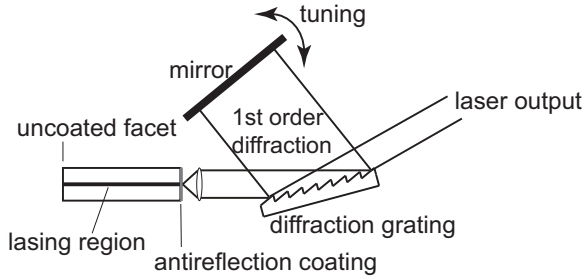


Figure 3.2.: Laser diode with external cavity in Littman geometry.

Laser system. The laser system that is used for all measurements in this work by means of conventional spin noise spectroscopy consists of a laser diode in an external cavity. External cavities are used to tune the laser wavelength to a narrow line within the gain spectrum of the laser diode [116]. In this work, the laser is operated in Littman configuration [117] (see Figure 3.2): The collimated output of the laser diode is directed on a diffraction grating and the first order diffracted beam is reflected by a mirror back onto the grating and the laser diode. The utilized laser diode¹ has an antireflection coated front facet and, hence, a laser resonator is formed between the back facet of the laser diode and the mirror. Since the grating is a dispersive element inside the cavity, tilting the cavity mirror tunes the resonantly amplified longitudinal mode. The system allows tuning from around 800 to 860 nm and the laser light is coupled out of the cavity as the zero order diffraction beam of the grating. The ellipsoidal beam profile of the outcoupled beam, which is typical for edge emitting quantum well laser diodes, is corrected by means of an anamorphic prism pair. Subsequently, the laser output is sent through an optical isolator to avoid back reflections into the cavity and focused onto a micron-sized pinhole to ensure a good spatial mode. For the measurements of Section 4.3, the spatial filtering is achieved by coupling the light into a single mode optical fiber. Typical probe laser powers in this work amount to 2 to 4 mW at the detector. Absorption by the sample is usually negligible with the

¹*Eagleyard Photonics EYP-RWE-0850-05010-1500-SOT02-0000.*

3. Experimental Methods

laser wavelength in the transparency region of the sample; however, a significant portion of probe laser power is lost due to reflection at the surfaces of the various optical elements and the sample although most surfaces are antireflection coated. Hence, the output power of the laser is usually 30 to 50% higher than the laser power at the photodetector.

Cryostat. In this work, three different helium based cryogenic systems are used. (i) For the measurements of the multiple quantum well structure (Section 4.1), an optical access to the sample with a high aperture is needed to ensure good focusing. This is achieved by the *Cryovac Konti-Kryostat-Mikro*, which cools the sample via a cold-finger. The temperature can be adjusted from around 3.5 K up to room temperature. For focusing on the sample, a microscope objective is used (*Nikon Plan Fluor ELWD 20x/0.45*) with a numerical aperture of 0.45. A knife edge test delivers the beam parameters: A beamwaist at the focus point of $w_0 \approx 3.5 \mu\text{m}$ with a corresponding Rayleigh range of $z_R \approx 3 \mu\text{m}$ is achieved.² For collimation of the transmitted probe light, a lens is mounted behind the sample within the refrigerator. Magnetic fields of up to 14 mT can be applied by a pair of coils with iron cores that are placed outside the cryostat. The magnetic field is carefully calibrated by a Hall probe. (ii) For the measurements in magnetic fields up to 3 T (Section 4.2), an *Oxford Instruments Spectromag* with a superconducting split coil magnet is used, which allows fields of up to 8 T. The sample is cooled in helium exchange gas and the sample temperature can be adjusted from helium temperatures up to room temperature. The probe laser is focused on the sample by achromatic lenses with a focus length of 250 mm. The magnetic field deviates strongly from the power supply readout and is carefully recalibrated by means of a Hall probe. The magnet is always degaussed when going to lower magnetic fields. (iii) The measurements in an oblique magnetic field with respect to the probe light wavevector (Section 4.3) are carried out in an optical helium-3/helium-4 dilution refrigerator (*Oxford DL-400*). This is a dry

²The measured beam parameters show a strong deviation from the relation for a purely Gaussian beam: $z_R = \pi w_0^2 / \lambda_0 M^2$. For a Gaussian beam $M = 1$ is expected, the measured beam parameters yield $M \approx 4$. This deviation motivates the replacement of the spatial filter by a single mode optical fiber for later measurements (see previous paragraph) which yields $M = 1.01$ [118].

system which means that the helium-3/helium-4 mixture is cooled by a closed helium-4 cycle and a pulse tube cooler. The thermal contact to the sample holder is achieved by copper wires which are connected to the mixing chamber. The sample temperature can be varied from below 100 mK up to 10 K. The actual investigation is however carried out at a moderate temperature of 2 K. Another feature of this system is a vector magnet which is essential for the experiment and allows application of magnetic fields in arbitrary directions. The vector magnet consists of three superconducting split coils with axes orthogonal to each other. A field of 2 T can be applied along the axis of light propagation and 200 mT in the two other orthogonal directions. Again the sample light is focused on the sample by an achromatic lens with a focus length of 250 mm.

Photoreceiver. The balanced receivers utilized for this work are the *New Focus 1607-AC-FS* with a 3 dB-bandwidth of 650 MHz (Sections 4.1 and 4.3) and the *New Focus 1807-FS* with a bandwidth of 80 MHz (Section 4.2). The silicon photodiodes of both devices have a responsivity of 0.5 A/W for the utilized wavelength region which corresponds to a quantum efficiency of around $\hbar\omega_{\text{laser}}/e \times 0.5 \text{ A/W} \approx 75\%$. The decisive quantity to calculate the Faraday rotation angle from the voltage output of the detector is the conversion gain which amounts to $\rho = 20000 \text{ V/W}$ (*New Focus 1807-FS*) and 700 V/W (*New Focus 1607-AC-FS*), respectively. The higher conversion gain comes along with lower relative electrical noise which is specified by the minimal noise-equivalent power of $3.3 \text{ pW}/\sqrt{\text{Hz}}$ compared to $40 \text{ pW}/\sqrt{\text{Hz}}$. This figure of merit is relevant for the signal-to-noise ratio at very low probe powers (see Section 3.2). Both receivers have a common mode rejection ratio of 25 dB, i.e., classical laser noise is suppressed by a factor of around 300. The voltage output of the photoreceiver is—if necessary—amplified by a low noise voltage amplifier to adjust the voltage amplitude to the optimal input load of the spectrum analyzer (see next paragraph and Section 3.3.2).

Spectrum analyzer. In the first realization of semiconductor spin noise spectroscopy [41], a sweeping spectrum analyzer was utilized for trans-

3. Experimental Methods

forming the acquired time signal into the frequency domain. However, a spectrum analyzer with a sweeping local oscillator measures the noise only at the reference frequency and thereby disregards the majority of the available data stream. Sweeping over 100 MHz bandwidth with a resolution of 0.1 MHz simply means that around 99.9% of the acquired signal remain unused at a time. This problem is avoided by digitizing the data stream and subsequent realtime spectrum analysis via fast Fourier transformation (FFT) that is used in this work. The FFT algorithm allows simultaneous detection of spin noise at all frequencies within the detection bandwidth and, hence, with no void time as long as all digitized data can be further processed. In other words, 100% of the signal acquired in the time domain enter into the data processing and averaging. FFT spectrum analysis yields an astonishing increase of the experimental sensitivity [17]. The actual realtime FFT analysis is perfectly suitable for parallel computing and, therefore, scalable to high data throughput; details about the implementation of the software based realtime FFT that was set up by Römer can be found in Reference 118.

The data transmission of the digitizer measured in bits/s is given by [119]

$$I = f_S \times R, \quad (3.1)$$

where f_S denotes the sampling rate and R the sample size or bit depth. In this work, the *Alazartech 9462 PCI Express* analog-to-digital converter ($f_S = 180 \text{ MS/s}$, $R = 16 \text{ bit}$) is used. According to the Nyquist-Shannon theorem [120, 121], the spin noise spectroscopy setup in Figure 3.1 can only detect spin noise at frequencies smaller than the detection bandwidth which is given by half of the sampling rate:

$$B = f_S/2. \quad (3.2)$$

It is important to cut off all shot noise at frequencies larger than B by means of low pass frequency filters. Otherwise, undersampling of these frequency components would result in an increased background noise level within the detection bandwidth. The bit depth determines the quantization error of a digitized signal, i.e., the difference between analog input and digital output. In the case of uniform quantization

and avoidance of overload at the digitizer, the variance of the quantization error is proportional to 2^{-2R} according to Bennett's approximation [122].³ Thus, the variance of the quantization error scales exponentially with the utilized number of bits per sample. Interestingly, the signal-to-noise ratio in spin noise spectroscopy is not limited by this quantity. A detailed understanding of the interplay of averaging and quantization errors is necessary to achieve the maximal sensitivity for spin noise spectroscopy (see Section 3.3.2).

3.2. Background noise and experimental implications

Besides the spin noise signal, also spurious noise sources contribute to the detected polarization fluctuations. In Section 3.2.1, these noise contributions are reviewed and the laser shot noise is identified as the main source. Furthermore, the relative signal strength is calculated for different sample systems. Section 3.2.2 focuses on the experimental methods to subtract the background noise from the signal, which are necessitated by the frequency-dependent amplification of the in theory white background noise level.

3.2.1. Background noise and relative signal strength

Classical laser noise. Classical laser noise due to intensity fluctuations mainly manifests itself as $1/f$ -noise [124]. The balanced detection scheme in Figure 3.1 is employed to reject classical noise of the laser system and $1/f$ -noise is usually negligible in the experiment down to frequencies of around 500 kHz.

Laser shot noise. In addition to the suppressible classical noise, quantum mechanical shot noise, which is a consequence of the photon nature of light, contributes to the measured polarization noise. Optical shot noise is—contrary to spin noise (see Section 2.5)—uncorrelated, i.e.,

³For a discussion of the validity of this approximation, see, e.g., Reference 123.

3. Experimental Methods

the idealized autocorrelation function of the electrical current that is generated in the detector reads

$$\langle i(t)i(t') \rangle \propto \delta(t - t'). \quad (3.3)$$

According to the Wiener-Chintchin theorem, the measured shot noise level can be calculated by the Fourier transform of this expression. A detailed derivation yields a shot noise power density of [124]

$$S_{\text{SN}} = 2\rho^2 \hbar \omega_{\text{laser}} P_{\text{laser}} \quad [\text{V}^2/\text{Hz}]. \quad (3.4)$$

Accordingly, a constant background noise level would be expected. However, due to the finite bandwidth of the detection system, every photogenerated electron corresponds to a current pulse in the detector of finite duration contrary to the modeling in Equation (3.3). Rectangular current pulses of a length of τ would correspondingly result in a frequency dependent shot noise level:

$$S_{\text{SN}}(f) \propto \left[\frac{\sin(\pi\tau f)}{\pi\tau f} \right]^2. \quad (3.5)$$

Figure 3.3 (a) depicts the noise power density at 1 MHz as a function of the probe laser power at the detector which is measured in the experimental setup of Figure 3.1 without a sample. The utilized photodetector is the *New Focus 1807-FS*, the laser wavelength is tuned to 833.5 nm. The absolute values are in excellent agreement with Equation (3.4) and the specified conversion gain. The dashed line indicates the residual amount of detected noise at vanishing probe power which is clearly negligible at 1 MHz. Hence, the measurement sensitivity in this frequency region, where classical laser noise as well as further electrical noise are negligible, is very close to the standard quantum limit, i.e., at its theoretical maximum. The conversion gain however decreases at higher frequencies: Figure 3.3 (b) depicts the background noise power density at 50 MHz. The linear fit corresponds to a conversion gain of $\rho = 15000 \text{ V/W}$ while also the amount of dark noise has slightly increased. Still, also at higher frequencies optical shot noise is the major source of background noise and further noise sources can be largely

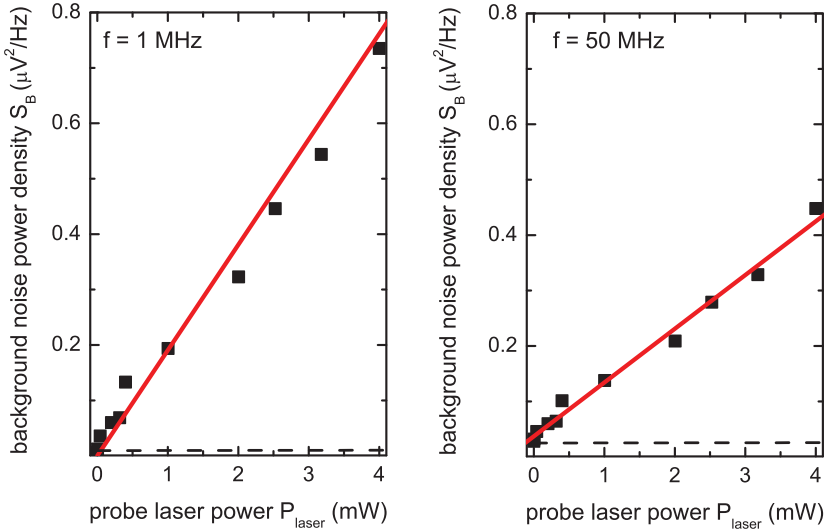


Figure 3.3.: (a) Background noise level as a function of laser power at 1 MHz. The dashed line gives the dark noise of the photodetector. The linear increase results from optical shot noise power and the solid line is calculated according to Equation (3.4). (b) Same as in (a), however at 50 MHz; the solid line is a linear fit that corresponds to 75% of the conversion gain in (a).

neglected at moderately high probe laser powers.

Other noise sources. The electronic components, like detector and the amplifier, introduce additional electrical noise. The dark noise that is detected for vanishing probe power amounts to $0.036 \mu\text{V}^2/\text{Hz}$ at 1 MHz is in good agreement with the specified noise equivalent power (see Section 3.1) which corresponds to a dark noise power density of $0.016 \mu\text{V}^2/\text{Hz}$. The dark noise power density is by a factor of 5 higher at 50 MHz, but still all other spurious noise contributions can be neglected in this work where moderately high laser powers of several mW are used. In Section 3.3.2, also the noise resulting from the quantization

3. Experimental Methods

by the digitizer is considered which however is also negligible for the digitizer utilized in this work at proper input load.

Relative signal strength. The peak spin noise power density at the detector is according to Equation (2.54) given by $S(\omega_L/2\pi) \times (\rho P_{\text{laser}})^2 = 2PT_2 \times (\rho P_{\text{laser}})^2$ where the Faraday rotation is converted into units of the detector output by multiplication with the detector gain ρ and the probe laser power P_{laser} . Note that the spin noise power is contrary to the shot noise power quadratic in laser power and a higher laser power accordingly increases the signal strength η which is quantified by the ratio between peak spin noise power density and shot noise power level:

$$\eta = PT_2 P_{\text{laser}}/\hbar\omega_{\text{laser}}. \quad (3.6)$$

Table 3.1 gives a survey on recent semiconductor spin noise experiments regarding the orders of magnitude of the integrated spin noise power P , the spin dephasing time T_2 , the peak spin noise power density $S(\omega_L/2\pi)$, the probe laser power at the detector P_{laser} , and the signal strength η and also shows estimated values for prospective spin noise measurements in a single quantum dot and in bulk GaAs at room temperature. The last column of Table 3.1 reveals that the photon shot noise level is large compared to the amount of spin noise, especially for systems with high spin dephasing rates. This circumstance necessitates the efficient data averaging via real-time FFT spectrum analysis that is introduced in Section 3.2.1. Due to the fast data acquisition, typical integration times in this work of 10 to 20 minutes yield a signal-to-noise ratio—defined as ratio of the height of the spin noise power peak to the variance of the shot noise level—of 20 to 30 dB.

3.2.2. Subtraction of background noise

Laser shot noise is white noise and adds in theory as a constant noise floor to the spin noise as expounded in Section 3.2.1. However, due to the finite detector bandwidth, the shot noise power density is frequency dependent [see Equation (3.5)] and, furthermore, the frequency response of the detector and an optional pre-amplifier can generally not be viewed as constant within the relevant frequency intervals. Sub-

Table 3.1.: (a) Magnitude of spin noise power P , spin dephasing time T_2 , peak spin noise power density $S(f_L)$, probe laser power P_{laser} , and ratio of $S(f_L)$ to the background shot noise level, i.e., the signal strength η , for different semiconductor systems at cryogenic temperatures. All quantities are detector independent and mostly apply to the weakly perturbing detection regime, i.e., strong detuning and large probe area. Electrical noise is neglected for calculating η . (b) Estimated values for prospective measurements. In the case of the single spin, additional electrical noise equivalent to 0.04 mW probe laser power is assumed.

Investigated system	Ref.	P [μrad^2]	T_2 [ns]	$S(f_L)$ [$\mu\text{rad}^2/\text{Hz}$]	P_{laser} [mW]	η
(a)						
n -doped Bulk GaAs ($1.8 \times 10^{16} \text{cm}^{-3}$, $l \approx 340 \mu\text{m}$)	[100]	10	100	1	1	10^{-2}
n -doped Bulk GaAs ($2.7 \times 10^{15} \text{cm}^{-3}$, $l \approx 500 \mu\text{m}$)	[100]	100	10	1	1	10^{-2}
InGaAs quantum dots	[125]	1000	1	1	1	10^{-2}
n -doped Bulk GaAs ($8.8 \times 10^{16} \text{cm}^{-3}$, $l \approx 370 \mu\text{m}$)	[100]	10	10	0.1	1	10^{-3}
Modulation-doped multiple quantum well	[126]	10	10	0.1	1	10^{-3}
n -doped Bulk GaAs (10^{14}cm^{-3} , $l \approx 2 \mu\text{m}$)	[111]	10	1	0.01	1	10^{-4}
(b)						
Bulk GaAs at room temperature	[127]	10	0.1	0.001	1	10^{-5}
Single electron spin in optical cavity	[128]	100	10	1	0.01	10^{-5}

3. Experimental Methods

traction of the background noise floor and subsequent correction for the frequency dependent amplification are therefore necessary to avoid distortion of the spin noise spectra. To this end, a reference noise spectrum that does not contain spin noise has to be acquired. This can be achieved by shifting the spin noise peak in frequency by variation of the applied magnetic field as carried out for measurements presented in Sections 4.2 and 4.3. The negative spin noise peak in some spectra that are shown in this work results from this procedure (see, e.g., Figures 3.5 and 3.10).

Due to the anisotropic spin dynamics in the (110)-oriented quantum well, the spin noise peak is centered at zero frequency in the available field range (Section 4.1.2). Accordingly, an alternative approach to subtract the background noise is pursued. To this end, a reference noise spectrum is acquired by switching the optical bridge setup from detection of circular birefringence, i.e., Faraday rotation, to linear birefringence and thereby suppressing the spin noise signal contained in the probe light, while keeping the photon shot noise background: The polarization state of the probe laser light is changed by means of a variable retarder from linearly polarized light to circularly polarized light before it is transmitted through the sample. The circularly polarized light does not acquire a Faraday rotation and is split in equal parts into the two orthogonal linear polarization states via the polarizing beam splitter cube in front of the detector. The variable retardation is implemented in this work by a motorized Soleil-Babinet compensator. Alternatively, a liquid crystal retarder could be utilized, which may appear more convenient because of the higher switching speed between the two polarization states. Switching the liquid crystal retarder, however, also would introduce a slight change of the light transmission due to a change in the absolute refractive index of the waveplate that would have to be accounted for in the experiment. Switching the polarization state of the probe light in front of the sample can bear some disadvantages if the sample exhibits linear dichroism, e.g., due to strain. In this work, also the collimation lens that is inserted in the cryostat may introduce linear dichroism.⁴ Hence, best results are achieved for the

⁴A method to cancel out the spin noise signal by retardation of the probe light behind the sample is described in Reference 17.

spin noise measurements in the (110)-oriented quantum well structure (Section 4.1) by utilizing a double difference scheme where both the light polarization and the magnetic field are changed.

3.3. Extension of the experimental bandwidth

The spin noise spectroscopy setup introduced in Section 3.1 can only detect spin dynamics at frequencies that fall into the experimental detection bandwidth which is limited by the speed of the balanced photoreceiver as well as by the sampling rate of the digitizer. Accordingly, spin noise spectroscopy before this work has been limited to frequencies below 1 GHz [125]. This technical limitation poses a drawback of spin noise spectroscopy compared to conventional experimental techniques to investigate spin dynamics which allow a time resolution that corresponds to a bandwidth of the order of 1 THz. Application of spin noise spectroscopy to various semiconductor systems like, e.g., n -doped bulk GaAs at room temperature (see Table 3.1) demands an extension of the bandwidth. Here, the technical limitations resulting from the performance of the photodetector and the spectrum analyzer are investigated in detail and possible implementations to resolve fast spin dynamics via spin noise spectroscopy are reviewed. In Section 3.3.1, electrical frequency mixing is applied for down-sampling the spin noise signal into the bandwidth of the spectrum analyzer, which can be utilized if the bandwidth of the balanced receiver exceeds the bandwidth of the spectrum analyzer. It is however shown in Section 3.3.2 by means of simulated spin noise experiments that also ultrafast low-bit digitizers allow spin noise spectroscopy without any significant loss of sensitivity and, hence, the speed of the balanced photoreceiver poses the more fundamental bottleneck to spin noise spectroscopy. On this footing, a spin noise setup is suggested where the classical laser noise is no longer suppressed by balanced detection but by means of interferometry. Finally, in Section 3.3.3, a new experimental method is presented that overcomes the limitation of spin noise spectroscopy to low frequencies by application of pulsed probe light.

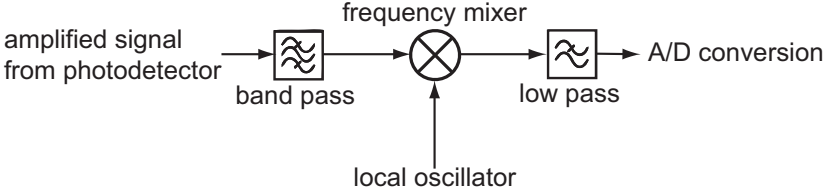


Figure 3.4.: Block diagram for electrical frequency mixing of the spin noise signal.

3.3.1. Electrical down-conversion of the noise signal

Electrical frequency mixing is an important concept in radio frequency electronics and is applied for up- or down-conversion of electric signals. For example, in parabolic antennas for satellite reception usually frequency mixing is deployed to convert the satellite signal that is modulated at frequencies around 11 GHz down to frequencies that allow transmission via standard coaxial cables.

Frequency mixing is described as multiplication of the input signal with the reference signal of a local oscillator which is given by a sine waveform $\propto \sin \omega_{\text{LO}} t$. If the input signal is as well a sinusoidal waveform, the frequency mixing results in

$$\sin(\omega_{\text{LO}} t) \times \sin(\omega_{\text{input}} t) = \frac{1}{2} [\cos(\omega_{\text{input}} - \omega_{\text{LO}}) t - \cos(\omega_{\text{input}} + \omega_{\text{LO}}) t], \quad (3.7)$$

i.e., the output of the mixer consists of the signal down(up)-converted to the difference (sum) of the two frequencies. In the experimental setup depicted in Figure 3.4, electrical frequency mixing is employed for spin noise spectroscopy to down-convert the electrical signal from the balanced receiver. This scheme may be useful if the available FFT spectrum analyzer does not fully exploit the bandwidth of the balanced receiver. To this end, the amplified electrical signal from the balanced photoreceiver is sent through a band pass filter, which filters the frequency region around the electron Larmor frequency, and gets mixed with the output of a signal generator. The output of the frequency mixer is sent through a low pass filter to avoid undersampling and is

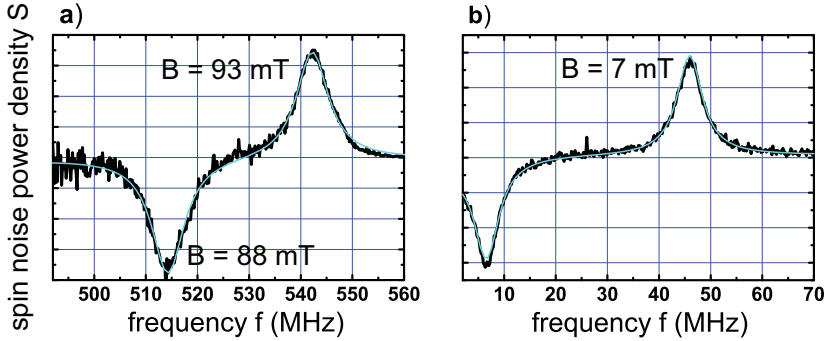


Figure 3.5.: (a) Spin noise spectrum acquired by electrical frequency mixing (see Figure 3.4); the balanced receiver has a 3 dB-bandwidth of 650 MHz while the bandwidth of the digitizer amounts to 80 MHz (b) Reference spectrum acquired with the conventional setup at lower magnetic fields; the integration time is nine times shorter than in (a).

digitized and seamlessly Fourier transformed.

Figure 3.5 (a) depicts a spin noise spectrum which is acquired by this technique. The utilized balanced receiver is the *New Focus 1607-AC-FS* with a bandwidth of 650 MHz; the voltage output is amplified by 70 dB. The local oscillator is set to $\omega_{LO} = 490$ MHz, which is added to the x -axis in Figure 3.5 (a), at an output power of 23 dBm. The utilized sample is an n -doped bulk GaAs sample (sample A, see Section 3.4.1). The two spin noise peaks correspond to 88 and 93 mT. For comparison, a reference spectrum [Figure 3.5 (b)] at low magnetic fields is acquired by the conventional setup of Figure 3.1. The total integration time for this reference spectrum is about 9 times shorter which roughly corresponds to the specified conversion loss of the frequency mixer (*Mini-Circuits ZFY-11*) of around 7.4 dB.

Accordingly, this experimental extension of the conventional setup has a reduced sensitivity due to inevitable conversion losses of the non-linear frequency mixing process that introduces additional noise. Furthermore, spin noise at Larmor frequencies larger than the bandwidth of the photodetector is still not detectable via this experimental modi-

fication. It is shown in the next section that fast low-bit digitizers can be utilized for spin noise spectroscopy without a significant decrease of the experimental sensitivity and, hence, the practical relevance of electrical frequency mixing in spin noise measurements seems to be low. Application might be useful in the case of very narrow spin noise peaks at high frequencies in order to avoid a high number of FFT points and achieve fast data processing if the sufficient computational power is not at hand.

3.3.2. Limitations of FFT spectrum analysis

In this Section, it is investigated to which extent the FFT spectrum analysis limits the experimental bandwidth of spin noise spectroscopy. FFT spectrum analyzers usually have a lower bandwidth than spectrum analyzers with a sweeping reference oscillator but allow much more efficient averaging that is demanded for spin noise spectroscopy in semiconductors (see Section 3.1 and Reference 17). In this work, a digitizer with a high resolution of $R = 16$ bit and a moderate sampling rate of $f_S = 180$ MS/s is used. Crooker *et al.* recently employed a GHz digitizer⁵ ($f_S = 2$ GS/s) to measure spin dephasing rates of a few 100 MHz [125], however, at the expense of a lower effective bit depth around $R = 6$ bit. Ultrafast digitizers with a corresponding sampling rate of up to 26 GHz are commercially available but show an effective bit depth as low as $R = 4$ bit at the maximum frequency.⁶

Figure 3.6 (a) depicts the input-output characteristics of a symmetric midrise digitizer that is usually utilized for analog-to-digital conversion of an AC signal x . The digital output y has a quantization error $q = x - y$ which results from overload (for $|x| > |x_{\max}|$, throughout this section x_{\max} is set to 0.5 V.) and from the granularity. As long as q can be viewed as distributed independently of x , the granularity results in a standard deviation of q given by Bennett's formula [122]:

$$\sigma_{q, \text{gran}} = \frac{2^{-R}}{\sqrt{12}} \text{ V}. \quad (3.8)$$

⁵Agilent U1080A Acqiris.

⁶E.g., Guzik WDM 5000.

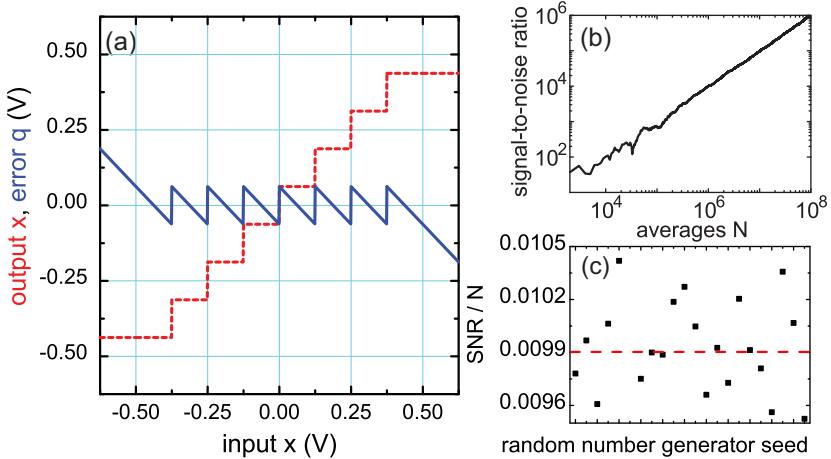


Figure 3.6.: (a) Input-output characteristics of a symmetric midrise digitizer ($R = 3$ bit). (b) Signal-to-noise ratio (SNR) of an exemplary simulated spin noise measurement with N averages. (c) SNR/ N for different random number sets; all other data in this section is acquired by means of the same set of random numbers.

In the following, spin noise measurements are simulated in which the bit depth of the digitizer, the ratio between spin noise power and optical shot noise level,⁷ and the voltage load at the digitizer input is systematically varied in order to study the influence of the analog-to-digital conversion to the experimental sensitivity of spin noise spectroscopy. The input consists of $N \times 1024$ samples. The spin noise is represented by sine waveforms with amplitude α [V] and a frequency $f_L = f_S/8$ that are added to white Gaussian background noise with zero mean and the standard deviation $\sigma_{SN} = \sqrt{B \times S_{SN}}$ [V] [see Equation (3.4)].⁸ The digital data is produced by simulating an R -bit digitizer corresponding to Figure 3.6 (a) and blocks of 1024 points are Fourier transformed

⁷ According to Section 3.2.1, other sources of detector noise can be largely neglected.

⁸ It is carefully assured that the output of the used pseudo random number generator shows no correlations that reduce the efficiency of the averaging process. The periodicity of the employed algorithm exceeds 10^{57} samples.

3. Experimental Methods

via the FFT algorithm. The resulting power spectra are averaged and the resulting noise spectrum $S'(f)$ [V^2/Hz] is obtained. The spin noise signal strength is measured by the signal-to-noise ratio (SNR) which is extracted from the simulations as $\text{SNR} = [S'(f_L) - \mu_{S'}] / \sigma_{S'}$, where $\mu_{S'}$ and $\sigma_{S'}$ denote the mean and standard deviation of $S'(f)$ with $0 < f \leq B$, $f \neq f_L$, respectively. All spin noise power is detected in a single frequency bin f_L and the magnitude of the spin noise peak is given by $S(f_L) = \alpha^2/2 \times 512/B$ on top of the shot noise floor of $S_{\text{SN}} = \sigma_{\text{SN}}^2/B$. All simulation data that is shown in this section is acquired with fixed relative signal strength $\eta = S(f_L)/S_{\text{SN}} = 256 \times \alpha^2/\sigma_{\text{SN}}^2 = 0.01$ since the following conclusions are independent of η for $\eta \ll 1$. Keeping η fixed while varying σ_{SN} corresponds to simultaneous amplification of spin noise and background noise by a voltage amplifier in the experiment.

Figure 3.6 (b) exemplarily shows the signal-to-noise ratio of the simulated spin noise measurements as a function of the averages N for a certain set of simulation parameters. The signal-to-noise ratio increases linearly with N and, hence, the slope of such a curve, SNR/N , is identified as a good measure for the detection sensitivity. In Figure 3.6 (c), SNR/N is plotted for several simulations with the same parameter set but with a different seed for the pseudo random number generator. The theoretically expected mean value of 0.01, which is derived below, for the corresponding parameter set is within the error interval around the mean of $\mu_{\text{SNR}/N} = 0.0099(3)$. Hence, in order to cope with the long computing times, statistic averaging of the simulation results is waived in the following and, instead, all simulation runs are carried out with the same set of random numbers to ensure comparability between different parameters.

Figure 3.7 (a) shows SNR/N as a function of the bit depth R for 10^8 averages, $\eta = 256 \times \alpha^2/\sigma_{\text{SN}}^2 = 0.01$, and different σ_{SN} . At optimal input load⁹ at $\sigma_{\text{SN}} = 0.1 \dots 0.2 \text{ V}$, a decrease of the detection sensitivity is found for $R \leq 3$ bit. Lower input voltages effectively reduce the bit depth and the granular quantization error becomes significant at a correspondingly higher bit depth. Given Equation (3.8), the quite weak influence of the bit depth may at first sight seem surprising. The background noise, however, can be viewed as additive dither to the signal

⁹Since $\alpha \ll \sigma_{\text{SN}}$, the input load is basically given by σ_{SN} .

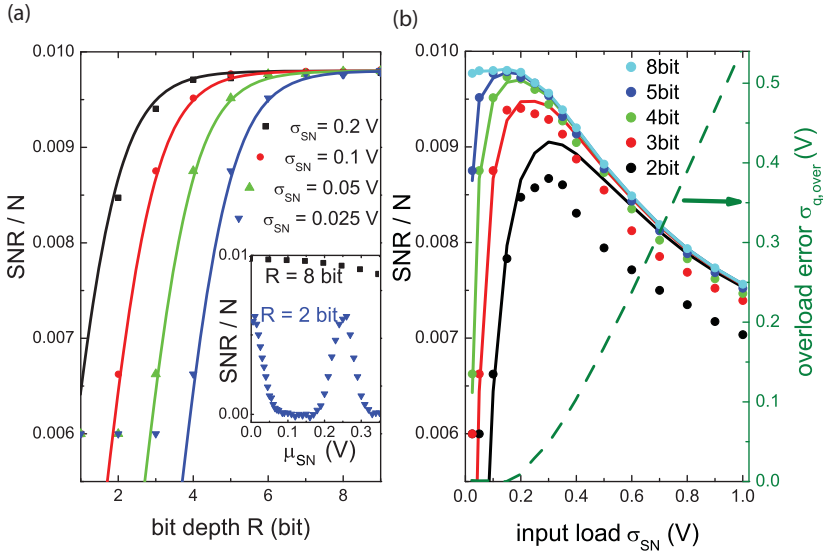


Figure 3.7.: (a) SNR/N ($N = 10^8$) as a function of the bit depth for different voltage loads. The ratio of spin noise to shot noise is set to $\eta = 256 \times \alpha^2 / \sigma_{SN}^2 = 0.01$; the solid lines are calculated by Equations (3.8) and (3.9) and corrected for the statistic deviation from 0.01. The inset shows SNR/N as a function of a superimposed DC signal μ_{SN} revealing the effective 1-bit quantization at low input load. (b) SNR/N ($N = 10^8$, $\eta = 256 \times \alpha^2 / \sigma_{SN}^2 = 0.01$) as a function of input load for different bit depths. The broken line gives the overload error for 8 bit. The solid lines are calculated with these values for $\sigma_{q,over}$ according to Equation (3.9).

that helps to detect spin noise with an amplitude much smaller than the size of the least significant bit 2^{-R} V. The effect of such additive dither on quantization has been subject of several investigations in information theory [129, 130, 131, 132, 133, 134, 135, 136, 137]. Additive dither in connection with data averaging is discussed in References 130, 133, 135, 136, and 137. Overload errors are, however, disregarded in these studies. In Reference 137, the optimal amount of dither is calcu-

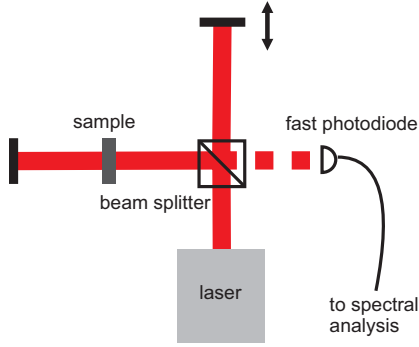


Figure 3.8.: Interferometric spin noise setup for suppression of classical noise without balanced detection.

lated to be much smaller than the white noise in semiconductor spin noise spectroscopy and, hence, while dither can be purposely added to reduce quantization errors, optical shot noise has still to be viewed as an obstacle to spin noise spectroscopy.

The standard deviation of the spin noise spectrum S is in total composed of contributions from the optical shot noise and the granular as well as the overload quantization noise:

$$\sigma_S = \sqrt{\frac{1}{B} \sqrt{\sigma_{\text{SN}}^2 + \sigma_{q, \text{gran}}^2 + \sigma_{q, \text{over}}^2} \left[\frac{\text{V}}{\sqrt{\text{Hz}}} \right]}. \quad (3.9)$$

Accordingly, the signal-to-noise ratio, extracted from the simulations as described above, reads $\text{SNR} = \alpha^2 / 2\sigma_{\text{SN}}^2 \times N$. First, it is pointed out that the linear increase of signal-to-noise ratio with N is found in the simulations for all tested parameter sets. Deviation from this linear behavior as reported in Reference 137 is not expected due to the larger amount of dither present in the simulations. Additionally, the proportionality between the signal-to-noise ratio and α^2 in the simulations over four orders of magnitude is tested. Taking into account the stochastic fluctuations of the simulated data [see Figure 3.6 (c)], SNR/N in Figure 3.7 (a) agrees well at high bit depths with the theoretically expected value of $\eta = 256 \times \alpha^2 / \sigma_{\text{SN}}^2 = 10^{-2}$. The granular quantization

error at lower bit depths is well modeled by Equation (3.8) [solid lines in Figure 3.7 (a)]. However, a significantly smaller quantization error in the simulations than in Bennett’s formula is found at $R = 1$ bit or at effective 1-bit quantization in the case of low input load. This observation is not surprising since the assumptions for Equation (3.8) obviously collapse for 1-bit quantization (see, e.g., Reference 123). Note that low input load at low bit rates resulting in effective 1-bit quantization, which theoretically shows a decent detection sensitivity, is not of experimental relevance since even the smallest DC offset μ_{SN} yields a drastic drop of the signal-to-noise ratio as it is visualized in the inset of Figure 3.7 (a). Input overload, however, which occurs above $\sigma_{\text{SN}} = 0.2\dots 0.3$ V equally destroys the efficiency of the spin noise detection even at high bit depth. Figure 3.7 (b) depicts SNR/N as a function of σ_{SN} for different R . The overload error for 8 bit (broken line) is extracted from the simulation results in conjunction with Equations (3.8) and (3.9) and is in turn utilized for calculating SNR/N for the different bit depths (solid lines), revealing that the overload error slightly depends on R . The optimal voltage load, which is found to be independent of spin noise power, varies from $\sigma_{\text{SN}} \approx 0.1$ V (8 bit) to $\sigma_{\text{SN}} \approx 0.3$ V (2 bit). Interestingly, these values coincide with the literature values for optimal load in the case of a normally distributed signal in the absence of dither [119, 138].

To conclude, the simulated spin noise measurements allow determination of the optimal input load at the digitizer for efficient data averaging. Furthermore, the simulations show that, at well chosen input load, even low-bit analog-to-digital conversion allows spin noise spectroscopy with a reasonable sensitivity. Hence, commercially available ultrafast digitizers with a bandwidth of up to 13 GHz are perfectly suitable for semiconductor spin noise spectroscopy so that the bandwidth of the basic spin noise spectroscopy setup in Figure 3.1 is from a technical point of view rather limited by the balanced receiver. However, fast InGaAs based balanced photoreceivers¹⁰ with a bandwidth of up to 20 GHz can be utilized instead of the detectors based on silicon photodiodes used in this work. Alternatively, suppression of classical laser noise in the spin noise measurements can also be achieved by an interferometric setup as depicted in Figure 3.8; here the interferometer arms are adjusted so

¹⁰E.g., *Discovery Semiconductors DSC710/720*.

that all light destructively interferes at the photodiode in the absence of spin noise. This setup would enable detection of spin noise by means of a single ultrafast photodiode.

3.3.3. Ultrafast spin noise spectroscopy

Contrary to the two previous sections, where different ways are discussed to mitigate the technical limitations of spin noise spectroscopy, this section introduces a new experimental technique that completely disposes of these bottlenecks. The basic idea is to replace the continuous-wave laser in Figure 3.1 with an ultrafast pulsed laser light source. Thereby, the spin-spin correlation in Equation (2.53) is only probed when an ultrashort laser pulse traverses the sample and the relevant correlator additionally contains the probing pulse train:

$$\langle s_z(0)s_z(t) \rangle \rightarrow \langle s_z(0)s_z(t) \rangle \times \sum_n \delta(t - n/f_{\text{rep}}), \quad (3.10)$$

where f_{rep} is the repetition rate of the laser source. Thus, the spin noise spectrum, which is given by a peak $S(f)$ around the Larmor frequency $f_L = \omega_L/2\pi$ in conventional spin noise spectroscopy, evolves into a sum of peaks all shifted by the repetition rate of the laser:

$$S(f) \rightarrow \sum_{\pm m} S(f - mf_{\text{rep}}). \quad (3.11)$$

Accordingly, spin noise at frequencies much higher than the bandwidth of the detector appears to slow down due to this stroboscopic sampling and can still be detected. Ultrafast spin noise spectroscopy is limited to dynamics on timescales that are long with respect to the pulse length. Thus, ps light pulses allow investigation of spin dynamics up to hundreds of GHz and sub ps pulses would enable access to the THz regime. It is important to note that this ultrafast sampling does not *per se* introduce any further noise and, correspondingly, does not show a reduced sensitivity compared to conventional spin noise spectroscopy. The maximal widths of the spin noise curves that can be resolved by this technique are limited by half the laser repetition rate as well as the

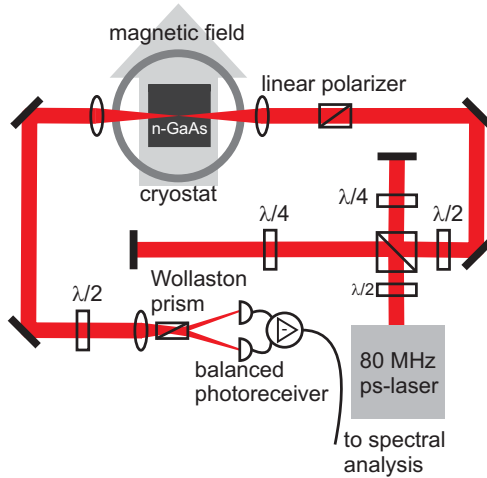


Figure 3.9.: Experimental setup for ultrafast semiconductor spin noise spectroscopy; the repetition rate of the ps laser is doubled by the Michelson interferometer-like setup to use the full bandwidth of the balanced receiver of 80 MHz.

bandwidth of the detector.¹¹

The experimental setup that is used in this work to implement ultrafast spin noise spectroscopy is depicted in Figure 3.9. An actively mode-locked titanium-sapphire laser ($f'_{\text{rep}} \approx 80$ MHz, pulse length around 3 ps) is used as light source. To exploit the full bandwidth of the utilized digitizer of 90 MHz, the repetition rate of this system is doubled by a Mach-Zehnder interferometer-like setup where one arm is $c_0/4f'_{\text{rep}} \approx 94$ cm longer than the other. The light power in the two arms is carefully adjusted by means of polarization optics and the per-

¹¹ Assuming that the spin dynamics at the Larmor frequency f_L are sampled via ultrafast spin noise spectroscopy and the replica of the spin noise peak at the lowest frequency is centered at $f_L - n f_{\text{rep}} = \Delta f$, $\Delta f < f_{\text{rep}}/2$ and the nearest neighboring spin noise peak is at $(n+1)f_{\text{rep}} - f_L$. Hence, the distance between the two spin noise peaks amounts to $2(f_{\text{rep}} - \Delta f) < f_{\text{rep}}$ which should be larger than two times the full width at half maximum of the spin noise curve w_{FWHM} to accurately resolve the spin dephasing rate so that $w_{\text{FWHM}} < f_{\text{rep}}/2$.

3. Experimental Methods

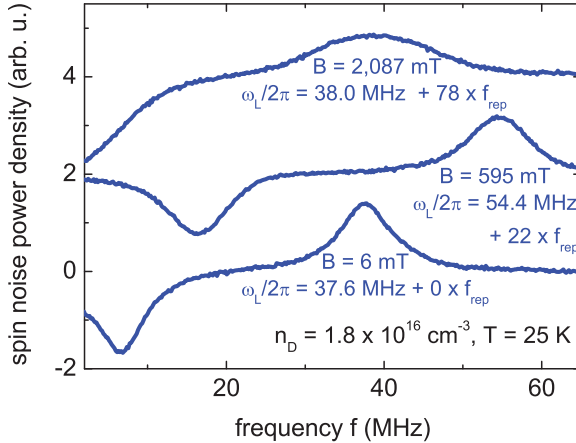


Figure 3.10.: Ultrafast spin noise spectroscopy in *n*-doped bulk GaAs (sample *A*, see Section 3.4.1); the spin dephasing shows an inhomogeneous broadening that results in a crossover from a Lorentzian to a Gaussian line shape (see Section 4.2).

fect alignment of the arm length is checked in the time domain by a streak camera system and in the frequency domain by a fast photodiode and a spectrum analyzer. This photodiode is later used to record the exact repetition rate of the system for determining the underlying Larmor frequency of the detected spin dynamics. The utilized balanced receiver has a bandwidth of 80 MHz (*New Focus 1807-FS*).

Figure 4.2 depicts three spectra that are acquired via ultrafast spin noise spectroscopy in sample *A* (see Section 3.4.1) at 25 K. Inhomogeneous spin dephasing, which is discussed in detail in Section 4.2, limits the range of applied fields to $B < 3 \text{ T}$ which corresponds to Larmor frequencies of around 16 GHz that are 200 times larger than the bandwidth of the balanced receiver.

The spin dephasing rates that can be resolved by this technique are still limited by the detection bandwidth. However, by varying the time delay between two subsequent probe pulses, the spin-spin correlation function $\langle s_z(0)s_z(t) \rangle$ is directly probed and no high-bandwidth spectral

analysis is needed anymore [139]. In this experimental modification, spin dephasing rates and the Larmor frequency would be only limited by the inverse pulse length.

3.4. Investigated samples

In this work, three samples are investigated, two n -doped bulk GaAs samples and a (110)-oriented multiple quantum well structure. All of these samples were characterized regarding their absorption and photoluminescence spectra by Römer (see Reference 118).

3.4.1. Bulk samples

The two bulk samples are commercial wafers grown by the Czochralski method (see, e.g., Reference 140). Both of these samples have antireflection coated surfaces to increase the light transmission for the spin noise experiments. The coating is given by a $\lambda/4$ -layer of amorphous silicon nitride, which was applied by the IFS Hameln.

Sample A. The first sample, denoted throughout this work as sample A, is $341 \mu\text{m}$ thick and has a silicon doping concentration of $n_{\text{D}}^{\text{A}} = 1.8 \times 10^{16} \text{ cm}^{-3}$. The sample is at the metal-to-insulator transition: $0.25 < n_{\text{D}}^{\text{A}^{1/3}} a_{\text{B}}^* \approx 0.26 < 0.33$ (see Section 2.2.2). Electrical measurements reveal hopping conductivity and extrapolation to zero temperature indicates vanishing conductivity [118]. Furthermore, an anomalous temperature behavior of the Hall voltage is found, also proving that sample A is not in the metallic phase at low temperatures [141]. At finite temperatures, also possible ionization of donors has to be considered. The donor ionization in sample A is roughly estimated by Blakemore's formula [142] to be smaller than 15% in the temperature range relevant for this work [100].¹² All spin noise measurements on this sample except the measurements shown in Section 4.3 are carried out at a laser wavelength of $\lambda = 850 \text{ nm}$, which is well within the transparency region of the sample [118].

¹²Due to the broadening of the donor binding energy in sample A, Blakemore's formula does only yield approximative results.

3. Experimental Methods

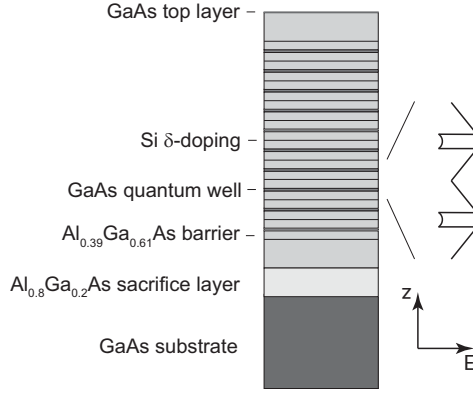


Figure 3.11.: Schematic of the investigated (110)-oriented multiple quantum well structure. At the right, also the conduction band structure is qualitatively depicted.

Sample B. The second sample is $373 \mu\text{m}$ thick and has a silicon donor concentration of $n_D^B = 8.8 \times 10^{16} \text{ cm}^{-3}$. In this sample, a fully degenerate electron gas is formed ($n_D^{B1/3} a_B^* \approx 0.44 > 0.43$). The Fermi energy at zero magnetic field for sample B is calculated via Equation (2.10) assuming a perfectly parabolic dispersion to 10.8 meV (10.2 meV) at $T = 0$ ($T = 30 \text{ K}$) which corresponds to a Fermi temperature of $E_F/k_B \approx 125 \text{ K}$. Spin noise measurements on this sample are carried out at a laser wavelength of $\lambda = 855 \text{ nm}$.

3.4.2. (110)-oriented GaAs/AlGaAs multiple quantum well

The investigated multiple quantum well structure is grown by molecular beam epitaxy (see, e.g., Reference 140) on a (110)-oriented GaAs substrate. The sample growth as well as transport measurements were carried out in the former group of Professor Wegscheider at the University of Regensburg. The sample consists of ten identical, symmetrically grown, nominally 16.8 nm thick GaAs quantum wells that are separated by 80 nm Al_{0.39}Ga_{0.61}As barriers (see Figure 3.11). The quantum wells

are symmetrically modulation-doped by silicon δ -layers in the middle of the barriers. Transport measurements under illumination yield a carrier density per quantum well of $n_D = 1.8 \times 10^{11} \text{ cm}^{-2}$ at 1.5 K and a corresponding mobility of $\mu = 3.7 \times 10^5 \text{ cm}^2/\text{Vs}$. Photogalvanic experiments by Belkov *et al.* [143] showed that spin dephasing due to structure inversion asymmetry is minimal in such symmetrically doped (110)-oriented quantum wells in contrast to symmetrically grown (001)-oriented structures. A 150 nm thick $\text{Al}_{0.80}\text{Ga}_{0.2}\text{As}$ sacrifice layer is grown between the actual structure and the substrate in order to remove the sample structure from the substrate (see next paragraph). The confinement energy for electrons and holes is numerically calculated,¹³ yielding an electronic ground state energy of 13.9 meV and a heavy (light) hole ground state energy of 1.8 meV (10.7 meV) at low temperatures. The next electronic energy level is at 55.7 meV. Since the doping concentration corresponds to a Fermi level of $E_F = 6.4 \text{ eV}$, only the lowest subband in the quantum well is occupied and the second subband is out of reach regarding the temperature range in this work. White light transmission measurements identify the optical absorption edge (interband transition to the Fermi level energy) of the quantum well between 813 and 814 nm (see Reference 118).

Sample preparation. Spin noise measurements are carried out in transmission. Therefore, the substrate is removed and the multiple quantum well layer is van-der-Waals bonded to a c-cut Sapphire substrate, following a recipe by Yablonovitch *et al.* [144] (see Figure 3.12). This recipe takes advantage of the strong dependence of the etch rate of $\text{Al}_x\text{Ga}_{1-x}\text{As}$ by hydrofluoric acid on the degree of composition x [145].

Above a certain threshold between $x = 0.4$ and $x = 0.5$, the etch rate increases by more than seven orders of magnitude while etching for $x = 0.4$ is as slow as about 0.15 nm/h in concentrated (48%) hydrofluoric acid at room temperature [146]. This extreme selective etching may be related to percolation type behavior [146].

¹³The numerical calculation solves the Schrödinger equation for a particle in a square potential. In this calculation, the different effective masses for electron and holes in the quantum well and the barrier are included. The relative valence band offset is set to 0.34 [54].

3. Experimental Methods

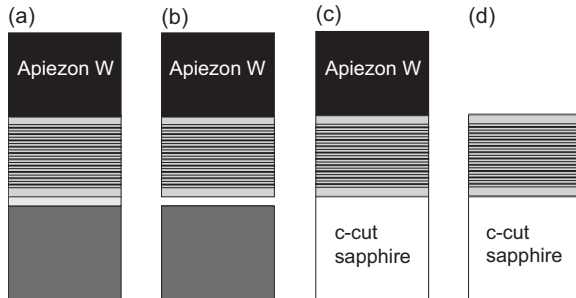


Figure 3.12.: Lift-off of the multiple quantum well structure and subsequent van-der-Waals bonding to a sapphire substrate. (a) The epilayer is covered with Apiezon W. (b) The sacrifice layer is selectively etched by hydrofluoric acid. (c) The epilayer is pressed onto a sapphire substrate. (d) The Apiezon W is removed by an organic solvent.

A drop of melted Apiezon W, a proprietary mixture of hydrocarbons, also known as black wax, is placed on the sample surface. A Teflon stamp is brought close to the sample surface so that the adhesive forces between the melted Apiezon W and the Teflon yield a full wetting of the sample surface and the sample sticks to the stamp. By the same method, a small Teflon rod is attached asymmetrically with respect to the sample geometry to the bottom side of the substrate. As the diffusion of the produced hydrogen gas from the etching zone determines the etching rate, this rod is supposed to act as a lever [147]. The sample attached to the Teflon stamp is exposed to diluted (10%) hydrofluoric acid and the sacrifice layer is selectively etched.

After rinsing the stamp with deionized water, a drop of water is deposited on a piece of (0001)-oriented sapphire substrate and the film is pressed onto it by a force of 0.8 N. Clean room tissues are used to absorb the excess water. After about 24 hours, the film is permanently bonded to the sapphire substrate. Finally, the black wax is solved in Trichloroethene (C_2HCl_3) and the sample is rinsed with water.

4.1. Spin noise spectroscopy in (110)-oriented quantum wells

Semiconductor quantum wells attract a lot of attention in the context of spintronics since they allow engineering of spin orbit fields (see Section 2.2.4). GaAs/AlGaAs based quantum wells with an (110)-oriented growth axis are especially interesting since the Dresselhaus field points along the growth axis for all \mathbf{k} -states such that electronic spins aligned with the growth axis do not dephase according to the Dyakonov-Perel mechanism [86]. The longer spin dephasing times in (110)-oriented quantum wells compared to equivalent (001)-oriented structures were experimentally demonstrated by Ohno *et al.* in 1999 [43]. Later, Döhrmann and co-workers showed that spins in the quantum well plane still undergo spin dephasing via the Dyakonov-Perel mechanism and that, subsequently, spin dephasing is anisotropic in (110)-oriented quantum wells [44]. However, in this investigation via

4. Experimental Results

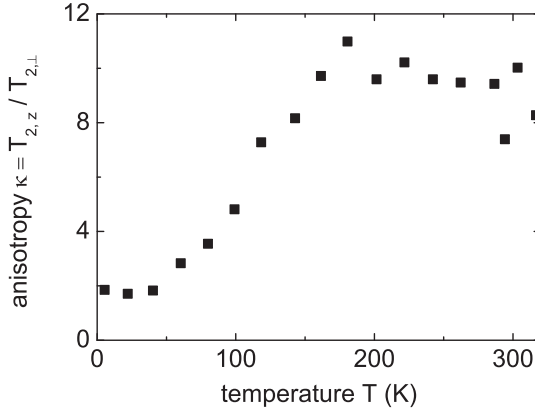


Figure 4.1.: Ratio of the spin dephasing times of spins aligned along and perpendicular to the growth direction z , $\kappa = T_{2,z}/T_{2,\perp}$, for a (110)-oriented quantum well as a function of temperature measured via polarization and time resolved photoluminescence. The isotropic Bir-Aronov-Pikus mechanism that results from the optical generation of electron-hole pairs diminishes κ at low temperatures. Data is taken from Reference 44.

time and polarization resolved photoluminescence, the anisotropy of the spin dephasing is diminished at low temperatures due to the Bir-Aronov-Pikus mechanism (see Figure 4.1). Like in all experimental probes that rely on optical spin orientation, the presence of optically created holes yields additional spin dephasing which becomes dominant because of the enhanced exchange interaction at low temperatures and the absence of other efficient mechanisms of spin dephasing. In 2007, Couto *et al.* spatially separated optically created holes from electrons by means of surface acoustic waves [148]. Nevertheless, the influence of these acoustic waves on the spin dephasing has not been established yet and the dominant mechanism of spin dephasing and the corresponding spin dephasing times in (110)-oriented GaAs quantum wells at low temperatures remained unknown. In this work, spin noise spectroscopy is applied to study spin dynamics at thermal equilibrium, i.e., in the

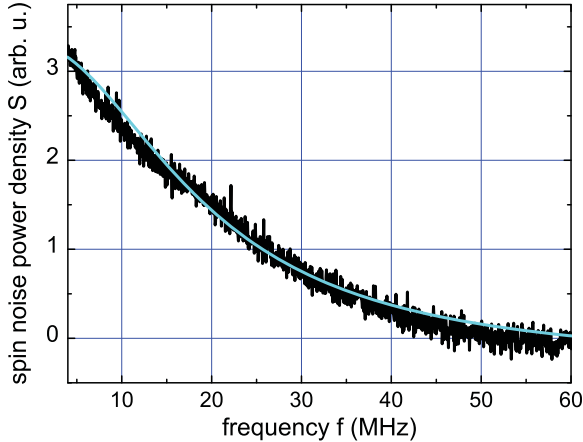


Figure 4.2.: Exemplary spin noise spectrum (acquired at 814.25 nm and 20 K); the light-colored line is a Lorentzian fitting curve centered at zero frequency.

absence of optically created holes, to explore the intrinsic mechanisms of spin dephasing in (110)-oriented GaAs quantum wells at low temperatures. This experiment constitutes the first application of spin noise spectroscopy to a semiconductor system of reduced effective dimensionality [126]. The specifics of the modulation-doped multiple quantum well structure are given in Section 3.4.2.

4.1.1. Probe wavelength dependence

Figure 4.2 shows a typical spin noise spectrum measured at a laser wavelength of about 814.25 nm (1.5226 eV), zero magnetic field, and a temperature of 20 K. All measured spin noise spectra are fitted with a Lorentz function centered at zero frequency. The area under the Lorentz curve gives the integrated spin noise power and the width determines the spin dephasing time (see Section 2.5).

Figure 4.3 shows the measured (squares) and the calculated integrated spin noise power (solid line) as a function of the probe laser

4. Experimental Results

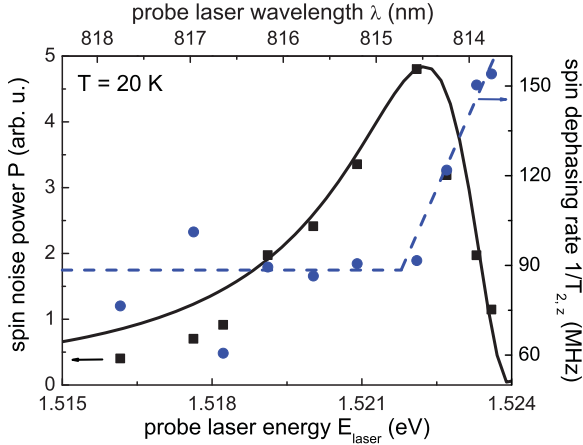


Figure 4.3.: Spin noise power P and spin dephasing rate $1/T_{2,z}$ as a function of probe laser energy (wavelength). The measured spin noise power agrees well with the theoretical modeling of spin noise presented in Sections 2.4 (further details of the calculation are given in References 118 and 126). The spin dephasing rate scales with the amount of absorbed energy due to the Bir-Aronov-Pikus mechanism; the broken line is a guide to the eye.

energy. The integrated spin noise power P is calculated by the model presented in Sections 2.3 and 2.4 (see References 118 and 126 for more details about this calculation). The spin noise power is proportional to the change of the real part of the refractive index squared with the minimum of P at the optical absorption edge (compare with Figure 2.3). The width and the position of the optical transition for the calculation are consistent with white light transmission measurements. The good agreement between modeled and measured spin noise power shows that the model presented in Sections 2.3 and 2.4 gives a realistic picture of the origin of spin noise.

Figure 4.3 also depicts the spin dephasing rate (circles) in dependence of the laser energy for a temperature of 20 K. As no magnetic field is applied, the measured spin dephasing time is purely given by

the spin dephasing of spins aligned along the growth direction, i.e., $T_{2,z}$ is measured. The spin dephasing rate $1/T_{2,z}$ increases sharply when the laser wavelength approaches the optical absorption edge. This observation is consistent with the fact that in this temperature regime traditional spin dephasing measurements based on optical excitation yield results which are completely obstructed by the Bir-Aronov-Pikus mechanism (see Figure 4.1). Measurements of this increase of $1/T_{2,z}$ by spin noise spectroscopy for wavelengths shorter than 813.7 nm are hindered by the fact that the integrated spin noise power is zero at the optical absorption edge and by the finite electrical frequency bandwidth of the detection setup. For wavelengths longer than 815 nm, optical absorption becomes negligible and the measured spin dephasing rate is in good approximation constant indicating that the electron system is very close to thermal equilibrium and that the residual spin dephasing time is determined by other spin dephasing mechanisms than the Bir-Aronov-Pikus mechanism. Further measurements (see Section 4.1.3) show that this spin dephasing rate is not yet given by the intrinsic spin dephasing but limited by time-of-flight broadening.

4.1.2. Anisotropic spin dynamics

The Dyakonov-Perel mechanism is still effective for spins perpendicular to the growth direction and, hence, the corresponding spin dephasing time $T_{2,\perp}$ is expected to be shorter than $T_{2,z}$. As a result, the equation of motion of a spin polarization differs from the isotropic Bloch equation [Equation (2.19)]. With a magnetic field applied in x -direction, the equation of motion for the spin polarization in the two other directions reads

$$\frac{d}{dt} \begin{pmatrix} m_y \\ m_z \end{pmatrix} = - \begin{pmatrix} 1/T_{2,\perp} & \mu_B g^* B/\hbar \\ -\mu_B g^* B/\hbar & 1/T_{2,z} \end{pmatrix} \cdot \begin{pmatrix} m_y \\ m_z \end{pmatrix}. \quad (4.1)$$

The exponential ansatz $[m_y, m_z] \propto \exp(\alpha t)$ yields the secular equation

$$(\alpha + 1/T_{2,\perp})(\alpha + 1/T_{2,z}) + \left(\frac{\mu_B g^* B}{\hbar} \right)^2 = 0. \quad (4.2)$$

4. Experimental Results

For $B = 0$ the differential equations decouple and the spin dephasing times are given for the two spin components by $T_{2,z}$ and $T_{2,\perp}$.¹ At low magnetic fields, the spin dephasing rate $1/T_2$ increases with magnetic field and no spin precession is observed, i.e., α in Equation (4.2) is real. The effective spin dephasing time reads for $B \leq \hbar(T_{2,\perp}^{-1} - T_{2,z}^{-1})/2g^*\mu_B$

$$\frac{1}{T_2} = \frac{T_{2,\perp}^{-1} + T_{2,z}^{-1}}{2} - \sqrt{\left(\frac{T_{2,\perp}^{-1} - T_{2,z}^{-1}}{2}\right)^2 - \left(\frac{\mu_B g^* B}{\hbar}\right)^2}. \quad (4.3)$$

At $B > \hbar(T_{2,\perp}^{-1} - T_{2,z}^{-1})/2g^*\mu_B$, the spin starts precessing, however, with a frequency smaller than the usual Larmor frequency $\omega_L = g^*\mu_B B/\hbar$ given by

$$\omega = \sqrt{\omega_L^2 - \left(\frac{T_{2,\perp}^{-1} - T_{2,z}^{-1}}{2}\right)^2}, \quad (4.4)$$

where the effective spin dephasing rate amounts to the arithmetic mean of the two spin dephasing rates.

Figure 4.4 depicts the measured $1/T_2$ (full circles) as a function of the applied magnetic field at $T = 20$ K and $\lambda = 815$ nm. The spin noise data shows the behavior expected from Equation (4.3) and is fitted by a corresponding least square fit (top solid curve).² The fit yields the anisotropy factor $\kappa = T_{2,z}/T_{2,\perp}$ which is shown as filled squares in the inset of Figure 4.4 in dependence on the probe laser wavelength. The anisotropy factor is smaller at $\lambda = 815$ nm than at longer wavelengths since the Bir-Aronov-Pikus mechanism is in contrast to the Dyakonov-Perel mechanism not explicitly dependent on the crystallographic direction and an efficient isotropic spin relaxation lowers the spin relaxation anisotropy. In agreement with the wavelength dependent data (Figure 4.3), the anisotropy factor is constant for long wavelengths since the Bir-Aronov-Pikus mechanism is inefficient at thermal equilibrium.

Also, measurements at a laser wavelength of $\lambda = 815$ nm with a

¹Note that $T_{2,\perp}$ cannot be solely detected in an optical experiment as the optical selection rules for a quantum well forbid emission or absorption of circularly polarized light with a wavevector in the quantum well plane [149].

²The effective electron g -factor $g^* = 0.29$ was acquired via time and polarization resolved photoluminescence by Stefan Oertel.

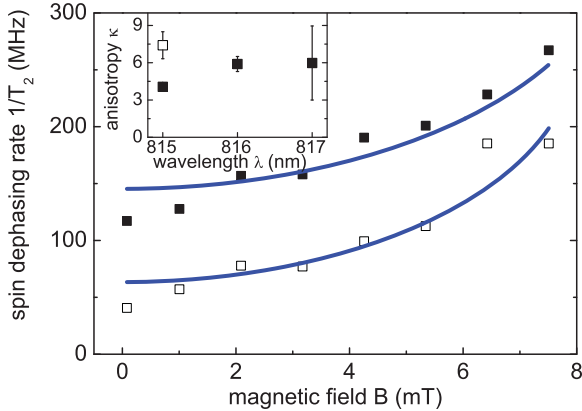


Figure 4.4.: Effective spin dephasing rate as a function of the magnetic field applied in the quantum well plane at a probe laser wavelength of 815 nm with a small (full symbols) and an enlarged laser spot (open symbols) on the sample. The curves are fits according to Equation (4.3). The inset depicts $\kappa = T_{2,z}/T_{2,\perp}$ that is extracted from the fits for different probe laser wavelengths. Spin noise measurements with an enlarged laser spot yield a higher anisotropy indicating time-of-flight broadening of the spin noise spectra (see Section 4.1.3).

strongly defocused laser spot on the sample (open circles in Figure 4.4) show a reduced spin dephasing by the Bir-Aronov-Pikus mechanism and yield an anisotropy factor $\kappa = 7.4(1.0)$ which is almost a factor of two larger than in the focused case. This anisotropy factor is of the same magnitude as κ measured in a similar sample at room temperature [44] and in an undoped GaAs (110)-oriented quantum well at low temperature where electrons and holes are spatially separated via surface acoustic waves [148]. However, in these two cases the physical origin of this anisotropy is different. In the room temperature case, the anisotropy is limited by intersubband spin relaxation [44] and, in the latter case, the anisotropy is probably dominated by the yet unclear influence of the surface acoustic waves. As argued in Section 4.1.4, the anisotropy measured in this work is in contrast given by the hitherto un-

known intrinsic low temperature spin dephasing times in (110)-oriented quantum wells.

4.1.3. Time-of-flight broadening

The strong increase of $T_{2,z}$ after defocusing cannot be solely explained by the reduction of the Bir-Aronov-Pikus mechanism since κ is only equal to about 6 for laser wavelengths of 816 and 817 nm where the Bir-Aronov-Pikus mechanism is negligible (see Figure 4.4). In fact, the strong dependence on the laser spot diameter indicates diffusion of electrons out of the laser spot which is equivalent to time-of-flight broadening. It is known from spin noise spectroscopy in atomic gases that time-of-flight broadening can have a significant influence on the observed width of the spin noise curve [150]. Figure 4.5 depicts the measured spin dephasing rate in dependence on the beamwaist w at the sample position.³ At $\lambda = 815$ nm (squares), the Bir-Aronov-Pikus mechanism cannot be completely neglected while at $\lambda = 816$ nm (circles) the Bir-Aronov-Pikus mechanism is negligible. Measurements at 816 nm with twice the probe laser power (triangles) rule out that the observations can be attributed to any excitation density dependent spin dephasing mechanism. As intrinsic spin dephasing rate, $1/T_{2,z}^{\text{intr}} = 42(3)$ MHz is determined. This value is the average dephasing rate to which the measured values converge by defocusing ($T = 20$ K and $\lambda = 815$ nm) and corresponds to a spin dephasing time of $T_{2,z}^{\text{intr}} = 24(2)$ ns which is the longest reported spin dephasing time for delocalized electrons in n -doped GaAs (110)-oriented quantum wells. Possible mechanisms of spin dephasing are discussed in the next section.

In the following, the observed time-of-flight broadening is theoretically modeled: The investigated electron ensemble is at thermal equilibrium and has accordingly vanishing total momentum. For calculation of the relevant scattering time τ_p^* , also electron-electron interaction has to be included (see Section 2.2.4). The electron-electron scattering time for a two-dimensional system in thermal equilibrium calculates to

³The beamwaist is varied by defocusing and is calculated from the beam parameters $w_0 = 3.5 \mu\text{m}$ and $z_R = 3 \mu\text{m}$ via $w(z) = w_0 \sqrt{1 + (z/z_R)^2}$; the focus position, $z = 0$, is determined for each data set by the observed time-of-flight effect, i.e., by fitting a peak shaped function to the experimental data.

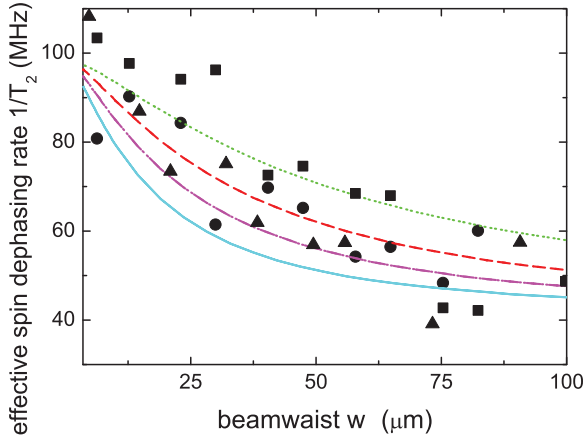


Figure 4.5: Effective spin dephasing rates $1/T_{2,z}$ ($T = 20$ K) as a function of the laser beamwaist at the sample position for a laser wavelength of 815 nm (squares), 816 nm (circles) and 816 nm with doubled laser power (triangles). The dephasing rates calculated according to the modeling given by Equation (4.8) are included for $D = 100$ cm²/s (solid line), 200 cm²/s (dash-dotted line), 400 cm²/s (dashed line) and 1000 cm²/s (dotted line).

[151, 152]⁴

$$\frac{1}{\tau_{ee}} = \frac{\pi (k_B T)^2}{2\hbar E_F} \ln \frac{E_F}{k_B T}, \quad (4.5)$$

which amounts to around 700 fs for the investigated sample system at 20 K while the mobility measurements (see Section 3.4.2) yield via the Drude relation ($\mu = e\tau_p/m_e^*$) a momentum scattering time of $\tau_p \approx 14$ ps ($\mu = 3.7 \times 10^5$ cm²/Vs). Accordingly, with the beamwaist w of the order of several microns, the electron dynamics on the relevant time scale given by w/v_F are diffusive. Thus, the sojourn probability for a classical electron at the time t which resides at the beginning of the

⁴This expression is only valid for $k_B T \ll E_F$. Here, the Fermi temperature E_F/k_B amounts 74 K and sample temperature is 20 K. At $k_B T \gg E_F$, the scattering rate increases linear with temperature.

4. Experimental Results

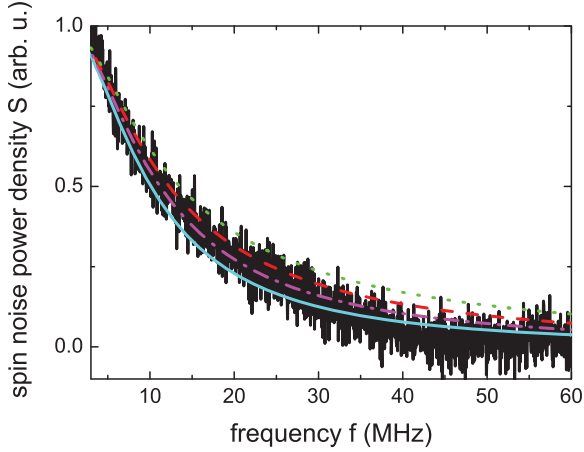


Figure 4.6.: Spin noise spectrum for $w = 23 \mu\text{m}$ at $T = 20 \text{ K}$ and $\lambda = 816 \text{ nm}$. The lines show calculated spectra according to the modeling given by Equation (4.8) for $D = 100 \text{ cm}^2/\text{s}$ (solid line), $200 \text{ cm}^2/\text{s}$ (dash-dotted line), $400 \text{ cm}^2/\text{s}$ (dashed line) and $1000 \text{ cm}^2/\text{s}$ (dotted line).

measurement $t = 0$ at the two-dimensional coordinate \mathbf{r}_0 is given by [153, 154]

$$P(\mathbf{r}, \mathbf{r}_0) = \frac{1}{4\pi D t} \exp\left[-\frac{(\mathbf{r} - \mathbf{r}_0)^2}{4D t}\right]. \quad (4.6)$$

Here, the D is the diffusion constant. The spin noise from the electron at position \mathbf{r} has to be weighted with the intensity profile of the laser beam:

$$I(\mathbf{r}) = I_0 \exp(-2r^2/w^2). \quad (4.7)$$

Overall, the spin noise spectrum is modeled by

$$S(\omega) \propto \int d\mathbf{r}_0 \left| \mathcal{F} \left\{ \int d\mathbf{r} \exp(-t/T_{2,z}^{\text{intr}}) \cdot P(\mathbf{r}, \mathbf{r}_0) \cdot I(\mathbf{r}) \right\} \right|^2, \quad (4.8)$$

where $\exp(-t/T_{2,z}^{\text{intr}})$ describes the intrinsic spin dephasing and \mathcal{F} denotes the Fourier transformation. Figure 4.6 shows different spin noise

spectra that are numerically calculated via Equation (4.8) together with an experimental spectrum for $w = 23 \mu\text{m}$. The curves are calculated for different diffusion constants. The dependence of the observed spin dephasing rate on the beamwaist w is calculated numerically via Equation (4.8) and is included in Figure 4.5 for different values of D . Best agreement between model and experiment is obtained for values of D between 100 and $1000 \text{ cm}^2/\text{s}$, the measurement accuracy however does not allow a more precise determination of D . The measured mobility of $\mu = 3.7 \times 10^5 \text{ cm}^2/\text{Vs}$ yields together with the Einstein relation $D = \frac{\mu E_F}{e} \approx 2400 \text{ cm}^2/\text{s}$ ($E_F = 6.4 \text{ meV}$) while the electron-electron scattering time corresponds to a diffusion constant of $D \approx 100 \text{ cm}^2/\text{s}$. Accordingly, the diffusion constants determined by modeling the time-of-flight broadening of the spin noise spectra are in the expected range. Hence, this experiment allows in principle investigation of the Brownian motion of electrons at thermal equilibrium.

After the first publication of these results [126], time-of-flight broadening in spin noise spectroscopy was theoretically investigated by Kos *et al.* [155], however, for the case of a cylindrical laser intensity profile. They derive that in this case the width of the spin noise curve is given by $D/w^2 + 1/T_{2,z}^{\text{intr}}$. The authors however do not give a conversion from this ideal beam profile to a physical Gaussian profile. This conversion is not expected to be linear since the measured dephasing rates in Figure 4.5 do not show a w^{-2} behavior.

4.1.4. Intrinsic spin dephasing

As expounded in the previous sections, the Dyakonov-Perel mechanism contributes to the in-plane spin dephasing with a rate of $1/T_{2,\perp}^{\text{intr}} - 1/T_{2,z}^{\text{intr}} \approx 300 \text{ MHz}$. Equations (2.32) and (2.28) with a Dresselhaus coefficient of $\gamma_D \approx 8 \dots 10 \text{ eV}\text{\AA}^3$ [156] yield a momentum scattering time consistent with $\tau_p^* \approx 700 \text{ fs}$ as calculated in the previous section.

Still, the physical origin for $T_{2,z}^{\text{intr}}$ is unknown. The Elliott-Yafet mechanism is expected to yield spin dephasing times of the order of several hundred nanoseconds [157]. The recently discovered intersubband spin relaxation [44], which is generally effective in quantum wells, cannot account for the experimental findings in a quantum well with a rather large

4. Experimental Results

subband splitting (see Section 3.4.2) compared to $k_B T$ and E_F [158]. Accordingly, Zhou and Wu calculated spin dephasing times longer than 100 ns for the investigated sample structure in a fully microscopic model including all of these spin dephasing mechanisms [159].

The Van-der-Waals bonding of the quantum well structure to the sapphire substrate introduces strain in the sample [111]. However, it has been demonstrated theoretically [160] as well as experimentally [161] that $T_{2,z}$ in a (110)-oriented grown structure is unaffected by strain.

Nevertheless, as expounded in Section 2.2.4, inevitable density fluctuations in the doping sheets yield microscopic Rashba fields that in turn result in spin dephasing. This spin dephasing by random Rashba fields was initially put forward by Sherman in 2003 [89] and it was suggested in Reference 126 that this spin dephasing mechanism may represent the final limitation for spin dephasing times in symmetric modulation-doped (110)-oriented GaAs/AlGaAs quantum wells. According to Equation (2.35), the relevant fluctuation of the doping density amounts to $1/\sqrt{\pi R_d^2 n_D} \approx 27\%$. The corresponding mean deviation of the electric field is calculated to $\sqrt{\langle \mathcal{E}_z^2 \rangle} \approx 2.5 \text{ kV/cm}$. Using $\xi \approx 8.7 \text{ \AA}^2$ from Reference 162, the corresponding spin dephasing rate $1/T_2^{\text{RR}}$ amounts to around 2.5 MHz [Equation (2.37)], which is more than one order of magnitude smaller than the observed spin dephasing rates. More detailed theoretical calculations yield different dephasing times: While the fully microscopic calculation from Reference 156 agrees well with the experimental findings of this work, the work by Glazov *et al.*, where also spin-flip collisions of electrons from different quantum wells of the multiple quantum well structure are explicitly considered [163], gives spin dephasing times similar to those calculated by Equation (2.37). The deviations between experiment and theory can however also result from unknown sample parameters like the effective Rashba coefficient.

Belkov *et al.* showed that—unlike to corresponding (001)-grown quantum wells—the symmetric growth of modulation-doped (110)-oriented quantum wells—very similar to the sample investigated in this work—results in structures with at most very small net Rashba fields [143]. Nevertheless, Karimov *et al.* [164] and Iba *et al.* [165] demonstrated that growth imperfections yield significantly shorter spin de-

phasing times and destroy the structure inversion symmetry. Hence, also Dyakonov-Perel spin dephasing due to net Rashba fields could contribute to the observed spin dephasing. In fact, the inevitable doping density fluctuations of around 27% should exceed electric fields resulting from growth imperfections. However, the correlation time for the Dyakonov-Perel mechanism is given by $\tau_p^* \approx 700$ fs at 20 K while the correlation time in the case of random Rashba fields is the passage time $\tau_d = R_d/v_F \approx 250$ fs. Correspondingly, motional narrowing should be less efficient at 20 K for the usual Dyakonov-Perel mechanism and, hence, spin dephasing by net Rashba fields cannot *a priori* be excluded.

A criterion to decide whether the observed spin dephasing is dominated by net or random Rashba fields is given by the temperature dependence of the dephasing rates [90]. The correlation time of the net Rashba fields is given by Equation (4.5) and should correspondingly obey a strong temperature dependence; the observed spin dephasing rate should in this case show a T^{-2} behavior. The correlation time for the spin dephasing by random Rashba fields, on the other hand, is the passage time through one disorder domain $\tau_d = R_D/v_F$ that should be nearly independent of temperature as long as $T < E_F/k_B = 74$ K. The experimental outcome ($\lambda = 815$ nm) is depicted in Figure 4.7. The probe laser is defocused and, hence, time-of-flight broadening can be neglected. The measured spin dephasing rate is within the measurement accuracy independent of temperature at low temperatures and increases for temperatures above 15 to 20 K. The dotted line shows the temperature behavior expected for the case of the Dyakonov-Perel mechanism. Still, the increase of the spin dephasing rates at higher temperatures is unexpected at first sight, but can be explained by the increased efficiency of the Bir-Aronov-Pikus mechanism that results from increased absorption due to broadening of the optical transition width (see Figure 4.7). Accordingly, the experimental data supports the hypothesis that spin dephasing in the investigated sample is dominated by random Rashba fields and motional narrowing due to the transit through different disorder domains.

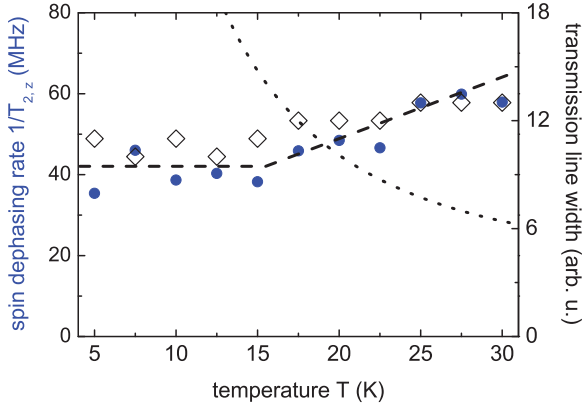


Figure 4.7.: Spin dephasing rate (circles, $\lambda = 815$ nm) and width of the optical transition (diamonds) as a function of temperature. The broken line depicts the expected temperature dependence of the spin dephasing rate in case of Dyakonov-Perel spin dephasing. The observed temperature dependent spin dephasing can be attributed to the Bir-Aronov-Pikus mechanism that gets more efficient as the width of the optical transition increases. Relative values for the width are acquired by white light transmission measurements [118].

4.2. Spin noise spectroscopy in n -type bulk GaAs in transverse magnetic fields

The advancement of spin noise spectroscopy to GHz frequencies, which is introduced in Section 3.3.3, allows precision spectroscopy of the effective g -factor as well as investigation of the spin dephasing in transverse magnetic fields. It is expounded in Section 2.2.3 that the effective Landé factor in GaAs shows a delicate energy dependence. This energy dependence necessitates extrapolation to zero excitation density in conventional experiments in order to determine reliable values for g^* [149]. In doped bulk samples below the metal-to-insulator transition, conventional optical techniques, like time-resolved photoluminescence or Faraday rotation, rely on a transfer from the spin polarization of

free electrons to the donor electron ensemble [17]. Correspondingly, these two electron species are present during a significant portion of the measurement time and the detected spin dynamics usually present an average over the two electronic states [166, 167, 168]. These circumstances complicate g -factor spectroscopy in samples at the metal-to-insulator transition and, likewise, the spin dephasing in this doping range strongly depends on the optical excitation due free carrier generation and electron heating (see Section 2.2.4). Spin noise spectroscopy leaves the sample system close to thermal equilibrium and, accordingly, circumvents these problems. In this work, the effective g -factor as a function of magnetic field and temperature (Section 4.2.2) as well as the dependence of the spin dephasing on a transverse magnetic field (Section 4.2.1) are investigated for n -type bulk GaAs at (sample A) and above (sample B) the metal-to-insulator transition. The specifics of the samples are given in Section 3.4.1. Exemplary spin noise spectra (sample A) are shown in Figure 3.10; the spin dephasing times are extracted via fitting Lorentzian curves to the spin noise spectra.⁵ The Larmor frequency is extracted from the experiment as the center frequency of the peak plus a multiple of the laser repetition rate (see Figure 3.10), which is determined by a stepwise increase of the magnetic field.

4.2.1. Spin dephasing in transverse magnetic fields

Spin dephasing in a transverse magnetic field is quantified by means of the spin quality factor [16]:⁶

$$Q = \frac{g^* \mu_B B T_2^*}{h}. \quad (4.9)$$

⁵At high magnetic fields, Gaussian curves yield better least-square fits for sample A indicating a crossover from homogeneously broadened Lorentzian peak to an inhomogeneously broadened Gaussian peak (see Section 2.2.4). In the intermediate field region, a physical correct fit function would base upon Voigt profiles which have too many free parameters for practical purposes. Nevertheless, fitting with Gaussian profiles yields comparable peak widths as fitting Lorentzian profiles.

⁶This quality factor of a spin ensemble is defined analogously to the Q -factor of all kinds of physical systems as the ratio of the resonance frequency to the bandwidth of the system.

4. Experimental Results

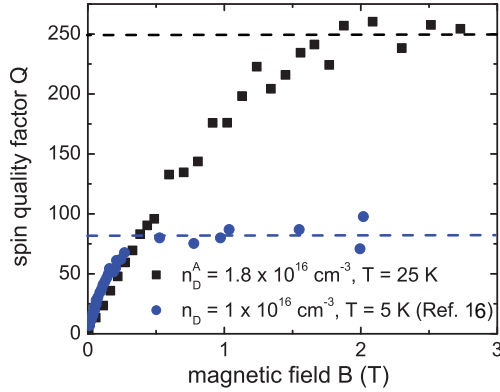


Figure 4.8.: Spin quality factor [see Equation (4.9)] for sample A at a temperature of 25 K (squares) and the Q -factor from Reference 16 at 5 K (circles); the lines are guides to the eye.

If the investigated sample shows a linear increase of the spin dephasing rate in a magnetic field, i.e., $1/T_2^*(B) = 1/T_2^*(0) + C \times B$, e.g., due to inhomogeneities of the effective g -factor according to Equation (2.39), then an initial increase of Q with the magnetic field at a slope of $g^* \mu_B T_2^*(0)/h$ and a subsequent saturation of the quality factor at $g^* \mu_B / Ch$ is expected. A superlinear increase of $1/T_2^*(B)$ would accordingly result in a Q -factor converging to zero at high fields while a sublinear increase or a decrease correspond to an ever increasing spin quality factor.

Kikkawa and Awschalom for example measured via resonant spin amplification a plateau of the spin quality factor of around 80 for a sample with a doping concentration of $n_D = 1 \times 10^{16} \text{ cm}^{-3}$ and a temperature of 5 K [16]. They attributed this maximal Q -factor to a thermal electron distribution and the energy dependence of g^* yielding an inhomogeneous broadening. Puttika and Joynt gave a different explanation for the same experimental data and suggested a spin-phonon mechanism, which effectively leads to a homogeneous broadening of the spin dephasing rate for localized electrons [167].

Sample A. Figure 4.8 shows the Q -factor of a similar sample (sample A) measured via ultrafast spin noise spectroscopy at a lattice temperature of 25 K together with the data from Reference 16. The plateau of the Q -factor measured in this work of around 250 is despite a five times higher temperature about three times larger than the value reported in Reference 16. This finding directly disproves that the spin quality factor measured by Kikkawa and Awschalom is limited by a g -factor spread resulting from a thermally broadened electron energy distribution. Such a thermally broadened g -factor spread is negligible on these timescales due to a motional narrowing type averaging in the electron energy, which additionally leads to a quadratic dependence of the broadening on the magnetic field and, hence, would not result in the formation of a Q -factor plateau [see Equation (2.38) and the paragraph “Sample B”]. The ultrafast spin noise measurements also discourage the theory of thermally activated lattice vibrations since further measurements in sample A from 6 to 30 K show a Q -factor at $B = 1$ T of similar size as at $T = 25$ K.

Correspondingly, the origin of the broadening of the spin noise peak in sample A needs a more careful assessment. According to Reference 100, the spin dephasing at zero field in sample A is dominated by the anisotropic exchange interaction or closely related mechanisms (see Section 2.2.4). The magnetic field dependence of these mechanisms is quite intricate [102] but a magnetic field at this doping density is rather expected to increase the corresponding spin dephasing times:⁷ For instance, τ_c in Equation (2.43) is expected to increase in a magnetic field due to the resulting localization [102].⁸

Thus, the observed increase of the spin dephasing rate in sample A

⁷At lower doping concentrations, where a significant portion of the donor electrons form clusters that consist of two neighboring donors, the spin dephasing rate may significantly increase in a magnetic field [169]: The donors in such a cluster exchange their spin frequently. Nevertheless, the mechanism according to Equation (2.43) is ineffective at zero magnetic field because the rotation of the spin by γ is compensated by the next spin exchange process which yields a rotation of $-\gamma$. This situation changes when the spin precesses due to an additional external field and spin dephasing rates increase. At the doping concentration of sample A, the average interdonor distance however amounts 23 nm and a formation of such donor pairs is not expected.

⁸According to Reference 102, τ_c is increased by a factor of $1/e$ at 4 T.

4. Experimental Results

cannot result from the increased efficiency of the mechanism that dominate spin dephasing at vanishing magnetic field and another mechanism has to be effective. The line shape of the spin noise spectra in sample A at high magnetic fields indicates a Gaussian broadening of the spin noise curves (see Footnote 5 on page 91) and, hence, an inhomogeneous mechanism of spin dephasing is expected. Depth-resolved spin noise measurements⁹ that were carried out by Römer (see References 118 and 171) show that the absolute value of the effective g -factor in sample A is increased at the sample surfaces. According to the energy dependence of the effective Landé factor in GaAs [Equation (2.14)], such a behavior is linked to a lowered Fermi energy in the impurity band and, correspondingly, to a diminished carrier concentration at the sample surface. This observation may be explained by Fermi level pinning at the surface and consequent electron depletion; however, such a behavior is hard to model for a doping concentration below the metal-to-insulator transition where an impurity band is formed (see References 118 and 171). This observation can only be understood if the charge carriers in sample A are at least partially localized. This localization is further proved by the temperature dependence of the spin noise power in sample A where extrapolation to vanishing temperature shows a finite amount of spin noise [171] which can only be present if the probed electron ensemble is not fully degenerate (see also Section 2.4). The lower Q -factor from Reference 16 may be explained by the slightly lower doping concentration which should result in stronger localization of the electrons but can also originate from the measurement technique itself, which does not allow for averaging of the spin dynamics over the whole sample thickness as spin noise spectroscopy and may enhance spatial inhomogeneities due to the inhomogeneous optical excitation profile.

Sample B. Figure 4.9 depicts the measured spin quality factor for the samples A and B at a temperature of 25 K. While the Q -factor in sample A levels off at about $Q = 250$, sample B exhibits no Q -

⁹Depth-resolution is a unique feature of spin noise spectroscopy [170]; conventional experimental methods that employ light above the bandgap are exclusively sensitive to the sample surface.

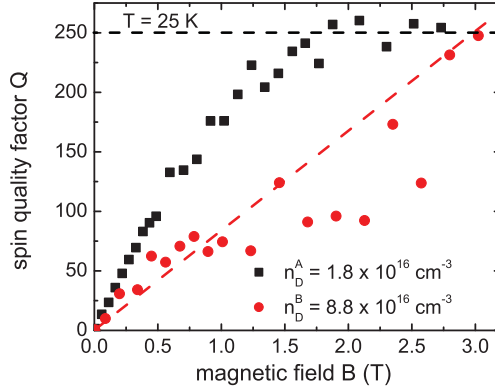


Figure 4.9.: Spin quality factor [Equation (4.9)] for samples A (squares) and B (circles) at a temperature of 25 K; the lines are guides to the eye.

factor plateau in the examined field range.¹⁰ The electrons in sample B with a doping concentration well above the metal-to-insulator transition ($n_d^B = 8.8 \times 10^{16} \text{ cm}^{-3}$) are expected to be fully delocalized. This assertion is backed up by the temperature dependence of the spin noise power P [171]: Extrapolation of P to zero temperature yields vanishing spin noise power. This behavior results from Pauli blockade [Equation (2.51)] and, correspondingly, proves full degeneracy of the donor electrons. In this doping regime, the Dyakonov-Perel mechanism dominates spin dephasing at zero magnetic field for all temperatures [100]. At a magnetic field of $B = 1$ T, the cyclotron and the Larmor frequency amount to $\omega_c \approx 2.6$ THz and $\omega_L \approx 37$ GHz, respectively, while the momentum relaxation rate due to impurity scattering time is of the order of $\tau_p \approx 1$ ps [172]. Hence, the Dyakonov-Perel spin dephasing times are rather expected to increase according to Equation (2.30) in the applied magnetic field range of up to $B = 3$ T since $\omega_c \tau_p \gtrsim 1$. Spin dephasing

¹⁰The scatter of the data for sample B above magnetic fields of 1 T results from a drastic drop of the spin noise power. This observation may originate from Landau quantization and suppression of spin noise due to Pauli blockade (see Section 4.2.2).

4. Experimental Results

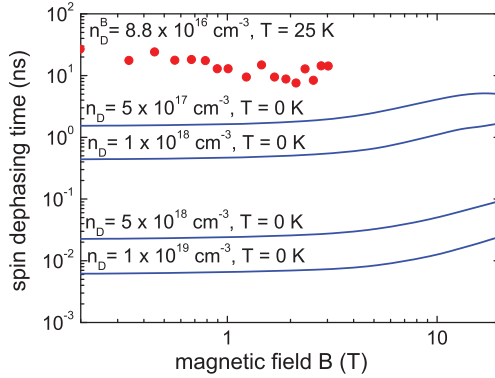


Figure 4.10.: Spin dephasing times in sample B at 25 K (circles) as a function of magnetic field. The lines are calculated low temperature spin dephasing times for higher doping concentrations taken from Reference 92.

due to a thermal g -factor spread [Equation (2.38)] is not expected to contribute to the measured rates at these moderate fields below 10 T.¹¹ Hence, a strictly monotonic increase of the quality factor in sample B is expected in agreement with the fact that no Q -factor plateau is formed in the applied field range (Figure 4.9). However, the corresponding spin dephasing times in sample B , which are depicted in Figure 4.10 together with theory curves from Reference [92] for higher doped samples, still slightly decrease with increasing magnetic field. This behavior is unexpected from theory and cannot be explained within this work.

4.2.2. Field, doping and temperature dependence of the effective Landé factor

Last, the doping, temperature, and magnetic field dependence of g^* , which is a consequence of the energy-dependent effective g -factor, is

¹¹The energy dependence of the effective Landé factor of $dg^*/dE = 6.3 \text{ eV}^{-1}$ (see Section 2.2.3) and the thermal energy of $k_B T = 2.2 \text{ meV}$ result in a g -factor spread of $\Delta g^*/g \approx 3\%$. Equation (2.38) yields with the above scattering time a negligible line broadening of 1 MHz.

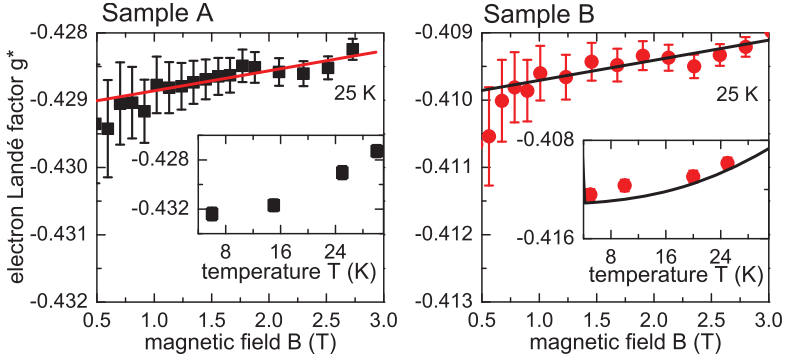


Figure 4.11.: Electron Landé g^* as a function of the magnetic field for samples A and B at $T = 25$ K and as a function of the sample temperature at a magnetic field around $B = 850$ mT. The error bars of the magnetic field dependence include the inaccuracy of the magnetic field and the repetition rate f_{rep} and the fitting errors.

studied. Before this work, similar systematic investigations were only carried out for undoped or very low n -doped bulk GaAs samples [63, 173, 174].

Figure 4.11 shows the magnetic field dependence of g^* for samples A and B at 25 K. A linear fit to the magnetic field dependence of g^* between 0.5 T and 3 T yields $g_A^* = -0.4292(2) + 3(1) \times 10^{-4} \text{T}^{-1} \times B$ for sample A and $g_B^* = -0.4100(2) + 3(1) \times 10^{-4} \text{T}^{-1} \times B$ for sample B at $T = 25$ K. The insets also show the temperature dependence of the effective Landé factor in the two samples.

Dependence on doping density. The effective Landé factor in sample B at 25 K extrapolated to zero field $g_B^* = -0.4100(2)$ is in good agreement with Equation (2.14). The deviation for the conduction band edge value corresponds to a Fermi energy of around 11 meV while the Fermi energy calculated from the doping density amounts to 10.3 meV (see Section 3.4.1). Including the thermal broadening at the Fermi edge even yields a better agreement (see next paragraph). In sample A, the donor electrons form an impurity band and are at least partially lo-

4. Experimental Results

calized. In the following, the effective g -factor of localized electrons in GaAs is estimated. Localized electronic states are formed by a sum of Bloch functions with different \mathbf{k} , i.e., the donor wavefunction given by Equation (2.7) is only an approximate solution and for calculation of g^* for localized donors a proper averaging over \mathbf{k} -space has to be carried out. Contributions from $\mathbf{k} \neq 0$ are given by the Fourier expansion of the hydrogen wavefunction, i.e., they fall off as $(k^2 + a_B^{*-2})^{-2}$ [56]. Accordingly, $\langle k^2 \rangle$ is of the order a_B^{*-2} . Using the conduction band dispersion, this corresponds to an energy similar to the effective Rydberg energy, which in turn yields

$$\begin{aligned} g_{\text{loc}}^* &\approx -0.48 + 6.3 \text{ eV}^{-1} \times E_{\text{Ry}}^* \\ &\approx -0.445. \end{aligned} \quad (4.10)$$

The experimental values for the effective g -factor of hydrogenic donors in GaAs are even higher: Colton *et al.* [175] report a value of $g_{\text{loc}}^* = -0.41$ ($T = 1...2 \text{ K}$) in agreement with Römer [118] ($g_{\text{loc}}^* = -0.40$, $T = 10 \text{ K}$). In sample A, the localization of the electrons is reduced due to overlapping donor wavefunctions and, correspondingly, a lower value is measured in this work [$g_{\text{A}}^* = -0.4292(2)$, 25 K]. A more detailed knowledge about the structure of the impurity band in sample A would allow further theoretical assessment. The measured value is in good agreement with the value reported by Schreiber *et al.* for a similar doping concentration [168].

Dependence on temperature. The effective g -factor in sample B is well understood by taking the finite Fermi energy of the system into account (see previous paragraph). A more detailed modeling also demands to include the thermal broadening at the Fermi edge. The temperature dependence of sample B is very well described by (see Figure 4.11)

$$g_{\text{B}}^*(T) = \frac{\int_0^\infty D(E)f(E,T)[1 - f(E,T)]g^*(E)dE}{\int_0^\infty D(E)f(E,T)[1 - f(E,T)]dE}, \quad (4.11)$$

where $D(E)$ is the three-dimensional density of states. Here, the conduction band edge value is set to -0.481 in agreement within the error

bars of the high precession measurements of Reference 63. Note that also the band edge value of g^* is generally a function of temperature due to the temperature dependence of the fundamental band parameters [see Equation (2.13)]. In the temperature range of this work, the change of the GaAs band parameters is however negligible [173]. For sample A, the measured temperature dependence of g^* is slightly larger than in sample B, a more detailed assessment is however not possible within this work because of the unknown impurity band structure.

Dependence on magnetic field. Stein *et al.* reported a dependence on an external magnetic field of the effective Landé factor in a doped GaAs/AlGaAs based quantum well in 1983 [176]. This behavior was later explained by Lommer and co-workers [177] via the non-parabolicity of the conduction band. The energy of conduction band electrons increases in a magnetic field according to Equation (2.17) by $\hbar\omega_c (n + \frac{1}{2})$ where n gives number of the Landau level of the electron. With the energy dependence of the effective g -factor of $dg^*/dE = 6.3 \text{ eV}^{-1}$ and the effective mass of $m_e^*/m_e = 0.067$, the change of g^* in a magnetic field B can be estimated by

$$\Delta g^* \approx 0.011 \text{ T}^{-1} \left(n + \frac{1}{2} \right) B. \quad (4.12)$$

Dobers *et al.* [178] carried out electron spin resonance in a doped quantum well and found that only the electrons from the highest Landau level contribute to the detected resonance signal in their experiment. Correspondingly, they found an increase of Δg^* with different slopes at different magnetic fields according to Equation (4.12). Oestreich *et al.* [173] and Döhrmann [149] measured the change of g^* for free electrons in undoped bulk GaAs at the conduction band edge of $dg^*/dB \approx 5 \times 10^{-3} \text{ T}^{-1}$ ($n = 1/2$). At fields above 6 T, Seck and co-workers [174] found the same increase of the effective g -factor for donor-bound electrons. In this work, both samples show a significantly more moderate slope of $3(1) \times 10^{-4} \text{ T}^{-1}$ in the field range up to 3 T at 25 K (see Figure 4.11). This slope does not significantly vary with temperature from around 5 to 30 K. Nevertheless, the physical origin of this finding is different for the two samples.

4. Experimental Results

In sample A, the magnetic field enhances the localization of the electrons which leads to an increase of $\langle k^2 \rangle$ (see paragraph “Dependence on doping density”). According to Reference 179, the extension of the donor wavefunction transverse to the magnetic field roughly decreases proportional to $B^{-1/2}$, i.e., $\langle k^2 \rangle$ increases linear in the magnetic field as observed. As $\nu < 0.5$, in the applied magnetic field range (see Section 2.2.3), the relevant energy change is significantly smaller than the Landau level splitting $\hbar\omega_c$ in accordance with the observed weak magnetic field dependence of g_A^* .

In sample B, the electrons are delocalized and are, accordingly, subject to Landau quantization. The Landau levels are however broadened due to momentum scattering. The dominant source of momentum relaxation in this doping and temperature regime is impurity scattering and the scattering time is of the order of $\tau_P \approx 1$ ps [172]. Hence, $\tau_P\omega_c \approx 1$ in the investigated field range and, correspondingly, only a weak increase of the effective g -factor in a magnetic field is observed due to impurity scattering and consequent broadening of the Landau levels. For comparison, Döhrmann [149] found an increase of $dg^*/dB \approx 6 \times 10^{-4} \text{ B}^{-1}$ at a temperature of 242 K in nominally undoped material where momentum scattering is significantly less efficient. At fields larger than ~ 4.6 T [Equation (2.18)] where only the lowest Landau level is occupied, an increase of $dg^*/dB \approx 5 \times 10^{-3} \text{ B}^{-1}$ is expected in sample B at low temperatures.

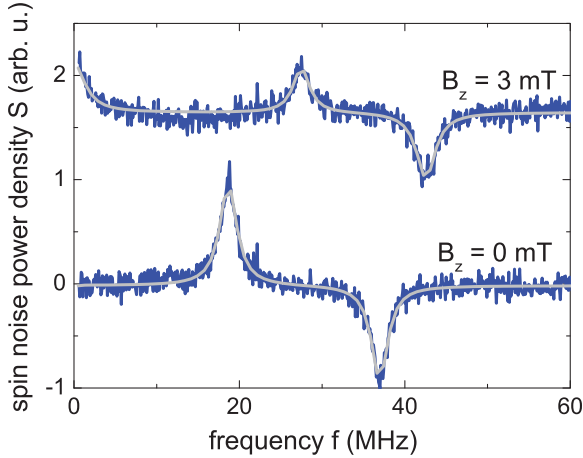


Figure 4.12.: Lower curve: spin noise spectrum acquired in Voigt configuration, i.e., $B_z = 0$; the two peaks correspond to $B_x = 3$ mT and $B_x = 6$ mT. Upper curve: spin noise spectrum acquired in an oblique magnetic field, i.e., $B_z = 3$ mT while still a transverse field of $B_x = 3$ mT and $B_x = 6$ mT is applied, respectively. Also, noise of the spin component along the magnetic field $\mathbf{B} = [B_x, 0, B_z]$ is detected around 0 MHz. The light-colored curves are fits.

4.3. Spin noise spectroscopy in oblique magnetic fields

In the spin noise measurements in the previous section, a magnetic field transverse to the wavevector of the probe light ($\mathbf{B} \perp \mathbf{k}_{\text{laser}}$) is applied to modulate the dynamics of the spin component along the probe light wavevector $\mathbf{k}_{\text{laser}}$ with the Larmor frequency. In this so-called Voigt configuration, the spin noise peak is shifted away from zero frequency and its width is determined by the spin dephasing rate $1/T_2^{(*)}$. In the Faraday configuration, i.e., in a longitudinal magnetic field, the spin noise peak is centered around zero frequency, the width is however no longer determined by T_2 , but by the spin relaxation time T_1 [see

4. Experimental Results

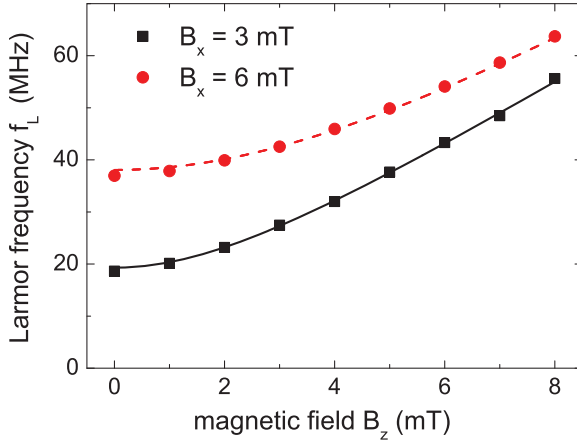


Figure 4.13.: Larmor frequency as a function of the longitudinal magnetic field B_z ; the lines are fits according to Equation (4.13).

Equation (2.19)]. It is demonstrated in this section that application of an oblique magnetic field allows simultaneous measurement of the spin dephasing as well as the spin relaxation time.

Figure 4.12 depicts spin noise spectra that are recorded in sample A at 2 K and a probe laser wavelength of 830 nm.¹² The spectra are acquired by subsequent application of transverse magnetic fields B_x of 3 and 6 mT and subtraction of the two spectra to remove the photon shot noise (see Section 3.2.2). In addition, a longitudinal magnetic field B_z is applied. The Larmor frequency is determined by the absolute value of the magnetic field and, correspondingly, the two peaks that are detected at $B_z = 0$ shift according to (see Figure 4.13)

$$f_L = \frac{g^* \mu_B}{h} \sqrt{B_x^2 + B_z^2}, \quad (4.13)$$

as indicated by the fitting curves in Figure 4.13. However, according to

¹²Note that the measurements in Section 4.2 are carried out at a laser wavelength of 850 nm. Accordingly, the measurements presented in this section are not free of perturbations and the width of the spin noise curves is not evaluated.

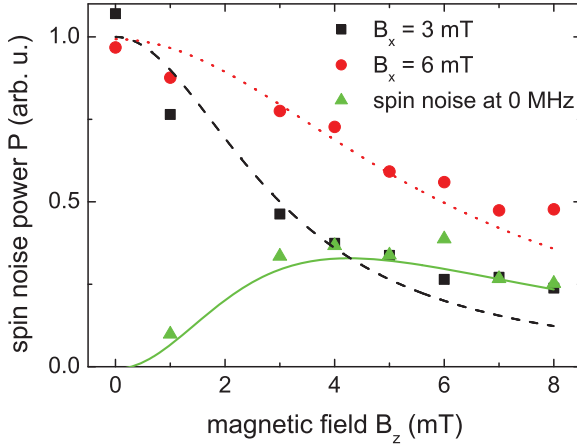


Figure 4.14.: Observed spin noise power as a function of the longitudinal magnetic field B_z for $B_x = 3$ mT (squares) and 6 mT (circles). The dashed and the dotted line are fits according to Equation (4.14). The triangles correspond to the noise power that is detected at zero frequency; the solid line corresponds to the difference of the two other lines.

Equation (2.19) only the spin polarization component \mathbf{m}_\perp perpendicular to the magnetic field $\mathbf{B} = [B_x, 0, B_z]$ is modulated with the Larmor frequency. The Faraday rotation is sensitive to the component of the stochastic spin polarization along the probe light wavevector $\mathbf{k}_{\text{laser}}$. Accordingly, the integrated spin noise power P around f_L is proportional to $\cos^2 \angle(\mathbf{m}_\perp, \mathbf{B}) = \sin^2 \angle(\mathbf{k}_{\text{laser}}, \mathbf{B})$, i.e.,

$$P \propto \frac{B_x^2}{B_x^2 + B_z^2}. \quad (4.14)$$

This expected behavior is also experimentally demonstrated (see Figure 4.14). The spin fluctuations along $\mathbf{B} = [B_x, 0, B_z]$ are correspondingly not modulated with the Larmor frequency and can be detected around zero frequency in spin noise spectroscopy as demonstrated in Figure 4.12. In Figure 4.14, also the corresponding noise that is de-

4. Experimental Results

tected in the experiment around zero frequency is plotted as a function of B_z . The dependence on B_z is well described by the difference of the two fitting curves according to Equation (4.14) revealing that spin noise spectroscopy in oblique magnetic fields is well understood.

The experiment presented in this section is carried out at relatively low magnetic fields where the difference between longitudinal and transverse spin decay, i.e., between T_1 and T_2^* , is insignificant (see Section 2.2.4). However, the results of this section show that in principle spin noise spectroscopy with an oblique magnetic field allows investigation of transverse and longitudinal spin dynamics in a single spin noise spectrum. In such an experiment, long magnet sweeping times can be avoided by taking reference curves by means of a variable retarder (see Section 3.2.2).¹³

¹³Alternatively, equivalent information could be gathered by alternately carrying out spin noise measurements in magnetic fields $\mathbf{B} = [B, 0, 0]$ and $\mathbf{B} = [0, 0, B]$. This measurement scheme however demands long magnet sweeping times. If the laser light power shows a drift, the long sweeping times do not only increase the time of measurement but may even impede this measurement scheme.

CHAPTER 5

Summary and Outlook

Semiconductor spin dynamics are most often studied by optical experiments in which a non-equilibrium spin polarization is injected by polarized light. This optical spin orientation is necessarily accompanied by energy absorption and the electron system is no longer at thermal equilibrium. The resulting electron heating and the presence of free, optically generated charge carriers can have a significant impact on the observed spin dynamics (Section 2.2). To circumvent these experimental pitfalls, spin noise spectroscopy is applied in this work to study spin dynamics in semiconductors. Spin noise spectroscopy avoids optical excitations of the examined electron system and enables investigations of the electron spin dynamics in semiconductors very close to thermal equilibrium (Section 2.1). This technique measures the fluctuating stochastic spin polarization of the electron ensemble (Sections 2.3 and 2.4) via the optical Faraday effect, i.e., the spin fluctuations of the electron ensemble are mapped onto the polarization state of the probe laser which can be tuned into the transparency region of the sample. Correlations in the detected time domain signal reveal the underlying

spin dynamics of the electron system at thermal equilibrium which are studied by spectral analysis (Section 2.5). The experimental realization of spin noise spectroscopy in this work shows a detection sensitivity for the relevant frequency range and for sufficiently high probe laser power close to the standard quantum limit (Sections 3.1 and 3.2).

Real-time detection of electron spin dynamics is an integral part of the measurement principle of spin noise spectroscopy and requires high-bandwidth photodetection and spectrum analysis (Section 3.3). Prior to this work, spin noise spectroscopy has been limited to frequencies smaller than 1 GHz. This work introduces and assesses different routes to mitigate this technical limitation for universal application of semiconductor spin noise spectroscopy. Electrical down-conversion of the spin noise signal is demonstrated in Section 3.3.1. However, electrical frequency mixing comes with a significant reduction of the detection sensitivity and the bandwidth is still limited by the performance of the photoreceiver. Simulated spin noise experiments (Section 3.3.2) reveal that also high-speed, low-resolution digitizers enable spin noise spectroscopy at the standard quantum limit, i.e., quantization noise is negligible for the real-time spectrum analysis based on fast Fourier transformation even with a resolution of the digitizer as low as 3 bit. The highly efficient spectrum analysis in this work can correspondingly be extended to a considerably larger bandwidth of several GHz. In contrast, the advancement of ultrafast spin noise spectroscopy (Section 3.3.3) disposes of the technical limitation of spin noise spectroscopy to low frequencies. In ultrafast spin noise spectroscopy, pulsed probe laser light is utilized instead of the hitherto used continuous-wave probe light. The detected spin dynamics appear to slow down under this stroboscopic sampling and spin dynamics at frequencies of around 16 GHz are measured with an 80 MHz photodetector (Section 4.2). The maximum precession frequency of the electron spins that can be resolved by this technique is only limited by the inverse pulse width while the bandwidth of the spin dynamics is, however, still limited by the bandwidth of the photodetector as well as the laser repetition rate.

Spin noise spectroscopy is applied to study the spin dynamics in a modulation-doped (110)-oriented GaAs/AlGaAs multiple quantum well structure (Section 4.1). This experiment constitutes the first application of spin noise spectroscopy to a semiconductor system of reduced

effective dimensionality. (110) GaAs/AlGaAs quantum wells are of special interest in the context of spintronics and promise long spin dephasing times for delocalized electronic spins since the Dyakonov-Perel spin dephasing mechanism is inefficient for spins aligned along the growth direction of these structures. These long spin lifetimes have, nevertheless, not been measured at low temperatures prior to this work since measurements with conventional experimental techniques that rely on optical spin orientation are obviated due to the presence of photogenerated holes. The strong influence of optically created holes on the observed spin dephasing times is demonstrated in Section 4.1.1 by tuning the spin noise probe laser close to the optical resonance. In fact, at sufficiently large detuning, the longest reported spin dephasing times for delocalized electronic spins in GaAs based quantum wells of $T_2 = 24(2)$ ns are found in this work. Also, the anisotropic spin dephasing, which results from the Dyakonov-Perel mechanism being still effective for in-plane spins, is demonstrated by application of a small in-plane magnetic field that rotates the spins into the quantum well plane where they rapidly dephase (Section 4.1.2). Furthermore, systematic variation of the probe volume shows that the finite transit time of an electron through the laser spot results in time-of-flight broadening of the spin noise spectra (Section 4.1.3). The influence of these transit time effects on the observed spin noise spectra is modeled; calculated and experimental data show good agreement. This time-of-flight broadening should uniquely allow the study of Brownian motion of electrons at thermal equilibrium. Finally, the mechanisms that possibly dominate spin dephasing of spins aligned along the growth direction at low temperatures are discussed (Section 4.1.4). Two mechanisms are elaborated in detail: spin dephasing by Rashba fields resulting from growth imperfections and by random Rashba fields that originate from inevitable dopant fluctuations in the doping sheets. The observed temperature dependence favors the latter possibility.

The new experimental technique of ultrafast spin noise spectroscopy which is developed in this work is applied to study the spin dynamics in n -type bulk GaAs in transverse magnetic fields (Section 4.2). Two different bulk samples are studied, one slightly below the metal-to-insulator transition, the other one well above. The broadening of the spin dephasing rates in the low doped sample is significantly smaller

than reported for a similar sample investigated by resonant spin amplification [16]. The experimental findings in this work directly disprove the theoretical assessment that the observed spin dephasing results from a thermal spread of the effective Landé factor. Instead, the observed inhomogeneous spin dephasing in this work is attributed to spatial inhomogeneities of the effective g -factor. The stronger spin dephasing in Reference 16 may accordingly be related to the inhomogeneous excitation profile that enhances such spatial inhomogeneities. The higher doped sample shows a less pronounced increase of the spin dephasing rates in a transverse magnetic field. However, this finding still lacks a proper explanation since no broadening of the spin noise spectra at all is expected in this doping and magnetic field regime. Furthermore, the temperature, doping, and magnetic field dependence of the effective electron Landé g -factor are investigated (Section 4.2.2). The temperature dependence and the absolute value of g^* in the high doped sample is quantitatively well modeled by the conduction band edge value and the energy dependence of the effective Landé factor in GaAs. However, the unknown impurity band structure in the low doped sample only allows a qualitative assessment. The magnetic field dependence of the effective electron g -factor is in both samples quite moderate in the applied magnetic field range of up to 3 T indicating that the effects of Landau quantization that are observed for free electrons in undoped samples are suppressed due to electron localization (in the low doped sample) or due to strong impurity scattering (in the high doped sample).

Spin noise spectroscopy is usually carried out in the Voigt geometry, i.e., a magnetic field is applied transverse to the probe light wavevector to modulate the measured stochastic spin polarization. In Section 4.3, a novel geometry for spin noise spectroscopy is introduced where a magnetic field with components parallel and perpendicular to the light propagation is used. This geometry enables simultaneous detection of transverse and longitudinal spin dynamics, i.e., spin dephasing as well as spin relaxation in a single measurement. Correspondingly, this experiment can easily distinguish between homogeneous and inhomogeneous spin dephasing mechanisms that can contribute to the spin decay in magnetic fields as discussed in the previous paragraph.

In summary, this work yields profound insight into the spin dynamics of semiconductor systems very close to thermal equilibrium and,

thereby, demonstrates that semiconductor spin noise spectroscopy is an ideal tool to investigate spin dynamics of resident electrons in semiconductors. The extensive assessment of the detection sensitivity and several routes to extend the experimental bandwidth may lay the basis for future spin noise measurements in very small systems, such as single self-assembled quantum dots, and in systems with high spin dephasing rates, such as n -type bulk GaAs at room temperature. The measurement principle of spin noise spectroscopy is not limited to semiconductors and, especially, the experimental advancement of ultrafast spin noise spectroscopy should allow the investigation of samples with ferromagnetic order where the spin precession frequencies are in the GHz range due to the spontaneous magnetization of the sample (see Appendix A). Such experiments may for instance allow the study of noise in the vicinity to magnetic phase transitions or Bose-Einstein condensation of magnons [180].

APPENDIX A

Spin Noise Spectroscopy in Materials with Magnetic Order

The main part of this dissertation focuses on spin noise spectroscopy in non-magnetic semiconductors. The assumption of an ensemble of independent spins is widely valid to describe these spin noise experiments in semiconductors. However, this modeling is obviously illegitimate for a spin system with magnetic order. On the one hand, spin noise spectroscopy may allow to study the transition of such a sample system to the paramagnetic phase. On the other hand, even in the magnetically ordered phase the spin polarization still fluctuates. This fact follows from the dissipation-fluctuation theorem and was, e.g., demonstrated in magnetometric investigations of spin glasses [24, 25]. This appendix assesses if also the optical approach to detect spin fluctuations via Faraday rotation of probe laser light, i.e., spin noise spectroscopy, is sensitive to these magnetic fluctuations. Contrary to the modeling in the Sections 2.3 and 2.4, spin fluctuations in the presence of magnetic order have to be viewed as thermally excited collective magnetic modes. This picture is further discussed in Section A.1 where also the correspond-

ing Faraday rotation noise power is estimated. Section A.2 focuses on the actual experiments in which yttrium iron garnet films are examined. The ferrimagnet yttrium iron garnet has developed into a quintessential material for studying magnetic oscillation and waves. Recently, room temperature Bose-Einstein condensation of magnons was demonstrated in this material [180]. The investigated samples are provided by the group of Professor Demokritov at the University of Münster where the films were also characterized by ferromagnetic resonance.

A.1. Model

In the following, a ferromagnetic thin film with lateral dimensions a and b in an external magnetic field applied in x -direction, $\mathbf{B} = [B, 0, 0]$, i.e., transverse to the light propagation is considered. The film is assumed to be uniformly magnetized along the external magnetic field direction so that the film consists of a single magnetic domain. The average magnetization is accordingly given by $\mathbf{M} = [M_S, 0, 0]$ and correspondingly no magnetization component along the direction of light propagation is measured in time average, i.e., $\langle M_z \rangle = 0$. However, thermal magnetization noise leads to a finite standard deviation $\langle M_z^2 \rangle$. Standing magnetic waves are thermally excited in the sample and are characterized by the wavevector $\mathbf{k} = [n\pi/a, m\pi/b]$ with $n, m = 0, 1, 2, \dots$. At $\mathbf{k} = 0$, the magnetic mode corresponds to a uniform precession of the magnetization around its equilibrium direction. Spin noise spectroscopy can only detect magnetic modes with a wavelength larger than the probe spot diameter $2w_0$. Hence, around $N_{\text{modes}} \approx ab/w_0^2$ magnetic modes contribute to the detected Faraday rotation. Each of these modes is activated by the thermal energy $\sim k_B T$. In the following, the contribution to $\langle M_z^2 \rangle$ per mode is estimated. As only modes close to the uniform mode are detected, it should suffice to consider the energy of the uniform mode and neglect dipolar and exchange interaction. The magnetic energy density is given by

$$U = -\mathbf{B} \cdot \mathbf{M} + \frac{\mu_0}{2} M_z^2, \quad (\text{A.1})$$

where the first term is the Zeeman energy and the second term is the demagnetization energy in the case of a thin film. All other anisotropies besides this shape anisotropy are disregarded. It is easy to see that the uniform magnetization along the direction of the in-plane external magnetic field represents the ground state of this system. The frequency of the uniform magnetic mode can be calculated from this energy density by harmonic expansion around the equilibrium magnetization [181]:

$$\omega(\mathbf{k} = 0) = \frac{g^* \mu_B}{\hbar} \sqrt{B(B + \mu_0 M_S)}. \quad (\text{A.2})$$

A magnetization component perpendicular to the sample plane increases the energy of the system. The Zeeman contribution can be neglected ($B \ll \mu_0 M_S$) since very small magnetic fields are applied in the experiment. Hence, thermal fluctuations yield a standard deviation of (neglecting all numerical factors of the order of unity)

$$\langle M_z^2 \rangle \approx N_{\text{modes}} \frac{k_B T}{\mu_0 V_{\text{sample}}}, \quad (\text{A.3})$$

where $V_{\text{sample}} = abl$ is the sample volume. The expected Faraday rotation noise can be calculated from the literature values for the specific Faraday rotation ψ_F [rad/cm] assuming a linear relation between magnetization and Faraday rotation:

$$\begin{aligned} P = \sigma_{\theta_F}^2 &\approx \frac{\langle M_z^2 \rangle}{M_S^2} (\psi_F l)^2 \\ &\approx \psi_F^2 \frac{(k_B T)^2}{\mu_0 M_S^2} \frac{l}{w_0^2}. \end{aligned} \quad (\text{A.4})$$

Strong focusing accordingly increases the spin noise power. This can however result in a significant inhomogeneous broadening of the noise spectrum if the magnon dispersion $\omega(\mathbf{k})$ significantly differs from $\omega(0)$ for $k = \pi/w_0$ which limits spin noise spectroscopy, e.g., in yttrium iron garnet to rather large probe laser spots of several ten microns.¹ The

¹The magnetic dispersion can be calculated with the Equations (16) and (35) from Reference 182 ($n = n' = 0$). The magnon dispersion is different for wavevectors

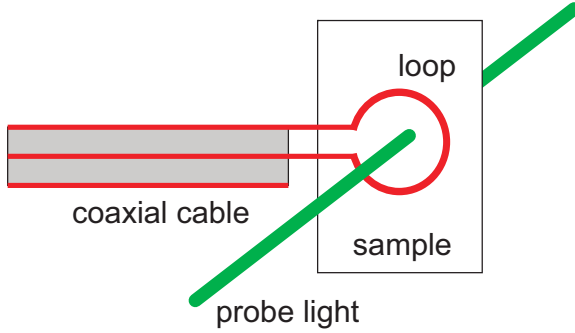


Figure A.1.: Excitation of magnetic oscillations by means of radio frequency antenna fabricated by short-circuiting a coaxial cable.

specific spin noise power at room temperature is $P/l \approx 10^{-30} \text{ rad}^2/\text{cm}$ according to Equation (A.4) for yttrium iron garnet films ($w_0 = 10 \mu\text{m}$, $\psi_F \approx 50 \text{ rad/cm}$, $\mu_0 M_S \approx 175 \text{ mT}$ [183]) while $P/l \approx 10^{-28} \text{ rad}^2/\text{cm}$ for nickel films ($\psi_F \approx 1400 \text{ rad/cm}$ [184], $\mu_0 M_S = 609 \text{ mT}$ [185]). Yttrium iron garnet is an insulator and shows only low absorption for a large portion of the visible optical spectrum which allows usage of quite thick films of several microns for Faraday rotation measurements. Nickel and other ferromagnetic metals allow only a film thickness of the order of the optical penetration depth around 10 nm so that the lower expected specific noise power in yttrium iron garnet films can be compensated by a higher film thickness.

A.2. Experiment

The detection of thermally excited spin noise in ferromagnets definitely demands high detection sensitivity and very long integration times. The Faraday rotation noise is enhanced by exciting magnetic fluctuations with radio frequency oscillations. To this end, a radio frequency antenna, fabricated by short-circuiting the end of a coaxial cable, is placed

parallel, \mathbf{k}_{\parallel} , and perpendicular, \mathbf{k}_{\perp} , to the magnetic field direction. This fact may be exploited in future experiments by focusing with cylindrical lenses.

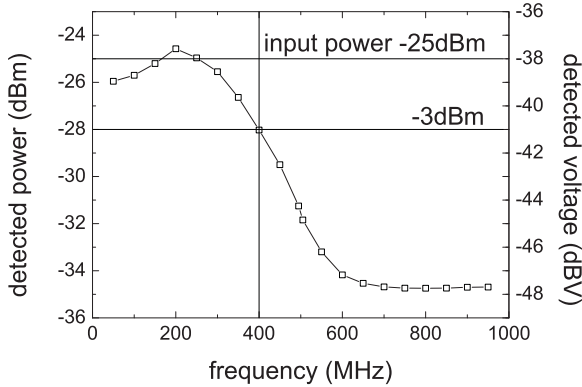


Figure A.2.: Frequency dependent sensitivity of the utilized digitizer *AlazarTech ATS9870* ($R = 8$ bit and $f_S = 1$ GS/s). The analog components of the digitizer show a 3 dB-bandwidth around 400 MHz.

around the probe laser spot (see Figure A.1). The antenna is connected to a signal generator which is tuned to the resonance frequency of the uniform magnetic precession.

The resonance frequency of the uniform magnetic mode of a thin magnetic film can be adjusted according to Equation (A.2) to an arbitrary value by tuning the applied magnetic field B . However, this equation is only valid as long a uniform magnetization state is present in the sample. Accordingly, no uniform magnetic precession is observed in ferromagnetic resonance measurements below a certain magnetic field. Measurements of ferromagnetic resonance show that a field around 7 mT is needed to achieve a single domain state in a $5 \mu\text{m}$ thick yttrium iron garnet film which results in a frequency of around 1.04 GHz. Thinner films have a stronger shape anisotropy and a uniform magnetization is correspondingly expected at lower magnetic fields. In fact, a $0.5 \mu\text{m}$ thick yttrium iron garnet film shows uniform magnetic precession around 500 MHz at a magnetic field around 1.5 mT. The available balanced receiver *New Focus 1607-AC-FS* with a 3 dB-bandwidth of 650 MHz (see Section 3.1) and digitizer *AlazarTech ATS9870* ($R = 8$ bit and $f_S = 1$ GS/s) limit the spin noise measurements on yttrium iron garnet

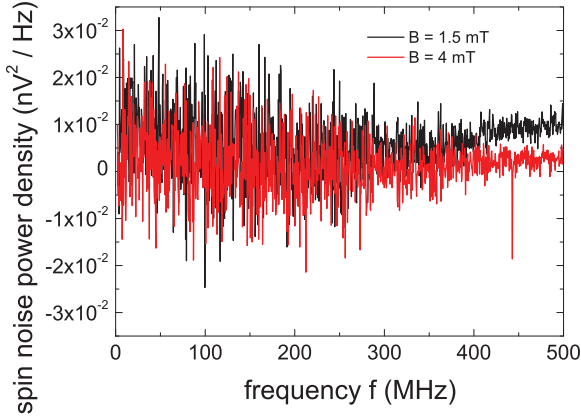


Figure A.3.: Faraday rotation noise spectra acquired according to the setup in Figure A.1 in a $0.5 \mu\text{m}$ thick yttrium iron garnet film. The magnetic field is set to 1.5 mT (dark-colored curve) so that the applied radio frequency signal at 500 MHz is resonant with the precession frequency of the uniform magnetic mode. For comparison, the light-colored curve is acquired with an external field of 4 mT .

to the film thickness of $0.5 \mu\text{m}$. Unfortunately, the analog components of the digitizer show a 3 dB -bandwidth of around 400 MHz deviating from the specifications (see Figure A.2) which reduces the detection sensitivity in the relevant frequency range. The signal generator is set to 500 MHz at an output power of 23 dBm while the corresponding magnetic field of 1.5 mT is applied transverse to the sample. A frequency doubled, diode pumped solid state laser is used as probe laser (*Coherent Verdi V6*, $\lambda = 532 \text{ nm}$). Reference noise spectra for subtraction of the optical shot noise background are acquired by switching off the output of the signal generator. Figure A.3 shows such a noise spectrum (dark curve) for very long integration times of around 16 hours . The light-colored curve depicts for comparison the corresponding curve with an external field of 4 mT where the applied radio frequency signal is off-resonant. Accordingly, spin noise spectroscopy is probably sensitive enough to detect the resonantly excited magnetic oscillations. However,

further investigations clearly demand an extension of the experimental bandwidth. Besides using ultrafast digitizers (see Section 3.3.2), this could be achieved by ultrafast spin noise spectroscopy employing pulsed lasers (see Section 3.3.3).

Bibliography

- [1] G. Lampel, “Nuclear Dynamic Polarization by Optical Electronic Saturation and Optical Pumping in Semiconductors”, *Phys. Rev. Lett.* **20**, 491 (1968).
- [2] R. R. Parsons, “Band-To-Band Optical Pumping in Solids and Polarized Photoluminescence”, *Phys. Rev. Lett.* **23**, 1152 (1969).
- [3] S. Datta and B. Das, “Electronic analog of the electro-optic modulator”, *Appl. Phys. Lett.* **56**, 665 (1990).
- [4] S. A. Wolf, D. D. Awschalom, R. A. Buhrman, J. M. Daughton, S. von Molnár, M. L. Roukes, A. Y. Chtchelkanova, and D. M. Treger, “Spintronics: A Spin-Based Electronics Vision for the Future”, *Science* **294**, 1488 (2001).
- [5] I. Zutic, J. Fabian, and S. D. Sarma, “Spintronics: Fundamentals and applications”, *Rev. Mod. Phys.* **76**, 323 (2004).
- [6] D. D. Awschalom and M. E. Flatté, “Challenges for semiconductor spintronics”, *Nature Phys.* **3**, 153 (2007).
- [7] J. Fabian, A. Matos-Abiague, C. Ertler, P. Stano, and I. Zutic, “Semiconductor Spintronics”, *Acta Phys. Slov.* **57**, 565 (2007).

- [8] B. E. Kane, “A silicon-based nuclear spin quantum computer”, *Nature* **393**, 133 (1998).
- [9] D. Loss and D. P. DiVincenzo, “Quantum computation with quantum dots”, *Phys. Rev. A* **57**, 120 (1998).
- [10] A. Imamoglu, D. D. Awschalom, G. Burkard, D. P. DiVincenzo, D. Loss, M. Sherwin, and A. Small, “Quantum Information Processing Using Quantum Dot Spins and Cavity QED”, *Phys. Rev. Lett.* **83**, 4204 (1999).
- [11] F. Meier and B. P. Zakharchenya, editors, *Optical Orientation (Modern Problems in Condensed Matter Sciences, Vol 8)*, North-Holland, Amsterdam, 1984.
- [12] G. Feher and E. A. Gere, “Electron Spin Resonance Experiments on Donors in Silicon. II. Electron Spin Relaxation Effects”, *Phys. Rev.* **114**, 1245 (1959).
- [13] A. P. Heberle, W. W. Rühle, and K. Ploog, “Quantum beats of electron Larmor precession in GaAs wells”, *Phys. Rev. Lett.* **72**, 3887 (1994).
- [14] J. J. Baumberg, D. D. Awschalom, N. Samarth, H. Luo, and J. K. Furdyna, “Spin beats and dynamical magnetization in quantum structures”, *Phys. Rev. Lett.* **72**, 717 (1994).
- [15] R. E. Worsley, N. J. Traynor, T. Grevatt, and R. T. Harley, “Transient Linear Birefringence in GaAs Quantum Wells: Magnetic Field Dependence of Coherent Exciton Spin Dynamics”, *Phys. Rev. Lett.* **76**, 3224 (1996).
- [16] J. M. Kikkawa and D. D. Awschalom, “Resonant Spin Amplification in n-Type GaAs”, *Phys. Rev. Lett.* **80**, 4313 (1998).
- [17] G. M. Müller, M. Oestreich, M. Römer, and J. Hübner, “Semiconductor spin noise spectroscopy: Fundamentals, accomplishments, and challenges”, *Physica E* **43**, 569 (2010).
- [18] R. Kubo, “The fluctuation-dissipation theorem”, *Rep. Prog. Phys.* **29**, 255 (1966).

-
- [19] A. Einstein, “Über die von der molekularkinetischen Theorie der Wärme geforderte Bewegung von in ruhenden Flüssigkeiten suspendierten Teilchen”, *Ann. Phys.* **17**, 549 (1905).
- [20] S. Kos and P. Littlewood, “Statistical physics: Hear the noise”, *Nature* **431**, 29 (2004).
- [21] F. Bloch, “Nuclear Induction”, *Phys. Rev.* **70**, 460 (1946).
- [22] T. Sleator, E. L. Hahn, C. Hilbert, and J. Clarke, “Nuclear-spin noise”, *Phys. Rev. Lett.* **55**, 1742 (1985).
- [23] M. Ocio, H. Bouchiat, and P. Monod, “Observation of 1/f magnetic fluctuations in a spin glass”, *J. Physique Lett.* **46**, 647 (1985).
- [24] W. Reim, R. H. Koch, A. P. Malozemoff, M. B. Ketchen, and H. Maletta, “Magnetic Equilibrium Noise in Spin-Glasses: $\text{Eu}_{0.4}\text{Sr}_{0.6}\text{S}$ ”, *Phys. Rev. Lett.* **57**, 905 (1986).
- [25] M. Alba, J. Hammann, M. Ocio, P. Refregier, and H. Bouchiat, “Spin-glass dynamics from magnetic noise, relaxation, and susceptibility measurements (invited)”, *J. Appl. Phys.* **61**, 3683 (1987).
- [26] N. E. Israeloff, M. B. Weissman, G. J. Nieuwenhuys, and J. Kossiorowska, “Electrical noise from spin fluctuations in CuMn ”, *Phys. Rev. Lett.* **63**, 794 (1989).
- [27] B. C. Stipe, H. J. Mamin, T. D. Stowe, T. W. Kenny, and D. Rugar, “Magnetic Dissipation and Fluctuations in Individual Nanomagnets Measured by Ultrasensitive Cantilever Magnetometry”, *Phys. Rev. Lett.* **86**, 2874 (2001).
- [28] H. J. Mamin, R. Budakian, B. W. Chui, and D. Rugar, “Detection and Manipulation of Statistical Polarization in Small Spin Ensembles”, *Phys. Rev. Lett.* **91**, 207604 (2003).
- [29] D. Rugar, R. Budakian, H. J. Mamin, and B. W. Chui, “Single spin detection by magnetic resonance force microscopy”, *Nature* **430**, 329 (2004).

- [30] R. Budakian, H. J. Mamin, B. W. Chui, and D. Rugar, “Creating Order from Random Fluctuations in Small Spin Ensembles”, *Science* **307**, 408 (2005).
- [31] H. J. Mamin, R. Budakian, B. W. Chui, and D. Rugar, “Magnetic resonance force microscopy of nuclear spins: Detection and manipulation of statistical polarization”, *Phys. Rev. B* **72**, 024413 (2005).
- [32] N. Müller and A. Jerschow, “Nuclear spin noise imaging”, *Proc. Natl. Acad. Sci. USA* **103**, 6790 (2006).
- [33] E. B. Aleksandrov and V. S. Zapasskii, “Magnetic resonance in the Faraday-rotation noise spectrum”, *Sov. Phys. JETP* **54**, 64 (1981).
- [34] M. Faraday, “On the Magnetic Affection of Light, and on the Distinction between the Ferromagnetic and Diamagnetic Conditions of Matter”, *Philos. Mag.* **29**, 249 (1846).
- [35] W. Happer and B. S. Mathur, “Off-Resonant Light as a Probe of Optically Pumped Alkali Vapors”, *Phys. Rev. Lett.* **18**, 577 (1967).
- [36] A. Kuzmich, L. Mandel, J. Janis, Y. E. Young, R. Egnisman, and N. P. Bigelow, “Quantum nondemolition measurements of collective atomic spin”, *Phys. Rev. A* **60**, 2346 (1999).
- [37] B. Julsgaard, A. Kozhekin, and E. S. Polzik, “Experimental long-lived entanglement of two macroscopic objects”, *Nature* **413**, 400 (2001).
- [38] V. B. Braginsky, Y. I. Vorontsov, and K. S. Thorne, “Quantum Nondemolition Measurements”, *Science* **209**, 547 (1980).
- [39] V. B. Braginsky and F. Y. Khalili, “Quantum nondemolition measurements: the route from toys to tools”, *Rev. Mod. Phys.* **68**, 1 (1996).
- [40] P. Grangier, J. A. Levenson, and J.-P. Poizat, “Quantum nondemolition measurements in optics”, *Nature* **396**, 537 (1998).

-
- [41] M. Oestreich, M. Römer, R. J. Haug, and D. Hägele, “Spin Noise Spectroscopy in GaAs”, *Phys. Rev. Lett.* **95**, 216603 (2005).
- [42] M. Römer, J. Hübner, and M. Oestreich, “Spin noise spectroscopy in semiconductors”, *Rev. Sci. Instrum.* **78**, 103903 (2007).
- [43] Y. Ohno, R. Terauchi, T. Adachi, F. Matsukura, and H. Ohno, “Spin Relaxation in GaAs(110) Quantum Wells”, *Phys. Rev. Lett.* **83**, 4196 (1999).
- [44] S. Döhrmann, D. Hägele, J. Rudolph, M. Bichler, D. Schuh, and M. Oestreich, “Anomalous Spin Dephasing in (110) GaAs Quantum Wells: Anisotropy and Intersubband Effects”, *Phys. Rev. Lett.* **93**, 147405 (2004).
- [45] R. de L. Kronig, “On the theory of dispersion of x-rays”, *J. Opt. Soc. Am.* **12**, 547 (1926).
- [46] H. A. Kramers, “La diffuision de la lmuire par les atomes”, *Atti. Congr. Int. Fis.* **2**, 545 (1927).
- [47] M. A. Hopkins, R. J. Nicholas, P. Pfeffer, W. Zawadzki, D. Gauthier, J. C. Portal, and M. A. DiForte-Poisson, “A study of the conduction band non-parabolicity, anisotropy and spin splitting in GaAs and InP”, *Semicond. Sci. Technol.* **2**, 568 (1987).
- [48] P. Pfeffer and W. Zawadzki, “Conduction electrons in GaAs: Five-level k - p theory and polaron effects”, *Phys. Rev. B* **41**, 1561 (1990).
- [49] P. Pfeffer and W. Zawadzki, “Five-level k - p model for the conduction and valence bands of GaAs and InP”, *Phys. Rev. B* **53**, 12813 (1996).
- [50] J. J. Sakurai, *Modern Quantum Mechanics*, Addison-Wesley, Reading, 1994.
- [51] G. Dresselhaus, “Spin-Orbit Coupling Effects in Zinc Blende Structures”, *Phys. Rev.* **100**, 580 (1955).

- [52] M. I. Dyakonov and V. I. Perel, “Spin Relaxation of Conduction Electrons in Noncentrosymmetric Semiconductors”, *Sov. Phys. Solid State* **13**, 3023 (1972).
- [53] R. Winkler, *Spin-orbit Coupling Effects in Two-Dimensional Electron and Hole Systems (Springer Tracts in Modern Physics)*, Springer, Berlin, 1 edition, 2003.
- [54] I. Vurgaftman, J. R. Meyer, and L. R. Ram-Mohan, “Band parameters for III–V compound semiconductors and their alloys”, *J. Appl. Phys.* **89**, 5815 (2001).
- [55] S. Pfalz, R. Winkler, T. Nowitzki, D. Reuter, A. D. Wieck, D. Hägele, and M. Oestreich, “Optical orientation of electron spins in GaAs quantum wells”, *Phys. Rev. B* **71**, 165305 (2005).
- [56] B. Shklovskii and A. Efros, *Electronic Properties of Doped Semiconductors*, Springer, Berlin, 1984.
- [57] R. A. Abram, G. J. Rees, and B. L. H. Wilson, “Heavily doped semiconductors and devices”, *Adv. Phys.* **27**, 799 (1978).
- [58] N. F. Mott, “Metal-Insulator Transition”, *Rev. Mod. Phys.* **40**, 677 (1968).
- [59] R. Dingle, H. L. Störmer, A. C. Gossard, and W. Wiegmann, “Electron mobilities in modulation-doped semiconductor heterojunction superlattices”, *Appl. Phys. Lett.* **33**, 665 (1978).
- [60] L. M. Roth, B. Lax, and S. Zwerdling, “Theory of Optical Magneto-Absorption Effects in Semiconductors”, *Phys. Rev.* **114**, 90 (1959).
- [61] P. Y. Yu and M. Cardona, *Fundamentals of Semiconductors*, Springer, Berlin, 3rd edition, 2005.
- [62] W. Zawadzki, P. Pfeffer, R. Bratschitsch, Z. Chen, S. T. Cundiff, B. N. Murdin, and C. R. Pidgeon, “Temperature dependence of the electron spin g factor in GaAs”, *Phys. Rev. B* **78**, 245203 (2008).

-
- [63] J. Hübner, S. Döhrmann, D. Hägele, and M. Oestreich, “Temperature-dependent electron Landé g factor and the interband matrix element of GaAs”, *Phys. Rev. B* **79**, 193307 (2009).
- [64] M. J. Yang, R. J. Wagner, B. V. Shanabrook, J. R. Waterman, and W. J. Moore, “Spin-resolved cyclotron resonance in InAs quantum wells: A study of the energy-dependent g factor”, *Phys. Rev. B* **47**, 6807 (1993).
- [65] I. Hapke-Wurst, “Resonanter Magnetotransport durch selbstorganisierte InAs Quantenpunkte”, Dissertation, Univ. Hannover, 2002.
- [66] V. Fock, “Bemerkung zur Quantelung des harmonischen Oszillators im Magnetfeld”, *Z. Phys. A* **47**, 446 (1928).
- [67] C. G. Darwin, “The Diamagnetism of the Free Electron”, *Math. Proc. Cambridge Philos. Soc.* **27**, 86 (1931).
- [68] Y. Yafet, R. W. Keyes, and E. N. Adams, “Hydrogen atom in a strong magnetic field”, *J. Phys. Chem. Solids* **1**, 137 (1956).
- [69] P. C. Makado and N. C. McGill, “Energy levels of a neutral hydrogen-like system in a constant magnetic field of arbitrary strength”, *J. Phys. C* **19**, 873 (1986).
- [70] D. Pines and C. P. Slichter, “Relaxation Times in Magnetic Resonance”, *Phys. Rev.* **100**, 1014 (1955).
- [71] G. Fishman and G. Lampel, “Spin relaxation of photoelectrons in p -type gallium arsenide”, *Phys. Rev. B* **16**, 820 (1977).
- [72] N. Bloembergen, E. M. Purcell, and R. V. Pound, “Relaxation Effects in Nuclear Magnetic Resonance Absorption”, *Phys. Rev.* **73**, 679 (1948).
- [73] R. J. Elliott, “Theory of the Effect of Spin-Orbit Coupling on Magnetic Resonance in Some Semiconductors”, *Phys. Rev.* **96**, 266 (1954).

- [74] Y. Yafet, *Solid State Physics*, volume 14, pages 2–98, Academic, New York, 1963.
- [75] P. Boguslawski, “Electron-electron spin-flip scattering and spin relaxation in III-V and II-VI semiconductors”, *Solid State Commun.* **33**, 389 (1980).
- [76] J. N. Chazalviel, “Spin relaxation of conduction electrons in n -type indium antimonide at low temperature”, *Phys. Rev. B* **11**, 1555 (1975).
- [77] J. H. Jiang and M. W. Wu, “Electron-spin relaxation in bulk III-V semiconductors from a fully microscopic kinetic spin Bloch equation approach”, *Phys. Rev. B* **79**, 125206 (2009).
- [78] E. I. Rashba, “Properties of Semiconductors with an Extremum Loop”, *Sov. Phys. Solid State* **2**, 1109 (1960).
- [79] Y. A. Bychkov and E. I. Rashba, “Oscillatory effects and the magnetic susceptibility of carriers in inversion layers”, *J. Phys. C* **17**, 6039 (1984).
- [80] L. Vervoort, R. Ferreira, and P. Voisin, “Effects of interface asymmetry on hole subband degeneracies and spin-relaxation rates in quantum wells”, *Phys. Rev. B* **56**, R12744 (1997).
- [81] M. Dyakonov, editor, *Spin Physics in Semiconductors (Springer Series in Solid-State Sciences)*, Springer, Berlin, 1st edition, 2008.
- [82] M. Wu and C. Ning, “A novel mechanism for spin dephasing due to spin-conserving scatterings”, *Eur. Phys. J. B* **18**, 373 (2000).
- [83] M. W. Wu, “Spin Dephasing Induced by Inhomogeneous Broadening in D’yakonov-Perel’ Effect in a n -doped GaAs Quantum Well”, *J. Phys. Soc. Jpn.* **70**, 2195 (2001).
- [84] M. Glazov and E. Ivchenko, “Precession spin relaxation mechanism caused by frequent electron-electron collisions”, *JETP Lett.* **75**, 403 (2002).

-
- [85] M. Glazov and E. Ivchenko, “Effect of electron-electron interaction on spin relaxation of charge carriers in semiconductors”, *JETP* **99**, 1279 (2004).
- [86] M. I. Dyakonov and V. Y. Kachorovskii, “Spin relaxation of two-dimensional electrons in noncentrosymmetric semiconductors”, *Sov. Phys. Semicond.* **20**, 110 (1986).
- [87] M. A. Brand, A. Malinowski, O. Z. Karimov, P. A. Marsden, R. T. Harley, A. J. Shields, D. Sanvitto, D. A. Ritchie, and M. Y. Simmons, “Precession and Motional Slowing of Spin Evolution in a High Mobility Two-Dimensional Electron Gas”, *Phys. Rev. Lett.* **89**, 236601 (2002).
- [88] D. Stich, J. Zhou, T. Korn, R. Schulz, D. Schuh, W. Wegscheider, M. W. Wu, and C. Schüller, “Effect of Initial Spin Polarization on Spin Dephasing and the Electron g Factor in a High-Mobility Two-Dimensional Electron System”, *Phys. Rev. Lett.* **98**, 176401 (2007).
- [89] E. Y. Sherman, “Random spin-orbit coupling and spin relaxation in symmetric quantum wells”, *Appl. Phys. Lett.* **82**, 209 (2003).
- [90] M. M. Glazov, E. Y. Sherman, and V. K. Dugaev, “Two-dimensional electron gas with spin-orbit coupling disorder”, *Physica E* **42**, 2157 (2010).
- [91] A. D. Margulis and V. A. Margulis, “Precession mechanism of conductive electron-spin relaxation in semiconductors in a strong magnetic field”, *Sov. Phys. Solid State* **25**, 918 (1983).
- [92] F. X. Bronold, I. Martin, A. Saxena, and D. L. Smith, “Magnetic-field dependence of electron spin relaxation in n-type semiconductors”, *Phys. Rev. B* **66**, 233206 (2002).
- [93] G. L. Bir, A. G. Aronov, and G. E. Pikus, “Spin relaxation of electrons due to scattering by holes”, *Sov. Phys. JETP* **42**, 705 (1976).

- [94] M. Z. Maialle, “Spin relaxation of electrons in p-doped quantum wells via the electron-hole exchange interaction”, *Phys. Rev. B* **54**, 1967 (1996).
- [95] J. Zhou and M. W. Wu, “Spin relaxation due to the Bir-Aronov-Pikus mechanism in intrinsic and p -type GaAs quantum wells from a fully microscopic approach”, *Phys. Rev. B* **77**, 075318 (2008).
- [96] A. W. Overhauser, “Polarization of Nuclei in Metals”, *Phys. Rev.* **92**, 411 (1953).
- [97] M. Dyakonov and V. Perel, “Optical Orientation in a system of electrons and lattice nuclei in semiconductors”, *Sov. Phys. JETP* **38**, 177 (1974).
- [98] D. Paget, G. Lampel, B. Sapoval, and V. I. Safarov, “Low field electron-nuclear spin coupling in gallium arsenide under optical pumping conditions”, *Phys. Rev. B* **15**, 5780 (1977).
- [99] I. A. Merkulov, A. L. Efros, and M. Rosen, “Electron spin relaxation by nuclei in semiconductor quantum dots”, *Phys. Rev. B* **65**, 205309 (2002).
- [100] M. Römer, H. Bernien, G. Müller, D. Schuh, J. Hübner, and M. Oestreich, “Electron-spin relaxation in bulk GaAs for doping densities close to the metal-to-insulator transition”, *Phys. Rev. B* **81**, 075216 (2010).
- [101] P.-F. Braun et al., “Direct Observation of the Electron Spin Relaxation Induced by Nuclei in Quantum Dots”, *Phys. Rev. Lett.* **94**, 116601 (2005).
- [102] K. V. Kavokin, “Spin relaxation of localized electrons in n-type semiconductors”, *Semicond. Sci. Technol.* **23**, 114009 (2008).
- [103] R. I. Dzhioev, K. V. Kavokin, V. L. Korenev, M. V. Lazarev, B. Y. Meltser, M. N. Stepanova, B. P. Zakharchenya, D. Gammon, and D. S. Katzer, “Low-temperature spin relaxation in n-type GaAs”, *Phys. Rev. B* **66**, 245204 (2002).

-
- [104] R. I. Dzhioev, V. L. Korenev, I. A. Merkulov, B. P. Zakharchenya, D. Gammon, A. L. Efros, and D. S. Katzer, “Manipulation of the Spin Memory of Electrons in n-GaAs”, *Phys. Rev. Lett.* **88**, 256801 (2002).
- [105] I. Dzyaloshinskii, “A thermodynamic theory of ferromagnetism of antiferromagnetics”, *J. Phys. Chem. Solids* **4**, 241 (1958).
- [106] T. Moriya, “Anisotropic Superexchange Interaction and Weak Ferromagnetism”, *Phys. Rev.* **120**, 91 (1960).
- [107] K. V. Kavokin, “Anisotropic exchange interaction of localized conduction-band electrons in semiconductors”, *Phys. Rev. B* **64**, 075305 (2001).
- [108] B. I. Shklovskii, “Dyakonov-Perel spin relaxation near the metal-insulator transition and in hopping transport”, *Phys. Rev. B* **73**, 193201 (2006).
- [109] E. H. Bogardus and H. B. Bebb, “Bound-Exciton, Free-Exciton, Band-Acceptor, Donor-Acceptor, and Auger Recombination in GaAs”, *Phys. Rev.* **176**, 993 (1968).
- [110] W. Demtröder, *Laser Spectroscopy: Vol. 1: Basic Principles*, Springer, Berlin, 4th edition, 2008.
- [111] H. Bernien, “Spinrauschspektroskopie an Donatoren in GaAs”, Diplomarbeit, Univ. Hannover, 2009.
- [112] S. A. Crooker, L. Cheng, and D. L. Smith, “Spin noise of conduction electrons in n-type bulk GaAs”, *Phys. Rev. B* **79**, 035208 (2009).
- [113] M. Braun and J. König, “Faraday-rotation fluctuation spectroscopy with static and oscillating magnetic fields”, *Phys. Rev. B* **75**, 085310 (2007).
- [114] N. Wiener, “Generalized harmonic analysis”, *Acta Mathematica* **55**, 117 (1930).

- [115] A. Chintchin, “Korrelationstheorie der stationären stochastischen Prozesse”, *Mathematische Annalen* **109**, 604 (1934).
- [116] J. W. Crowe and J. R. M. Craig, “GaAs laser linewidth measurements by heterodyne detection”, *Appl. Phys. Lett.* **5**, 72 (1964).
- [117] M. G. Littman and H. J. Metcalf, “Spectrally narrow pulsed dye laser without beam expander (ET)”, *Appl. Opt.* **17**, 2224 (1978).
- [118] M. Römer, “Spinrauschspektroskopie in Halbleitern”, Dissertation, Univ. Hannover, 2010.
- [119] N. S. Jayant and P. Noll, *Digital Coding of Waveforms: Principles and Applications to Speech and Video (Prentice-Hall Signal Processing Series)*, Prentice Hall, Englewood Cliffs, 1st edition, 1984.
- [120] H. Nyquist, “Certain topics in telegraph transmission theory”, *Trans. AIEE* **47**, 617 (1928).
- [121] C. E. Shannon, “Communication in the presence of noise”, *Proc. IRE* **37**, 10 (1949).
- [122] W. R. Bennett, “Spectra of quantized signals”, *Bell Syst. Tech. J.* **27**, 446 (1948).
- [123] R. Gray, “Quantization noise spectra”, *IEEE Trans. Inf. Theory* **36**, 1220 (1990).
- [124] M. Fox, *Quantum Optics: An Introduction (Oxford Master Series in Physics, 6)*, Oxford University Press, Oxford, 2006.
- [125] S. A. Crooker, J. Brandt, C. Sandfort, A. Greulich, D. R. Yakovlev, D. Reuter, A. D. Wieck, and M. Bayer, “Spin Noise of Electrons and Holes in Self-Assembled Quantum Dots”, *Phys. Rev. Lett.* **104**, 036601 (2010).
- [126] G. M. Müller, M. Römer, D. Schuh, W. Wegscheider, J. Hübner, and M. Oestreich, “Spin Noise Spectroscopy in GaAs (110) Quantum Wells: Access to Intrinsic Spin Lifetimes and Equilibrium Electron Dynamics”, *Phys. Rev. Lett.* **101**, 206601 (2008).

- [127] S. Oertel, J. Hübner, and M. Oestreich, “High temperature electron spin relaxation in bulk GaAs”, *Appl. Phys. Lett.* **93**, 132112 (2008).
- [128] J. Berezovsky, M. H. Mikkelsen, O. Gywat, N. G. Stoltz, L. A. Coldren, and D. D. Awschalom, “Nondestructive Optical Measurements of a Single Electron Spin in a Quantum Dot”, *Science* **314**, 1916 (2006).
- [129] L. Schuchman, “Dither Signals and Their Effect on Quantization Noise”, *IEEE Trans. Commun.* **12**, 162 (1964).
- [130] R. Belchamber and G. Horlick, “Use of added random noise to improve bit-resolution in digital signal averaging”, *Talanta* **28**, 547 (1981).
- [131] J. Vanderkooy and S. Lipshitz, “Resolution Below the Least Significant Bit in Digital Systems with Dither”, *J. Audio Eng. Soc.* **32**, 106 (1984).
- [132] R. Gray and T. Stockham, “Dithered quantizers”, *IEEE Trans. Inf. Theory* **39**, 805 (1993).
- [133] P. Carbone and D. Petri, “Effect of additive dither on the resolution of ideal quantizers”, *IEEE Trans. Instrum. Meas.* **43**, 389 (1994).
- [134] R. Wannamaker, S. Lipshitz, J. Vanderkooy, and J. Wright, “A theory of nonsubtractive dither”, *IEEE Trans. Signal Process.* **48**, 499 (2000).
- [135] P. Carbone and D. Petri, “Performance of stochastic and deterministic dithered quantizers”, *IEEE Trans. Instrum. Meas.* **49**, 337 (2000).
- [136] P. J. B. Koeck, “Quantization errors in averaged digitized data”, *Signal Process.* **81**, 345 (2001).
- [137] R. Skartlien and L. Oyehaug, “Quantization error and resolution in ensemble averaged data with noise”, *IEEE Trans. Instrum. Meas.* **54**, 1303 (2005).

- [138] J. Max, “Quantizing for minimum distortion”, IRE Trans. Inf. Theory **6**, 7 (1960).
- [139] S. Starosielec and D. Hägele, “Ultrafast spin noise spectroscopy”, Appl. Phys. Lett. **93**, 051116 (2008).
- [140] M. J. Howes, *Gallium Arsenide: Materials, Devices, and Circuits (Wiley Series in Solid State Devices and Circuits)*, John Wiley & Sons, Chichester, 1985.
- [141] M. Römer, “Spinfluktuationen und Spindynamik in Halbleiterstrukturen”, Diplomarbeit, Univ. Hannover, 2005.
- [142] J. S. Blakemore, *Semiconductor Statistics*, Dover Publications, Mineola, 2002.
- [143] V. V. Bel’kov, P. Olbrich, S. A. Tarasenko, D. Schuh, W. Wegscheider, T. Korn, C. Schüller, D. Weiss, W. Prettl, and S. D. Ganichev, “Symmetry and Spin Dephasing in (110)-Grown Quantum Wells”, Phys. Rev. Lett. **100**, 176806 (2008).
- [144] E. Yablonovitch, D. M. Hwang, T. J. Gmitter, L. T. Florez, and J. P. Harbison, “Van der Waals bonding of GaAs epitaxial liftoff films onto arbitrary substrates”, Appl. Phys. Lett. **56**, 2419 (1990).
- [145] A. R. Clawson, “Guide to references on III-V semiconductor chemical etching”, Mater. Sci. Eng. R **31**, 1 (2001).
- [146] E. Yablonovitch, T. Gmitter, J. P. Harbison, and R. Bhat, “Extreme selectivity in the lift-off of epitaxial GaAs films”, Appl. Phys. Lett. **51**, 2222 (1987).
- [147] A. van Geelen, P. Hageman, G. Bauhuis, P. van Rijsingen, P. Schmidt, and L. Giling, “Epitaxial lift-off GaAs solar cell from a reusable GaAs substrate”, Mater. Sci. Eng. B **45**, 162 (1997).
- [148] O. D. D. Couto, Jr., F. Iikawa, J. Rudolph, R. Hey, and P. V. Santos, “Anisotropic Spin Transport in (110) GaAs Quantum Wells”, Phys. Rev. Lett. **98**, 036603 (2007).

-
- [149] S. Döhrmann, “Spintronik in GaAs und (110)-GaAs-Quantenfilmen”, Dissertation, Univ. Hannover, 2007.
- [150] G. E. Katsoprinakis, A. T. Dellis, and I. K. Kominis, “Measurement of transverse spin-relaxation rates in a rubidium vapor by use of spin-noise spectroscopy”, *Phys. Rev. A* **75**, 042502 (2007).
- [151] G. Fasol, “Electron dephasing due to Coulomb interaction”, *Appl. Phys. Lett.* **59**, 2430 (1991).
- [152] H. Fukuyama and E. Abrahams, “Inelastic scattering time in two-dimensional disordered metals”, *Phys. Rev. B* **27**, 5976 (1983).
- [153] S. Chandrasekhar, “Stochastic Problems in Physics and Astronomy”, *Rev. Mod. Phys.* **15**, 1 (1943).
- [154] G. Bergmann, “Physical interpretation of weak localization: A time-of-flight experiment with conduction electrons”, *Phys. Rev. B* **28**, 2914 (1983).
- [155] S. Kos, A. V. Balatsky, P. B. Littlewood, and D. L. Smith, “Spin noise of itinerant fermions”, *Phys. Rev. B* **81**, 064407 (2010).
- [156] Y. Zhou and M. W. Wu, “Spin relaxation due to random Rashba spin-orbit coupling in GaAs (110) quantum wells”, *Europhys. Lett.* **89**, 57001 (2010).
- [157] A. Tackeuchi, T. Kuroda, S. Muto, Y. Nishikawa, and O. Wada, “Electron Spin-relaxation Dynamics in GaAs/AlGaAs Quantum Wells and InGaAs/InP Quantum Wells”, *Jpn. J. Appl. Phys.* **38**, 4680 (1999).
- [158] D. Hägele, S. Döhrmann, J. Rudolph, and M. Oestreich, “Electron Spin Relaxation in Semiconductors”, *Adv. Solid State Phys.* **45**, 253 (2006).
- [159] Y. Zhou and M. Wu, “A virtual intersubband spin-flip spin-orbit coupling induced spin relaxation in GaAs (110) quantum wells”, *Solid State Commun.* **149**, 2078 (2009).

- [160] S.-W. Chang and S.-L. Chuang, “Strain-induced enhancement of spin relaxation times in [110] and [111] grown quantum wells”, *Phys. Rev. B* **72**, 115429 (2005).
- [161] D. J. English, P. S. Eldridge, P. G. Lagoudakis, R. T. Harley, W. J. H. Leyland, J. D. Mar, M. H. R.T. Phillips, and D. Taylor, “Strain- and Electric Field-Control of Room Temperature Spin-Dynamics in GaAs/AlGaAs Quantum Wells”, in *Spintech 5 Cra-cow*, 2009.
- [162] P. S. Eldridge, W. J. H. Leyland, P. G. Lagoudakis, O. Z. Karimov, M. Henini, D. Taylor, R. T. Phillips, and R. T. Harley, “All-optical measurement of Rashba coefficient in quantum wells”, *Phys. Rev. B* **77**, 125344 (2008).
- [163] M. M. Glazov, M. A. Semina, and E. Y. Sherman, “Spin relaxation in multiple (110) quantum wells”, *Phys. Rev. B* **81**, 115332 (2010).
- [164] O. Z. Karimov, G. H. John, R. T. Harley, W. H. Lau, M. E. Flatté, M. Henini, and R. Airey, “High Temperature Gate Control of Quantum Well Spin Memory”, *Phys. Rev. Lett.* **91**, 246601 (2003).
- [165] S. Iba, H. Fujino, T. Fujimoto, S. Koh, and H. Kawaguchi, “Correlation between electron spin relaxation time and hetero-interface roughness in (110)-oriented GaAs/AlGaAs multiple-quantum wells”, *Physica E* **41**, 870 (2009).
- [166] D. Paget, “Optical detection of NMR in high-purity GaAs under optical pumping: Efficient spin-exchange averaging between electronic states”, *Phys. Rev. B* **24**, 3776 (1981).
- [167] W. O. Putikka and R. Joynt, “Theory of optical orientation in n-type semiconductors”, *Phys. Rev. B* **70**, 113201 (2004).
- [168] L. Schreiber, M. Heidkamp, T. Rohleder, B. Beschoten, and G. Guntherodt, “Mapping of spin lifetimes to electronic states in n-type GaAs near the metal-insulator transition”, [arXiv.org:0706.1884](https://arxiv.org/abs/0706.1884), 2007.

-
- [169] I. Lyubinskiy, “Spin relaxation in the impurity band of a semiconductor in the external magnetic field”, *JETP Lett.* **88**, 814 (2008).
- [170] M. Römer, J. Hübner, and M. Oestreich, “Spatially resolved doping concentration measurement in semiconductors via spin noise spectroscopy”, *Appl. Phys. Lett.* **94**, 112105 (2009).
- [171] G. M. Müller, M. Römer, J. Hübner, and M. Oestreich, “Gigahertz spin noise spectroscopy in n -doped bulk GaAs”, *Phys. Rev. B* **81**, 121202(R) (2010).
- [172] M. Beck, “Electron spin relaxation, transport and strain-induced precession in n-GaAs”, Dissertation, Univ. Nürnberg-Erlangen, 2004.
- [173] M. Oestreich, S. Hallstein, A. P. Heberle, K. Eberl, E. Bauser, and W. W. Rühle, “Temperature and density dependence of the electron Landé g factor in semiconductors”, *Phys. Rev. B* **53**, 7911 (1996).
- [174] M. Seck, M. Potemski, and P. Wyder, “High-field spin resonance of weakly bound electrons in GaAs”, *Phys. Rev. B* **56**, 7422 (1997).
- [175] J. S. Colton, T. A. Kennedy, A. S. Bracker, D. Gammon, and J. B. Miller, “Optically oriented and detected electron spin resonance in a lightly doped n-GaAs layer”, *Phys. Rev. B* **67**, 165315 (2003).
- [176] D. Stein, K. v. Klitzing, and G. Weimann, “Electron Spin Resonance on GaAs- $\text{Al}_x\text{Ga}_{1-x}\text{As}$ Heterostructures”, *Phys. Rev. Lett.* **51**, 130 (1983).
- [177] G. Lommer, F. Malcher, and U. Rössler, “Reduced g factor of subband Landau levels in AlGaAs/GaAs heterostructures”, *Phys. Rev. B* **32**, 6965 (1985).
- [178] M. Dobers, K. v. Klitzing, and G. Weimann, “Electron-spin resonance in the two-dimensional electron gas of GaAs- $\text{Al}_x\text{Ga}_{1-x}\text{As}$ heterostructures”, *Phys. Rev. B* **38**, 5453 (1988).

- [179] W. Rösner, G. Wunner, H. Herold, and H. Ruder, “Hydrogen atoms in arbitrary magnetic fields. I. Energy levels and wavefunctions”, *J. Phys. B* **17**, 29 (1984).
- [180] S. O. Demokritov, V. E. Demidov, O. Dzyapko, G. A. Melkov, A. A. Serga, B. Hillebrands, and A. N. Slavin, “Bose-Einstein condensation of quasi-equilibrium magnons at room temperature under pumping”, *Nature* **443**, 430 (2006).
- [181] A. G. Gurevich and G. A. Melkov, *Magnetization Oscillations and Waves*, CRC-Press, Boca Raton, 1st edition, 1996.
- [182] B.A.Kalinikos, “Excitation of propagating spin waves in ferromagnetic films”, *IEE Proc.* **127**, 4 (1980).
- [183] W. Wetting, M. G. Cottam, and J. R. Sandercock, “The relation between one-magnon light scattering and the complex magneto-optic effects in YIG”, *J. Phys. C* **8**, 211 (1975).
- [184] O. S. Heavens and R. F. Miller, “Measurement of Faraday Rotation in Single-Crystal Nickel Films”, *Proc. R. Soc. London A* **266**, 547 (1962).
- [185] C. Kittel, *Introduction to Solid State Physics*, Wiley, New York, 8th edition, 2004.

List of Publications

Parts of this work have already been published.

In journals:

- G. M. Müller, M. Römer, J. Hübner, and M. Oestreich, “Efficient data averaging for spin noise spectroscopy in semiconductors”, *Appl. Phys. Lett.* **97**, 192109 (2010).
- G. M. Müller, M. Oestreich, M. Römer, and J. Hübner, “Semiconductor spin noise spectroscopy: Fundamentals, accomplishments, and challenges (invited)”, *Physica E* **43**, 569 (2010).
- G. M. Müller, M. Römer, J. Hübner and M. Oestreich, “Gigahertz spin noise spectroscopy in n-doped bulk GaAs”, *Phys. Rev. B* **81**, 121202(R) (2010); see also accompanying Physics Synopsis ‘Noisy Spins’ by Sami Mitra.
- M. Römer, H. Bernien, G. Müller, D. Schuh, J. Hübner and M. Oestreich, “Electron-spin relaxation in bulk GaAs for doping densities close to the metal-to-insulator transition”, *Phys. Rev. B* **81**, 075216 (2010).

- M. Oestreich, M. Römer, G. Müller, D. Schuh, W. Wegscheider, and J. Hübner, “Spin noise spectroscopy in semiconductors”, Proc. SPIE **7398**, 739802 (2009).
- G. M. Müller, M. Römer, D. Schuh, W. Wegscheider, J. Hübner, and M. Oestreich, “Spin noise spectroscopy in GaAs (110) quantum wells: Access to intrinsic spin lifetimes and equilibrium electron dynamics”, Phys. Rev. Lett. **101**, 206601 (2008).

In talks:

- “Spin Dynamics of Equilibrium Electrons in Gallium Arsenide”, Group Seminar Prof. Ganichev, Regensburg, 3 December 2010.
- “GHz Spin Noise Spectroscopy in *n*-Doped Bulk GaAs”, Spring Meeting of the Condensed Matter Section, Regensburg, 26 March 2010.
- “Intrinsic Spin Lifetimes in GaAs (110) Quantum Wells”, 5th Spin-tech Conference, Cracow, Poland, 11 July 2009.
- “Intrinsic Spin Lifetimes in GaAs (110) Quantum Wells”, Spring Meeting of the Condensed Matter Section, Dresden, 23 March 2009.

Further articles:

- G. M. Müller, J. Walowski, M. Djordjevic, G.-X. Miao, A. Gupta, A. V. Ramos, K. Gehrke, V. Moshnyaga, K. Samwer, J. Schmalhorst, A. Thomas, A. Hütten, G. Reiss, J. S. Moodera, and M. Münzenberg, “Spin polarization in half metals probed by femtosecond spin excitation”, Nature Materials **8**, 56 (2009).
- G. M. Müller, G. Eilers, Z. Wang, M. Scherff, R. Ji, K. Nielsch, C. A. Ross and M. Münzenberg, “Magnetization dynamics in optically excited nanostructured nickel films”, New J. Phys. **10**, 123004 (2008).
- J. Walowski, G. Müller, M. Djordjevic, M. Münzenberg, M. Kläui, C. A. F. Vaz, and J. A. C. Bland, “Energy equilibration processes of electrons, magnons, and phonons at the femtosecond timescale”, Phys. Rev. Lett. **101**, 237401 (2008).

-
- G. M. Müller, M. Münzenberg, G.-X. Miao, and A. Gupta, “Activation of additional energy dissipation processes in the magnetization dynamics of epitaxial chromium dioxide films”, *Phys. Rev. B* **77**, 020412 (R) (2008).

Further talks:

- “Ultrafast dynamics in optically excited nickel nanodiscs”, 72nd Annual Meeting of the DPG and Spring Meeting of the Condensed Matter Section, Berlin, 28 February 2008.
- “Probing the half metallicity by fs carrier excitation”, 52nd Annual Conference on Magnetism and Magnetic Materials, Tampa, Florida, 7 November 2007.
- “Laser-induced magnetization dynamics of half metals and ferromagnetic nanostructures”, Frontier Developments in Optics and Spectroscopy, Centro Ettore Majorana, Erice, Sicily, 30 June 2007.
- “Magnetization dynamics of CrO₂ thin films”, 71st Annual Meeting of the DPG and Spring Meeting of the Condensed Matter Division, Regensburg, 29 March 2007.

Danksagung

An erster Stelle gilt mein Dank Herrn Prof. Dr. Michael Oestreich, der mir es ermöglicht hat, in seiner Arbeitsgruppe eine Doktorarbeit zu diesen interessanten Fragestellungen anzufertigen. Seine Anleitung und die vielen Ratschläge waren mir bei der Durchführung dieser Arbeit sehr hilfreich.

Herrn Prof. Dr. Rolf Haug danke ich für die Übernahme des Korreferates und Herrn Prof. Dr. Uwe Morgner für die Übernahme des Vorsitzes der Prüfungskommission.

Dem Evangelischen Studienwerk Villigst bin ich für die finanzielle Unterstützung dieser Arbeit durch ein Promotionsstipendium sehr zu Dank verpflichtet.

Prof. Dr. Ming-Wei Wu (Hefei, China), Prof. Dr. Eugene Sherman (Bilbao, Spanien) und Dr. Vladislav Demidov (Münster) danke ich für sehr hilfreiche wissenschaftliche Erläuterungen.

Dann gilt mein Dank den aktuellen und ehemaligen Mitarbeitern der Arbeitsgruppe Oestreich für die gute Zusammenarbeit: Hier sind an erster Stelle Dr. Jens Hübner, dessen zahlreiche Ratschläge zum Gelingen dieser Arbeit beigetragen haben, und Dr. Michael Römer, der mich in die experimentelle Ausstattung der Arbeitsgruppe eingewiesen hat und mir weiterhin häufig in technischen Fragen zur Seite stand, zu nen-

nen. Weiterhin danke ich Dipl.-Phys. Stefan Oertel, Dipl.-Phys. Hauke Horn, Dipl.-Phys. Tammo Böntgen, Dipl.-Phys. Hannes Bernien, Dipl.-Phys. Fabian Berski und Dr. Peter Eldridge für viele wissenschaftliche Diskussionen und Unterstützung bei der Laborarbeit.

Ich danke auch den übrigen Mitgliedern der Abteilung Nanostrukturen am Institut für Festkörperphysik, mit denen mir die Zusammenarbeit viel Freude bereitet hat. Ich bedanke mich insbesondere bei Yvonne Griep unter anderem für die Hilfe bei der Organisation der Sommerschule des Forschungsschwerpunktes „Halbleiter-Spinelektronik“ in Goslar, bei Ronny Hüther für die tatkräftige Unterstützung bei der technischen Umsetzung der Laborarbeit, bei Dr. Frank Hohls für viele physikalische Erläuterungen und bei Dipl.-Phys. Niels Ubbelohde und Dr. Christian Fricke für die Administration der Computer. Dipl.-Phys. Fabian Berski, M.Sc. Dave English, Dipl.-Phys. Hauke Horn, Dipl.-Phys. Stefan Oertel, B.Sc. Nils Scharnhorst, Dipl.-Phys. Henrik Schmidt und B.Sc. Carsten Schulte danke ich ferner für die Fehlersuche in der fast fertigen Arbeit.

Zu guter Letzt möchte ich mich bei meiner Familie und bei Eliane für die in jeglicher Hinsicht großartige Unterstützung meines Studiums bedanken.

Lebenslauf

Georg Martin Müller, geboren am 24. Mai 1982 in Emden.

August 1988 - Mai 2001	Schulzeit in Emden.
Mai 2001	Abitur am Johannes-Althusius-Gymnasium in Emden.
Juli 2001 - März 2002	Zivildienst.
April 2002 - September 2002	Studium der ev. Theologie an der Kirchlichen Hochschule Wuppertal.
Oktober 2002 - Juli 2007	Studium der Physik an der Georg-August-Universität Göttingen.
Juli 2004	Vordiplom in Physik.
September 2004 - März 2005	Studium an der University of California, Santa Barbara, USA.
Juli 2007	Physik Diplom. Diplomarbeit unter Anleitung von Prof. Dr. Markus Münzenberg: „Laser-induzierte Magnetisierungsdynamik von Halbmetallen und ferromagnetischen Nanostrukturen“.
Seit September 2007	Vorbereitung der Dissertation.